國立臺灣大學工學院機械工程學系

博士論文

Department of Mechanical Engineering

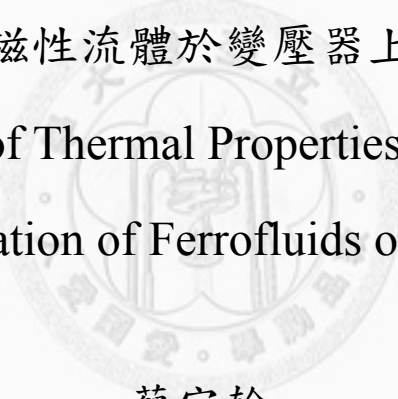College of Engineering

National Taiwan University

Doctoral Dissertation

奈米流體熱傳導係數的研究

及奈米磁性流體於變壓器上的應用

Investigation of Thermal Properties of Nanofluids

and the Application of Ferrofluids on Transformers

蔡宗翰

Tsai, Tsung-Han

指導教授：陳炳煇教授、吳文方教授

Advisor: Prof. Chen, Ping-Hei, Prof. Wu, Wen-Fang

中華民國 九十九 年 六 月

June 2010

Acknowledgement

It is hard to express my sincere gratitude by words to those who provided me with support and advice to help bring out this thesis.

My deepest gratitude goes first and foremost to Professor Ping-Hei Chen and Professor Wen-Fang Wu, my advisors, for your constant encouragement and guidance. I have benefited a lot from your illumination and instruction not only in studies but also in life experience. Appreciations are also expressed to the member of oral examination committee, Dr. Chao-Kuang Chen, Dr. Da-Sheng Lee, Dr. Chih-Cheng Lu, Dr. Chin-Ting Yang, Dr. Yao-Joe Yang and, for your valuable suggestions and constructive criticism.

Second, I would like to express the gratitude to my friends and lab mates who gave me their help and time in listening to me and helping me work out my problems during the difficult course of the thesis.

Last, my thanks would go to my family, my mother and my beloved, Ching-Yie, for your considerations and confidence in me all through these years. Without your supports, I cannot complete this work.

摘要

　　本論文主要討論奈米流體的熱傳導係數及奈米磁性流體的應用。在第一個主題中，我們討論了基礎流體的黏滯性對奈米流體的熱傳導係數的影響。實驗結果顯示，在低黏度的基礎流體中，奈米顆粒對奈米流體的熱傳導係數有明顯的增益。對於低黏度的奈米流體，量測到的熱傳導係數高於 Maxwell 模型所估計的值。當基礎流體的黏滯性增加時，量測到的奈米流體的熱傳導係數會越來越趨近於 Maxwell 模型的估計值，這表示了奈米流體的黏滯性會影響它們的熱傳導係數，以及懸浮的奈米顆粒的布朗運動大大地增進了奈米流體的熱傳導係數。此外，由於奈米磁性流體具有一些特殊的性質，因此衍生了新的應用。在第二個主題中，奈米磁性流體及四氧化三鐵塊被用來作為變壓器的磁芯。本論文使用的變壓器建構於毛細管及晶圓上。我們針對不同磁芯的變壓器的效能做了量測及模擬。雖然四氧化三鐵的存在增加了電感值及耦合係數，但是由於外加磁場與材料磁化有相位差的關係，電阻值也跟著增加而影響效能。最後，我們提出了一個製造固態磁芯的製程。在低於 4MHz 頻率下，具有固態磁芯的變壓器的效能會高於空氣芯變壓器的效能。

關鍵詞：熱傳導係數、奈米流體、布朗運動、奈米磁性流體、變壓器

Abstract

The thermal conductivity of nanofluids and the application of ferrofluids are investigated. With respect to the first topic, the effect of the viscosity of base fluids on the thermal conductivity of nanofluids is discussed. Experimental results reveal an obvious enhancement on thermal conductivity of nanofluids with low viscous base fluids. The measured thermal conductivity of low viscous nanofluids markedly exceeds that predicted by Maxwell prediction model. As the viscosity of the base fluid increases, the measured thermal conductivity of the nanofluid gradually approaches the value predicted by Maxwell prediction model, indicating that the viscosity of nanofluids influences their thermal conductivity, and the Brownian motion of suspended particles importantly enhances the thermal conductivity of nanofluids. Moreover, while the first topic is investigated, some special properties of ferrofluid are found. Therefore, a new application is derived. With respect to the second topic, ferrofluids and bulk Fe_3O_4 are applied as the magnetic cores of transformers. The transformers used in this thesis are constructed on a capillary or on a wafer. The performance of transformers with different magnetic cores is measured and simulated. Although Fe_3O_4 increases the inductance and coupling coefficient, it also increases the resistance owing to a lag between the external magnetic field and the magnetization of the material. Finally, a new process for

fabricating a solid magnetic core is proposed, in which ferrofluids are used to deliver ferro-nanoparticles into microchannels. A transformer with a solid magnetic core outperforms the same transformer that with an air core below a frequency of 4 MHz.

Keywords: Thermal conductivity, nanofluids, Brownian motion, ferrofluids, transformers

Nomenclature

k thermal conductivity

ϕ volume fraction of particles

d diameter

T temperature

T_0 initial temperature

t time

κ thermal diffusivity

r radial distance

q heat per unit length per unit time

Ei exponential integral function

F force

G torque

H^* distance between the cup and cylinder

Ra radius of cylinder

Len length of cylinder

Ω angular velocity of cylinder

D_B Brownian diffusion coefficient

k_B	Boltzmann constant
μ	viscosity
K	coupling coefficient
L	inductance
R	resistance
Z	impedance
ω	angular frequency
Q	quality factor
μ^*	permeability
μ'	real part of permeability
μ''	imaginary part of permeability
N	number of coil turns
A	cross section area
l	length of solenoid
E	electric field
B	magnetic field
H	magnetizing field
J	free current density
D	electric displacement field

ρ free charge density

$\tan\delta$ magnetic tangent loss

Subscript:

Maxwell   Maxwell prediction model

p   particle

bf   base fluid

nano   nanofluid

Table of Contents

List of Tables

List of Figures

The photo of processed wafer after line patterning

The photo of processed wafer after metal etching

The photo of processed wafer after Cu and Au electroplating

The photo of processed wafer after dry film patterning

The photo of processed wafer after via electroplating

The diagram of wafer cutting line

The schematic diagram of wire bonding

The measuring sample of MEMS transformer

The circuit diagram of high voltage output device

The photo of high voltage output device

The contact angles between bulk Fe_3O_4 and components of viscous base fluids: (a)

diesel oil; (b) PDMS

The schematic measurement of self inductance and leakage inductance

The effective circuit model of real inductors containing the series resistance and

parasitic capacitance

The self-inductance of coils of transformers with different magnetic cores

The leakage inductance of coils of transformers with different magnetic cores

The coupling coefficient of transformers with different magnetic cores

The resistance of coils of transformers with different magnetic cores

The quality factor of coils of transformers with different magnetic cores

The quality factor of coils of transformers with different magnetic cores at low

frequency

The simulated resistance of coils of MEMS transformer with the air core and magnetic

core of 1 M Fe_3O_4 nanofluid

The simulated quality factor of coils of MEMS transformer with the air core and

magnetic core of 1 M Fe_3O_4 nanofluid

The macroscopic view of Fe_3O_4 nanoparticles: (a) without a magnetic field; (b) with a

magnetic field.

The microscopic view of Fe_3O_4 nanoparticles: (a) without a magnetic field; (b) with a

magnetic field.

Chapter 1 Introduction

1.1 General Remarks

Nanofluids that comprise suspended nanoparticles in a base fluid has been used in numerous engineering applications, including microfluidic devices, heat exchangers, and optical switches. Choi [1] first coined the term "nanofluid" in 1995. Experimental results [2-7] reveal that a nanofluid has better heat transfer properties than the conventional heat transfer fluid or the corresponding base fluid with microparticles. However, the mechanism of improvement of the performance of a system using nanofluid should be carefully studied to optimize the performance of the system. This thesis investigates the mechanism of enhancement of the thermal conductivity of a base fluid upon the addition of nanoparticles. Then, due to the special properties of ferrofluid, a ferrofluid is used as a magnetic core of a capillary power transformer and of a MEMS power transformer. This application of nanofluid has not been investigated in prior studies.

Suspended nanoparticles in base fluid are expected to increase the thermal conductivity of the base fluid because the thermal conductivity of the suspended particles greatly exceeds that of the base fluid. However, numerous experimental studies

have shown that the enhancement of thermal conductivity of the base fluid greatly exceeds the enhancement that is predicted by traditional models of the thermal conductivity of composite materials. Even at a very low volume fraction, nanoparticles significantly enhance the thermal conductivity of a base fluid. This study presents evidence of the mechanism of enhancement of the thermal conductivity of base fluid by suspended nanoparticles.

In the second part of this thesis, due to the special properties of ferrofluid we found in the first part, the magnetic core of a miniature power transformer is replaced with ferrofluid. Ferrofluid is a colloidal mixture of ferro-nanoparticles, surfactant and base fluid. The ferro-nanoparticles are typically oxides of Fe, Co, Ni or a combination of different metals with an average diameter of approximately 10 nm. The ferro-nanoparticles are coated with surfactant to prevent their aggregation. This surfactant also modifies their surfaces, making them hydrophilic or hydrophobic, causing the ferro-nanoparticles to be uniformly suspended in the base liquid, like water or oil. The ferrofluid does not exhibit magnetism and the orientation of the ferro-nanoparticles is random when no external magnetic field is applied. When an external magnetic field is applied, the ferro-nanoparticles become polarized and their magnetic moments align with the magnetic force lines. Once the external magnetic field is removed, the orientation of ferro-nanoparticles returns to random. Although bulk

Fe_3O_4 exhibits ferromagnetism, the ferro-nanoparticles with a diameter of less than 50 nm exhibit super-paramagnetism. Therefore, the ferrofluid also exhibits super-paramagnetism. For decades, ferrofluid has been used as the heat transfer fluid in loudspeakers [8], as the damper in stepper motors and shock absorbers, and as the low-friction seal in rotating shaft motors and computer disk drives to keep out contaminants [9]. Ferrofluid also has some interesting properties. When an external magnetic field is applied to it, it adopts special shapes [10].

A transformer is an electrical device that typically contains two or more copper coils. The main purposes of transformers are to step up or down the voltage of the AC source, to change its effective impedance and separate the circuits. The transformer applies Faraday's law of induction to transfer electrical energy from one coil to another. The law states that the induced electromotive force (EMF) in any closed circuit equals the rate of change of the magnetic flux through the circuit. The AC source in the primary winding generates an alternating magnetic flux through the core of the transformer. Then, the alternating magnetic flux goes passes through the secondary winding, inducing an alternating EMF in it. This effect is called mutual induction. One of the most important parts of a transformer is the magnetic circuit, which provides a path of least magnetic resistance. A magnetic circuit typically includes a ferromagnetic material, such as metal and oxides of Fe, Co and Ni. These materials have a high

relative permeability, which ranges from hundreds to thousands, even reaching 20000, and so provide a path of low magnetic resistance. However, such solid materials exhibit hysteresis. Whenever the magnetic flux is reversed, some energy is lost by hysteresis in the magnetic core. As the frequency increases, the hysteresis loss increases proportionally. Another special transformer is the air core transformer, which is commonly used in radio-frequency circuits. This transformer has a non-magnetic core, and therefore none of the undesirable properties of a ferromagnetic core, such as eddy current loss, hysteresis loss, saturation and others, but the coupling coefficient between windings is lower than that of an iron core transformer. Both types of transformer have shortcomings. Transformers have a wide range of sizes, from a micro-sized transformer to a huge unit that weighs tons. Although range of designs is extensive, their basic operating principles are identical.

Both of the above topics have attracted considerable attention and have been extensively investigated in recent decades. However, there are no researches or convincing investigations about the integration of above topics. The aim of this study is to elucidate the effect of the viscosity of base fluid on the thermal conductivity of nanofluids, and the application of ferrofluids on MEMS chip transformers. To investigate thermal conductivity, water-based and oil-based nanofluids are adopted. The mechanism of enhancement of thermal conductivity of nanofluids is discussed with

reference to experimental results. Ferrofluids are applied in two transformers. One is constructed on a capillary, and the other is constructed on a wafer by the MEMS process. The performance of the transformers is measured using a precision impedance analyzer and simulated by performing an Ansoft HFSS 3D full-wave electromagnetic field simulation.

1.2 Literature Survey

1.2.1 Thermal Conductivity of Nanofluids

In the last decades, scientists have proposed several methods to improve the heat transfer, and one of the most popular methods is to enhance the thermal conductivity of heat transfer fluids. As shown in Table 1.1 [2], the thermal conductivity of solid is much higher than that of liquids. In order to increase the thermal conductivity of heat transfer fluids, originally, the solid particles had been added in the heat transfer fluids. Since Maxwell prediction model [11] was proposed over one hundred years ago, considerable experimental and theoretical studies of suspensions containing solid particles have been proposed. However, due to the large size and higher density of solid particles, the solid particles cannot suspend in the liquid for a long time, and the precipitation may result in the wear of container and additional flow resistance. For the reasons mentioned above,

5

the fluids containing the large-sized particles are not practical.

Today, the nano-sized particles with average diameter below 50 nm can be produce by the novel nanotechnology. The fluids in which nanoparticles suspended are named "nanofluids" by Choi [1] in 1995. Comparing to the conventional heat transfer fluids and the fluids containing microparticles, nanofluids have better performance. The smaller size and larger relative surface area of nanoparticles results in great enhancement of heat transfer and help nanoparticles suspend stably in fluids and also improve the wearing problem of container. For the reason mentioned above, nanofluids can be regarded as the next-generation heat transfer fluids and bring the smaller heat transfer systems. Although the use of nanofluids appears promising, however, there are some factors hinder the development of nanofluids [12], such as the lack of agreement between results obtained in different laboratories, the often poor characterization of suspensions and the lack of theoretical understanding of the mechanisms responsible for the observed changes in properties.

The metal and oxide of Al and Cu are the most commonly used materials of nanoparticles. Almost all the experimental results have indicated the enhancement of thermal conductivity of nanofluids. Eastman et al. [2] suspended Al_2O_3, CuO and Cu nanoparticles in water and HE-200 oil and got 60% enhancement of thermal conductivity with 5% volume fraction of nanoparticles. Lee et al. [3] suspended CuO

and Al_2O_3 nanoparticles of different diameters in water and EG and obtain higher thermal conductivity. It also suggested that the size of nanoparticles should be a dominant factor of enhancement on thermal conductivity. Wang et al. [4] suspended Al_2O_3 and CuO nanoparticles in water, EG, vacuum pump oil and engine oil. Experimental results indicated that the high thermal conductivity of nanofluids is dependent on the structure and microscopic motion of nanoparticles. Xuan and Li [5] suspended Cu nanoparticles in water and transformer oil and found that Cu nanoparticles in transformer oil had higher enhancement on thermal conductivity than those in water. Xie et al. [6] suspended different kinds of Al_2O_3 nanoparticles in water and EG and found that the increase in difference between the pH value of nanofluids and isoelectric point of Al_2O_3 nanoparticles. And the enhancement on thermal conductivity highly depended on the specific surface area (SSA) of nanoparticles. Eastman et al. [7] suspended Cu nanoparticles of less than 10 nm size in EG and obtained 40% enhancement on thermal conductivity with 0.3% volume fraction of Cu nanoparticles. It indicated that the high SSA should be an important factor and the additive acid may help nanoparticles suspend well.

There are also other materials of nanoparticles applied. Hong et al. [13] suspended Fe nanoparticles in EG and obtained the higher enhancement on thermal conductivity than those of Cu nanofluids. The experimental results showed the non-linearly increase

7

of thermal conductivity with increase of nanoparticles volume fraction. They also

investigated the effect of clustering of Fe nanoparticles on the thermal conductivity of

nanofluids and found that the agglomeration of Fe nanoparticles influences the thermal

conductivity of nanofluids [14]. Murshed et al. [15] suspended TiO_2 nanoparticles of

rod shape and spherical shape in water and found that the size and shape of

nanoparticles influence the thermal conductivity of nanofluids. Xie et al. [16, 17]

suspended SiC nanoparticles of 26 nm and 0.6 μm diameters in water and EG and found

that the nanofluids with the same particles in different base fluid had the same

enhancement on thermal conductivity, which differ from Lee et al. [3]. And the results

showed that Hamilton-Crosser model [18] predicted the thermal conductivity of 0.6 μm

SiC nanofluids precisely but underestimated that of 26 nm SiC nanofluids.

One of important factors, temperature, had also been investigated. Das et al. [19]

suspended Al_2O_3 and CuO nanoparticles in water and observed that thermal

conductivity of nanofluids increased 2 to 4 times with the temperature range of 21℃ to

52℃. They also mention that the motion of nanoparticles could be a probable factor for

the enhancement on thermal conductivity. Li and Peterson [20] suspended CuO and

Al_2O_3 in water. The results indicated that the material, diameter, volume fraction and

temperature are significant factors. They also derived simple linear regression of two

factors. Patel et al. [21] suspended Au and Ag coating citrate and thiolate of low volume

8

fraction in water and toluene based fluids and indicated that there are important factors related to the motion of nanoparticles, since the great enhancement occurs with the temperature range 30-60℃.

Experimental results mentioned above shows the unusual enhancement on thermal conductivity which the conventional prediction model fails to explain. To explain the reason for the anomalous enhancement on thermal conductivity of nanofluids, Keblinski et al. [22] and Eastman et al. [23] proposed four possible mechanisms: Brownian motion of nanoparticles, molecular-level layering of the liquid at the liquid/particle interface, the nature of heat transport in nanoparticles, and the effect of cluster of nanoparticles. Many scientists adopted the concept of liquid/solid interface layer to explain the anomalous enhancement on thermal conductivity of nanofluids. Yu and Choi [24, 25] proposed the models based on Maxwell model and Hamilton model which consider the liquid molecular layer around the nanoparticles. But Xue et al. [26] applied molecular dynamic simulation to show that the liquid layer had no effect on thermal transport properties. Koo and Kleinstreuer [27] found that the impact of Brownian motion is much more significant than that of thermophoretic and osmophoretic motion. Evans et al. [28] proposed that the hydrodynamics effects associated with Brownian motion have only a minor effect on the thermal conductivity of nanofluids. Besides the Brownian motion, liquid layer and agglomeration, Lee et al. [29] investigated the effect

of surface charge state of nanoparticles and showed that the pH value of nanofluids strongly affected the thermal conductivity of nanofluids. Based on these postulated mechanisms, numerous theoretical studies had also proposed to predict the thermal conductivity of nanofluids. Most of these studies are sourced from the classic model of Maxwell [11] of which the effective thermal conductivity, k_{eff}, is given by:

$$k_{Maxwell} = \frac{k_p + 2k_{bf} + 2(k_p - k_{bf})\phi}{k_p + 2k_{bf} - (k_p - k_{bf})\phi} \tag{1.1}$$

where k_p is the thermal conductivity of particles, k_b is the thermal conductivity of base fluids and ϕ is the volume fraction of particles. Yu and Choi [24] proposed a modified Maxwell model to present the effect of the liquid layer around nanoparticles. The thermal conductivity of particles k_p in (1.1) is replaced with the modified thermal conductivity of particles. They also proposed a modified Hamilton-Crosser model including the liquid layer for non-spherical particles [25]. There are also other modified models including the effect of liquid layer around particles [30-32]. However, these prediction models fail to predict some cases showed the great enhancement on thermal conductivity at low concentrations [21]. According to previous studies [19-21], the thermal conductivity of nanofluids depends strongly on temperature. The Brownian motion of nanoparticles may be a key factor ruling the thermal properties of nanofluids. Xuan et al. [33] proposed a modified model based on the Maxwell model with considering the Brownian motion. But the temperature dependence of this model is too

weak and not in agreement with the study of Das et al. [19]. Kumar et al. [34] proposed a model based on the Stokes-Einstein formula and depended strongly on temperature. Bhattacharya et al. [35] developed a technique based on parallel model and using the Brownian motion simulation. Jang and Choi [36, 37] proposed a model based on the parallel model and involving four modes of energy transport in nanofluids: the collision between base fluid molecules, the thermal diffusion in nanoparticles involving the Kapitza resistance [38], the collision between nanoparticles due to Brownian motion, and the thermal interactions of dynamic or dancing nanoparticles with base fluid molecules. Prasher [39] proposed a model based on the Maxwell model and including the convection of liquid near nanoparticles due to Brownian motion. Koo and Kleinstreuer [40, 41] proposed a model based on the Maxwell and taking the effects of particle size, particle volume fraction and temperature dependence as well as properties of base liquid and particle phase into consideration by considering surrounding liquid traveling with randomly moving nanoparticles. Although many possible mechanisms and theoretical researches are proposed, no models can predict the thermal conductivity precisely and satisfactorily for all nanofluids. It still needs further understanding to develop a comprehensive and convincing model.

1.2.2 Ferrofluids

Magnetic fluids or ferrofluids are the fluids in which magnetic particles suspended [9]. Magnetic particles can be attracted by the magnetic field. While magnetic particles are moving, the molecules of base fluid are also carried away. Hence, the bulk fluid is controllable. The magnetic fluids are composed of three major materials: the carrier liquid, magnetic particles and the surfactant. The surfactant is used to prevent magnetic particles from aggregation. The most common type of ferrofluids is the colloidal ferrofluid. The colloidal means a suspension of finely divided particles in a continuous medium. Since the stability of magnetic fluid as a colloidal system depends on the thermal motions of particles, which prevent from agglomeration and precipitation, the size of magnetic particles must be small enough. But the size of particles must not be too small. The magnetic properties of particles disappear if the size of particles is less than 1~2 nm. Thus the diameter of magnetic particles suspended in the carrier fluid is about 3~15 nm. The Brownian motion keeps the particles from settling under the gravity. And the surfactant is attached around the surface of particles to provide the repulsion between particles to prevent particles from agglomeration under a magnetic field [42].

There are two commonly used methods to prepare the magnetic fluid: precipitation and grinding. The precipitation method is a chemical reaction of condensation [43]. The chemical reaction show as follow:

$$FeCl_2 \cdot 4H_2O + 2FeCl_3 \cdot 6H_2O + 8NaOH \rightarrow Fe_3O_4 \downarrow + 8NaCl + 20H_2O \quad (1.2)$$

After rinsing the particles several times with water and finally once with 0.01 M HCl solution, the particles are added into the 0.5 percent soap solution and boil for a short time. Then the magnetic fluid is obtained. And Reimers and Khalafalla [44] use the lauric acid as the surfactant to prepare the water-based ferrofluid. There are other kinds of commonly used surfactants like oleic acid, tetramethylammonium hydroxide (TMAH), citric acid and soy lecithin. The grinding method is proposed by Papell [45]. The magnetite Fe_3O_4, the surfactant oleic acid and the carrier liquid kerosene are grinded together in a ball mill for a long time, and the nanometer-sized particles with diameter of 10 nm are obtained. Both two methods have individual advantages. The grinding method is very simple, the uniform dispersion is easy to be attained, there is no carrier liquid loss, and the applicable materials of particles and carrier liquid are various. But the major disadvantages of grinding method are time-consuming and lower yield. Reversely, the co-precipitation method is minute and complicated, and the magnetization of produced particles is relatively lower than that of particles produced by grinding method. However, it takes shorter time and higher yield for producing and needs no expensive instruments. Thus the co-precipitation method is adopted in this study.

The ferrofluids have been widely used in the recent years. There are various

applications, such as the seal, bearing, damper, loudspeaker, Inclinometer, nuclear

magnetic resonance (NMR) probe, Angular position sensor and Magnetic domain

detection. [46]. In the dilute and functionalized forms, ferrofluids have also applied on

the medicine as magnetic separation for purification and immunoassay, drug delivery

and targeting, magnetic resonance imaging and diagnosis and hyperthermia [47-52].

Ferrofluids also can be a useful alternative of moving mechanical components for the

miniaturized cooler, pump, valve, mixer and integrated micro total analysis systems

(μ-TAS) [53-59].
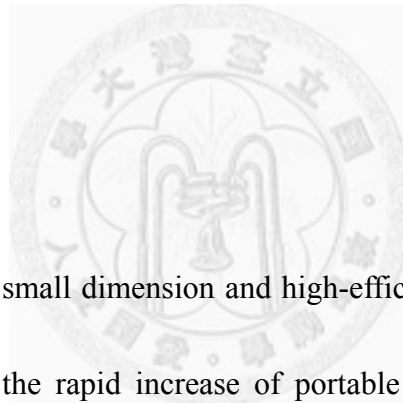
1.2.3 Transformers

In the recent year, the small dimension and high-efficiency transformers/inductors

are greatly needed due to the rapid increase of portable and miniaturized electronic

products such as cellphone, notebook, digital camera, etc. In order to reach these

demands, micro transformers/inductors fabricated by MEMS process have been

developed. Up to now, MEMS transformers/inductors which have been proposed for the

use of switching power converters or signal isolators can be divided into two types:

planar spiral type and 3D solenoid type. Both two types have their own advantages and

disadvantages.

For the planar spiral type, a transformer/inductor is commonly composed of planar

spiral coils, isolating layers and magnetic films and fabricated on silicon substrate using

MEMS techniques. Kim's group [60-62] presents several planar spiral type inductors

using magnetic thin film core of Fe-Zr-C-N nanocrystalline, Ti/FeTaN and FeBN.

However, the inductance of inductor is dropped slightly due to eddy current. Wang et al.

[63] present gapped and ungapped micro-machined inductors realized on a silicon wafer

using low temperature IC compatible electrochemical processes. Two layers of bottom

FeCoBN and single layer of top FeCoBN are electroplated as magnetic thin film core.

The ungapped inductor has a higher inductance value compared to the gapped inductor.

However, the inductance of the ungapped inductor drops much more rapidly with bias

current. The planar spiral type transformer/inductor usually has larger size, and the

magnetic flux is perpendicular to the plane of substrate and magnetic core, which causes

the eddy current loss in the substrate and magnetic core. So, some solutions have been

developed to reduce the eddy current loss. Yoon's group [64-67] presents a

CMOS-compatible versatile thick-metal surface micromachining technology which

enables to build 3D metal microstructures on standard silicon substrate as post-IC

processes at low temperature below 120 C. Spiral inductors suspended 100 μm over the

substrate, coplanar waveguides suspended 50 μm over the substrate, and complicated

micro-coaxial lines, which have 50 μm suspended center signal lines surrounded by

inclined ground shields of 100 μm in height are demonstrated. Chong et al. [68] present

the performance of spiral transformers on silicon substrate with micro-porous silicon (PS) region. The use of PS significantly reduces the substrate effects including eddy current and capacitive coupling between spirals and the substrate and lead to higher quality factor and resonant frequency, mutual reactive coupling coefficients with larger useable band width and higher available gain mainly because of the reduction in power loss to the substrate. Zhao et al. [69] present a planar inductor with the magnetic core of permalloy-SiO_2 granular film. By controlling the composition and microstructure, a permalloy-SiO_2 granular film with excellent soft magnetic properties and high electrical resistivity is produced. Yunas et al. [70, 71] present planar transformers with stacked double coil structure on high resistive glass substrate, which introduces the simple micromachining fabrication process with a bonding step. The planar transformers on glass substrate is flipped and bonded on the etched silicon substrate. The eddy current is reduced due to the air gap between coils and silicon substrate.

For the 3D solenoid type, the key challenge of miniaturized transformers/inductors is to construct the 3D structure and magnetic core which are more complex than that of planar spiral type. Laney et al. [72] present a set of microwave inductors and transformers fabricated in a solenoid design utilizing two metal layers rather than a single metal layer as used in conventional planar magnetic devices. The fabrication process utilized a production Si/SiGe HBT technology with standard metallization and a

thick polyimide dielectric. Yoon's group [73] presents a fabrication process for monolithic integration of solenoid inductors. The fabrication of air bridges of inductor is possible by forming a three-dimensional photoresist mold using multi exposures with varying exposure depths, following by a single development step, which realizes the 3D latent image of the unexposed volume in the photoresist. Yoon's group [74, 75] also presents a sacrificial metallic mold (SMM) method to fabricate a solenoid-type microwave transformer on a glass wafer. The SMM method requires a single seed metal layer and provides a thermally-stable metal mold for successive thick photoresist patterning and electroplating. Xu et al. [76] present a solenoid-type micro transformer with a laminated core structure for high frequency power or signal conversion. The laminated core structure has been adopted and implemented by using micromachining techniques to reduce the eddy current loss. Zhuang et al. [77] present a solenoid type inductor with the magnetic core of Cr/Fe10Co90 /Cr films which is performed by magnetron sputtering at room temperature under a dc magnetic field. Park et al. [78] present a solenoid-type inductor with highly laminated magnetic cores for low-megahertz power applications. The magnetic core of inductor has 72 laminations of 1 μm thick Ni/Fe films. A laminated core is used for reducing the eddy current in the electroplated Ni/Fe core. Gao et al. [79] present a solenoid-type micro inductor fabricated by MEMS technique, and the NiFe film is electroplated as the magnetic core,

and the polyimide which has low permittivity is used as the isolation material. Lei et al. [80] present a solenoid-type micro inductor with the Fe-based magnetic core. The magnetic core of FeCuNbCrSiB soft magnetic thin film is deposited by magnetron sputtering and patterned by UV-photolithography.

Although many manufacturing processes and materials have been proposed, in order to meet the requirement of increasingly miniaturized electronic component, further investigations are needed to develop high performance transformers/inductors.

1.3 Motivation and Objectives

The thermal conductivity of nanofluids has been investigated for decades. Comparing with the thermal conductivity predicted by conventional models like Maxwell prediction model, the measured thermal conductivity is much higher. This phenomenon gives rise to researches of the mechanisms of the enhancement on the thermal conductivity of nanofluids and also the investigations of new prediction models of thermal conductivity of nanofluids. Some investigations have indicated that the enhancement of thermal conductivity which directly results from collisions between nanoparticles is not obvious, and the Dominant factor of the enhancement in thermal conductivity is the convectionlike behavior which indirectly results from Brownian

motion. The convectionlike models presented by Choi [37] and Prasher [39] are shown

as follow:

$$k_{eff} = k_{bf}(1-\phi) + \beta k_p \phi + C_1 \frac{d_{bf}}{d_p} k_{bf} \, \text{Re}_{d_p}^2 \, \text{Pr} \, \phi \tag{1.3}$$

$$\frac{k_{eff}}{k_{bf}} = (1 + A\,\text{Re}^m \,\text{Pr}^{0.333}\,\phi)\left(\frac{[k_p(1+2\alpha)+2k_m]+2\phi[k_p(1-\alpha)-k_m]}{[k_p(1+2\alpha)+2k_m]-\phi[k_p(1-\alpha)-k_m]}\right) \tag{1.4}$$

where β is a constant for considering the Kapitza resistance per unit area, d_{bf} is the

diameter of molecule of base fluid, d_p is the diameter of nanoparticles, C_1, A and m are

constants, km is the thermal conductivity of matrix, Re is the Reynolds number, and Pr

is the Prandtl number. It is obvious that the effective thermal conductivities of both

models, k_{eff}, are divided into the static part of thermal conductivity, k_{static}, and the

dynamic part of thermal conductivity, k_{static}:

$$k_{eff} = k_{static} + k_{dynamic} \tag{1.5}$$

where the static part of thermal conductivity, k_{static}, presents the thermal conductivity

due to the difference of composition of nanofluids which includes the volume fraction

of nanoparticles in nanofluids and the thermal conductivity of nanoparticles and base

fluid. And the dynamic part, k_{static}, presents the thermal conductivity due to the effect

associated with Brownian motion. However, neither the static parts nor the dynamic

parts of both convectionlike models provide a consistent and convincing prediction

model for all nanofluids. This part of the study is aimed to clarify the model of static

part on the enhancement of thermal conductivity with nanoparticles in a base fluid at different viscosities.

As the general remarks mentioned, the ferromagnetic core transformer has some undesirable properties like eddy current loss, hysteresis loss, saturation and so on. Although the air core transformer eliminated the undesirable properties, the coupling efficiency and inductance are relatively lower. Both type transformers have individual disadvantages. For the reason mentioned above, an improvement is being constructed in this study. If the ferrofluid is applied as the magnetic core of transformer, due to the properties of high resistance and super-paramagnetism of ferrofluids, the eddy current loss and hysteresis loss can be eliminated. On the other hand, the relative permeability of ferrofluids is higher than that of air so that the coupling coefficient and inductance will also be improved. This part of study is aim to verify the improvement of transformer performance with application of ferrofluids, and the simulations are also made to proof the experiment results.

1.4 Outline of the Thesis

This study investigates the effect of viscosity of base fluid on thermal conductivity of nanofluids and the application of ferrofluids on the MEMS transformer. Firstly, the

enhancement on thermal conductivity of nanofluids and the mechanism are discussed.

Next, the performance of transformers which applies the ferrofluids as the magnetic

core is measured by a precision impedance analyzer and also simulated by Ansoft HFSS

3D full-wave electromagnetic field simulation. In Chapter 1, firstly, the background of

this study is introduced. Then, the literatures including the thermal conductivity of

nanofluids, ferrofluids and transformers are reviewed. Finally, the motivation, objectives

and outline of this thesis are described. In Chapter 2, the fabrication processes of

nanofluids and transformers are described. Then, the experimental procedure and

apparatus used in this thesis are also shown. In chapter 3, the physical properties of both

water-based and oil-based nanofluids are discussed. In chapter 4, the definition of the

coupling efficiency and quality factor are described, and the measured and simulated

results of both two transformers are discussed. Finally, chapter 5 summarizes the

experimental results of chapter 3 and 4, and the future prospects are proposed.

Table 1.1 Thermal conductivities of various solids and liquids

	Material	Thermal Conductivity (W/m-K)
Metallic Solids:	Silver	429
	Copper	401
	Aluminum	237
Nonmetallic Solids:	Silicon	148
	Alumina (Al_2O_3)	40
Metallic Liquids:	Sodium @644K	72.3
Nonmetallic Liquids:	Water	0.613
	Ethylene Glycol	0.253
	Engine Oil	0.145

Chapter 2 Fabrication Processes and Experimental Apparatus

Firstly, the fabrication processes of Al_2O_3 nanofluids and Fe_3O_4 nanofluids are described. Then, the fabrication processes of transformers are described. Finally, the third section describes the experimental procedure and apparatus for measuring physical properties of nanofluids and performance of transformers.

2.1 Fabrication of Nanofluids

This section describes the fabrication processes of water-based Al_2O_3 nanofluids and oil-based Fe_3O_4 nanofluids.

2.1.1 Fabrication of Water-Based Al_2O_3 Nanofluids

The water-based Al_2O_3 nanofluid used in this study is composed of Al_2O_3 nanoparticles with the modified surface and the viscous base fluids which consist of water, ethylene glycol (EG) and glycerol.

The Al_2O_3 nanoparticles of which the surface is modified by Sodium Citrate are purchased from the Yong-Zhen technomaterial CO., LTD. And the compound of water and EG and the compound of EG and Glycerol, are used as the two kinds of viscous base fluids. The Al_2O_3 nanoparticles are added directly into the viscous base fluids with proper ratios. The mixtures are stirred for 2 hours and vibrated with ultrasonic sieving

for 6 hours under room temperature. Then the water-based Al_2O_3 nanofluids with 2%

volume fraction of Al_2O_3 nanoparticles are obtained.

2.1.2 Fabrication of Oil-Based Fe₃O₄ Nanofluids

The oil-based Fe_3O_4 nanofluid used in this study is composed of Fe_3O_4

nanoparticles, the surfactant, and the compound of diesel oil and polydimethylsiloxane

(PDMS). The Fe_3O_4 nanoparticles are fabricated by the co-precipitation method for the

reason of fast and efficient production. The chemical reaction formula is expressed as:

$$Fe^{2+} + 2Fe^{3+} + 8OH^- \rightarrow Fe_3O_4 + 4H_2O \tag{2.1}$$
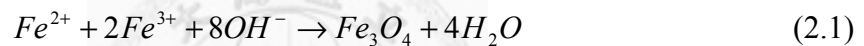
The chemical reagents needed in the experiment are listed in Table 2.1. The flow chart

of the precipitation procedure is shown in Fig. 2.1. Firstly, the $FeCl_2 \cdot 4H_2O$ and $FeCl_3 \cdot$

$6H_2O$ are dissolved in 100ml DI water with the mole ratio of 1:2. And the proper

quantity of NaOH is dissolved in 400ml DI water. Then the Fe^{2+}/Fe^{3+} solution is slowly

poured into the OH^- solution under stirring by a magnetic stirrer at a rotating speed of

500rpm. The Fe_3O_4 nanoparticles are synthesized immediately, and the whole solution

becomes black. When the precipitation reaction finished, the PH value of solution

should be controlled at 10~12. In the solution, there are some needless impurities and

ions which should be washed out. After keeping the solution static for a while, the

Fe_3O_4 nanoparticles precipitate, and the top of the solution becomes transparent. The

permanent magnet is used to accelerate the separation between Fe_3O_4 nanoparticles and

the solution. The washing process is repeated for several times to remove the needless

impurities and ions, and about 150ml water is left in the beaker. In order to prevent the

Fe_3O_4 nanoparticles from aggregation and to modify the surface of Fe_3O_4 nanoparticles,

the oleic acid is added as a surfactant. Because the oleic acid is not dissolved in water,

ammonia is used to modify the functional group of oleic acid to make it dissolve in

water. The chemical reaction of the modification process is expressed as:

$$\sim COOH + NH_4OH \rightarrow \sim COONH_4 + H_2O \tag{2.2}$$

Two ends of oleic acid molecule have different properties. The $\sim COONH_4$ end is

hydrophilic, and the hydrocarbon end is hydrophobic. After adding the ammonia and

oleic acid one after the other, the solution is heated and kept at $80℃$ and stirred for 2

hours. Then the water-based Fe_3O_4 nanofluid is obtained. As shown in Fig. 2.2(a), the

hydrophilic end of oleic acid attaches to the surface of Fe_3O_4 nanoparticles, which forms

the first layer of surfactant. Then the hydrophobic end of fixed oleic acid connects to

other oleic acid, which forms the second layer of surfactant. Such structure provides the

stable and uniform distribution of Fe_3O_4 nanoparticles in water.

By applying the phase transferring method, the base fluid can be changed. The

phase transferring process is shown in Fig. 2.3. In this study, the ethanol served as a

medium which can be dissolved in water and diesel oil. The enough quantity of ethanol

is added into the water-based Fe_3O_4 nanofluid, and the solution is stirred for 3 minutes. After keeping the solution static for a while, the Fe_3O_4 nanoparticles precipitate again, and the permanent magnet is used to accelerate the separation. After using the ethanol to wash out the outer layer surfactants and water for several times, the hydrophobic Fe_3O_4 nanoparticles with the single layer of surfactant, as Fig. 2.2(b) shown, are obtained. Finally, the proper quantity of diesel oil is mixed with the Fe_3O_4 nanoparticles. After the mixture is vibrated by an ultrasonic sieving for 2 hours, the residual water and ethanol are removed by magnetic separating and baking. Finally, the oil-based Fe_3O_4 nanofluid is obtained. The proper quantity of PDMS and oil-based Fe_3O_4 nanofluid are mixed to obtain the Fe_3O_4 nanofluid with high viscosity.

2.2 Fabrication of Transformers

This section describes the fabrication processes of the transformer on a capillary and the MEMS transformer on a wafer.

2.2.1 Fabrication of Transformer on a Capillary

The transformer on a capillary is simply made from the winding of enamel-insulated wire and a capillary used as the container of magnetic core. The air, bulk Fe_3O_4 and Fe_3O_4 nanofluids of 0.25M, 0.5M, 0.75M and 1M are applied as the

magnetic core. The bulk Fe_3O_4 is made by repeatedly dehydrating and baking the ethanol-based Fe_3O_4 nanofluid in the capillary. Figure 2.4 shows the structure of the transformer on a capillary which carries the oil-based Fe_3O_4 nanofluid. The diameter of applied enamel-insulated wire of #26 is 0.45mm, and the thickness of the enamel layer is near 0.05mm. Both the primary and secondary windings have 20 turns. The outer and inner diameters of capillary are respectively 3.2mm and 2.3mm, and the capacity of capillary is 100μl.

2.2.2 Fabrication of MEMS Transformer on a wafer

The MEMS transformer on a wafer is a solenoid type transformer, fabricated by the MEMS process. The fabrication process of the MEMS transformer is shown in Fig. 2.5. The detail procedures are described as follow:

1. Wafer cleaning: The surface of wafer is cleaned and coarsened by the reactive ion etch (RIE) with 50W power for 60 second. This step is to remove the impurities on the wafer and increase the adhesion between the wafer and materials.

2. Seed layer sputtering: The Cr layers of 0.05 μm thickness and the Cu layer of 3 μm thickness are sputtered sequentially on the wafer by a physical vapor deposition (PVD)

3. Line patterning: The surface of the metal layer is coated with the photoresist

EPG-512 by using a spin coater. The coating rotation speed and time are shown in Fig. 2.6(a). After spin coating, the photoresist layer of 1.5 μm thickness is baked under 110℃ for 1 minute. Then the photoresist is exposed with the mask 1 shown in Fig. 2.7(a) by the aligner with 150 mJ exposing power and developed by the TMAH solution of 2.38% concentration. The processed wafer after line patterning is shown in Fig. 2.8.

4. Wet etching and photoresist removing: Firstly, the Cu layer is etched by the etchant. The etchant consists of sulfuric acid and hydrogen peroxide solution. Then the Cr layer is etched by the potassium ferricyanide solution. After etching, the photoresist is removed by the remover. The processed wafer after metal etching is shown in Fig. 2.9

5. Electroplating: In order to reduce the resistance, the 6 μm Cu layer is electroplated on the seed layer with dipping in the $CuSO_4$ solution bath. And the 1 μm Au layer is electroplated with dipping in the potassium gold cyanide solution bath. The processed wafer after Cu and Au electroplating is shown in Fig. 2.10

6. Isolation layer patterning: In order to increase the adhesion between polyimide and wafer, the adhesive VM652 is coated on the wafer and baked under 120℃ for 2 minutes. The coating rotation speed and time are shown in Fig. 2.6(b). And the light-sensitive polyimide of 12 μm thickness is coated on the wafer and baked under

120℃ for 3 minutes. The coating rotation speed and time are shown in Fig. 2.6(c). Then the polyimide is exposed with the mask 2 shown in Fig. 2.7(b) by the aligner with 600 mJ exposing power, developed by the TMAH solution of 2.38% concentration and finally baked under 250℃ in the oxygen-deprived oven.

7. Dry film patterning: In order to increase the adhesion, RIE with 100W power is used to coarsen the surface of polyimide for 60 seconds. Two layers of dry film are attached on the wafer by the dry film machine. The temperature of roller of dry film machine is controlled at 105℃. Then the dry film is exposed with the mask 3 shown in Fig. 2.7(c) by the aligner with 150 mJ exposing power and developed by the sodium carbonate solution of 1% concentration. The processed wafer after dry film patterning is shown in Fig. 2.11.

8. Via electroplating and Die sawing: The 200 μm height metal pillars are electroplated with dipping in the $CuSO_4$ solution bath. The electroplated wafer is shown in Fig. 2.12. Then the wafer is cut according to the cutting line shown in Fig. 2.13. Finally, the protrudent Cu pillars are ground into flats.

9. Wire bonding: The wires are bonded on the wafer according to the Fig. 2.14. Then the wafer is bonded on a printed circuit board (PCB). The final testing sample is shown in Fig. 2.15. The oil-based Fe_3O_4 nanofluid will be loaded in the channel of wafer as a magnetic fluid core.

In order to verify the insulation of circuits under a high voltage, the insulativity of dry film is investigated. A self-made high voltage output device is used to test the insulativity of dry film. Figure 2.16 shows the circuit diagram of high voltage output device. The switching pulse width module (PWM) IC chip TL494 and two power MOSFET transistors IRF510 are used to cut the DC source into 56 kHz pulse. Then the voltage of pulse is stepped up by a transformer, rectified to DC and stepped up again by the voltage doublers. Figure 2.17 shows the photo of high voltage output device. The testing sample is a glass wafer coated the Cr/Cu layer and the dry film. The insulativity of dry film is investigated by applying a high voltage as shown in Fig. 2.18. The breakdown voltage of dry film with 100 μm thickness is over 5 kV, which indicates that the insulativity of dry film is high enough to endure the high surge.
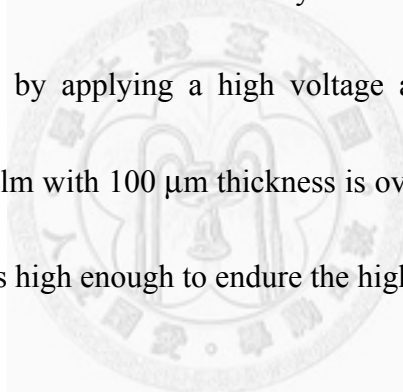
2.3 Experimental Procedure and Apparatus

This section describes the experimental procedure and apparatus for measuring the physical properties of nanofluids and the performance of transformers.

2.3.1 Physical Properties of Nanofluids

In this section, the experimental procedure and apparatus of measuring the thermal conductivity and viscosity of nanofluids are described. And measuring principles of

thermal conductivity and viscosity of nanofluids are also described.

For the experimental procedure, the controlled parameters are the viscosity of base fluids and the volume fraction of nanoparticles in nanofluids. According to the Einstein-Stokes's equation, the Brownian diffusion coefficient, D_B, is the function of temperature, diameter of nanoparticles and viscosity of fluid:

$$D_B = \frac{k_B T}{3\pi\mu d_p}$$
(2.3)

where k_B is Boltzmann constant, T is temperature, μ is viscosity of nanofluids, and d_p is diameter of nanoparticles. By increasing the viscosity of base fluids, the Brownian diffusion coefficient will decrease, which means that the influences of Brownian motion will be weakened. Then the thermal conductivity of dynamic part should decrease. It is reasonable to suppose that the measured thermal conductivity will gradually approach the static thermal conductivity. Finally, the thermal conductivity of static part will be measured solely in the experiment. The experimental setup contains three sections: a constant temperature water bath, a viscometer (LVDV-E, Brookfield), and a thermal property meter (model KD2, Decagon Devices, Inc.). The constant temperature water bath is used to keep the environment at a constant temperature while the sample is under measuring. For measuring the viscosity of nanofluids, the constant temperature water bath is connected to the viscometer by tubes to provide an environment of constant temperature 25℃ while the viscosity of sample fluid is being measured. For measuring

the thermal conductivity, the nanofluid is loaded in a test tube with 2cm diameter, and the test tube is immerged in the constant temperature water bath while the thermal conductivity is being measured. Then the long needlelike probe is immersed in the testing fluid to measure the thermal conductivity. The environment temperature outside the test tube is kept at 25℃ by a constant temperature water bath. The testing conductions of nanofluids are listed in Table 2.2.

For the principle of measuring the thermal conductivity, there are the two commonly used methods: the steady-state parallel plate method and the transient hot wire method [81]. To consider the convenience of measurement, the transient hot wire method is the most popular to measure the thermal conductivity of nanofluids. Theoretically, the length and thermal conductivity of hot wire are assumed to be infinite, and the diameter and thermal capacity of hot wire are assumed to be zero. In a homogenous and isotropic medium, the equation for radial heat conduction is given by [82]

$$\frac{\partial T}{\partial t} = \kappa \left(\frac{\partial^2 T}{\partial r^2} + r^{-1} \frac{\partial T}{\partial r} \right) \tag{2.4}$$

where T is the temperature, t is the time, κ is the thermal diffusivity, and r is the radial distance. When an electrically heated probe is immersed in a medium, the temperature which rises from an initial temperature, T_0, at some distance, r, from the probe is

$$T - T_0 = \left(\frac{q}{4\pi k}\right) Ei\left(\frac{-r^2}{4\kappa t}\right) \tag{2.5}$$

where q is the heat per unit length per unit time, k is the thermal conductivity of the medium, and Ei is the exponential integral function:

$$Ei(-a) = \int_a^\infty \left(\frac{1}{u}\right) \exp(-u)du = -\gamma - \ln\left(\frac{r^2}{4\kappa t}\right) + \frac{r^2}{4\kappa t} - \left(\frac{r^2}{8\kappa t}\right) + \dots \tag{2.6}$$

with $a=r^2/4\kappa t$ and γ is Euler's constant. When t is large, the high order terms can be ignored, so combining Eqs. (2.5) and (2.6) yields

$$\Delta T = T - T_0 \cong \frac{q}{4\pi k}\left(\ln(t) - \gamma - \ln\left(\frac{r^2}{4\kappa}\right)\right) \tag{2.7}$$

It is apparent from the relationship between thermal conductivity and $\Delta T = T - T_0$, shown in Eq. (2.7), that ΔT and $\ln(t)$ are linearly related with a slope $m=(q/4\pi k)$. Linearly regressing ΔT on $\ln(t)$ yields a slope that, after rearranging, gives the thermal conductivity as

$$k \cong \frac{q}{4\pi m} \tag{2.8}$$

In this study, the thermal conductivity of nanofluids is measured at 25 °C by a thermal property meter (model KD2, Decagon Devices, Inc.), which is based on the thermal hot wire method. All measurements are preformed over ten times and averaged.

For the principle of measuring the viscosity, there are several commonly used methods. In this study, the Searle viscometer is used to measure the viscosity of nanofluids. The advantage of the Searle viscometer is easy operation. But if the testing

33

fluid contains big particles of which the diameter approximates the gap between the cup and cylinder, the large error will occur. However, the size of nanoparticles is quite smaller than the gap, so that the error can be ignored. Figure 2.19 shows the schematic structure of Searle viscometer. The gap is filled with the testing fluid. As Figure 2.20 shown, the force dF and the torque dG on the unit area is expressed as:

$$dF = \tau_{r\theta}dA = \mu \dot{\gamma} dA = \mu\left(\frac{Ra \cdot \Omega}{H^*}\right)Ra \cdot Len \cdot d\theta \tag{2.9}$$

$$dG = Ra \cdot dF = \mu\left(\frac{Ra^3 \cdot Len \cdot \Omega}{H^*}\right)d\theta \tag{2.10}$$

where H^* is the distance between the cup and cylinder, Ra is the radius of cylinder, Len is the length of cylinder, and Ω is the angular velocity of cylinder. The entire torque can be obtained by integration:

$$G = \int dG = \int_0^{2\pi}\left[\mu\left(\frac{Ra^3 \cdot Len \cdot \Omega}{H^*}\right)\right]d\theta = \frac{2\pi\mu \cdot Ra^3 \cdot Len \cdot \Omega}{H^*} \tag{2.11}$$

After rearranging, the viscosity is given as:

$$\mu = \frac{GH^*}{2\pi Ra^3 \cdot Len \cdot \Omega} \tag{2.12}$$

By rotating the cylinder with a fixed angular velocity, a torque can be measured by the torque meter on the rotation axle. Then the viscosity of fluid can be calculated. In this study, the viscosity of nanofluids is measured at 25 °C by a Searle viscometer (LVDV-E, Brookfield).

34

2.3.2 Performance of Transformers

The controlled parameter in this section is the magnetic core of transformer. The solid magnetic core of traditional transformer has the property of hysteresis which causes the energy loss especially at high frequency. For this reason, the solid magnetic core is substituted with oil-based Fe_3O_4 nanofluids which possess the property of super-paramagnetism to reduce the hysteresis loss. On the other hand, because of the property of super-paramagnetism and the higher permeability than that of air, it is supposed that the transformer with the magnetic core of Fe_3O_4 nanofluids will have better performance than the air core transformer. For the model of transformer on a capillary, there are six kind materials loaded in the capillary for testing: air, bulk Fe_3O_4, Fe_3O_4 nanofluids of 0.25M, 0.5M, 0.75M and 1M. For the model of MEMS transformer on the wafer, air and 1M Fe_3O_4 nanofluids are applied as the magnetic core. The testing conditions of transformers are listed in Table 2.3. The impedance of transformer is measured by the precision impedance analyzer (4294A, Agilent Technologies). The photo of the precision impedance analyzer and the spring clip fixture are shown in Fig. 2.21. The measuring frequency ranges from 100 kHz to 100MHz. As Fig. 2.15 shown, the MEMS chip is fixed on the PCB board. And the transformer is connected to the precision impedance analyzer by wires. However, the inductance measured by this method includes the inductance of coils of transformer and the inductance of leading

wires connecting to the analyzer. Hence, a dummy shown in Fig. 2.22 is adopted to

eliminate the inductance of leading wires.
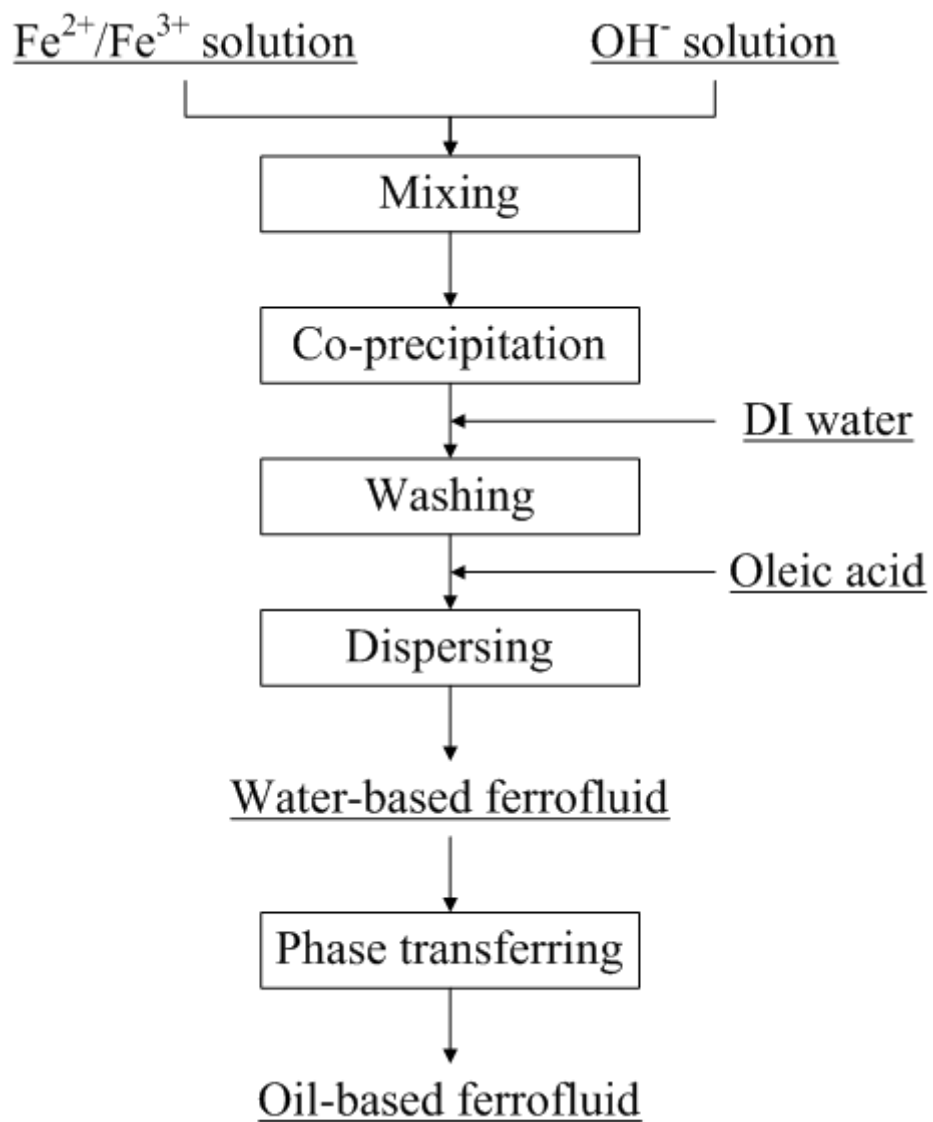
Figure 2.1 The flow chart of the precipitation procedure
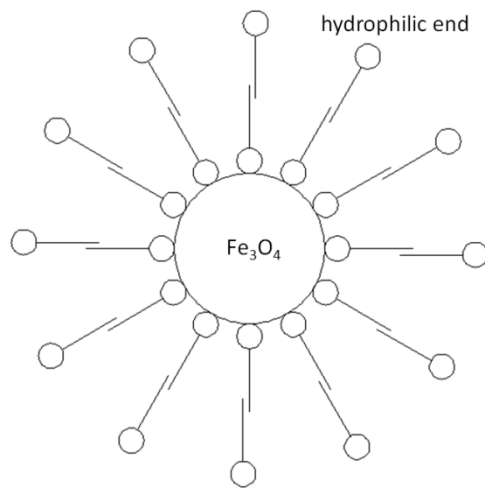
(a)
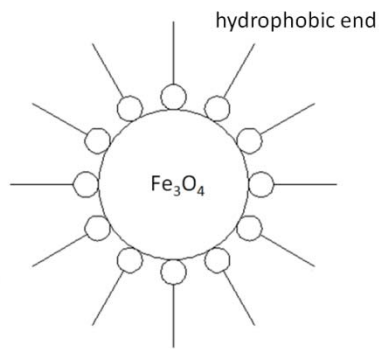
(b)

Figure 2.2 The adsorption model showing the relation between the surfactant and the

particle: (a) Model for water-based Fe_3O_4 nanofluid (b) Model for oil-based Fe_3O_4

nanofluid

Water-based ferrofluid

Washing ← Ethanol

Fe_3O_4 nanoparticles

← Diesel oil

Stirring and Vibrating

Purifying

Oil-based ferrofluid
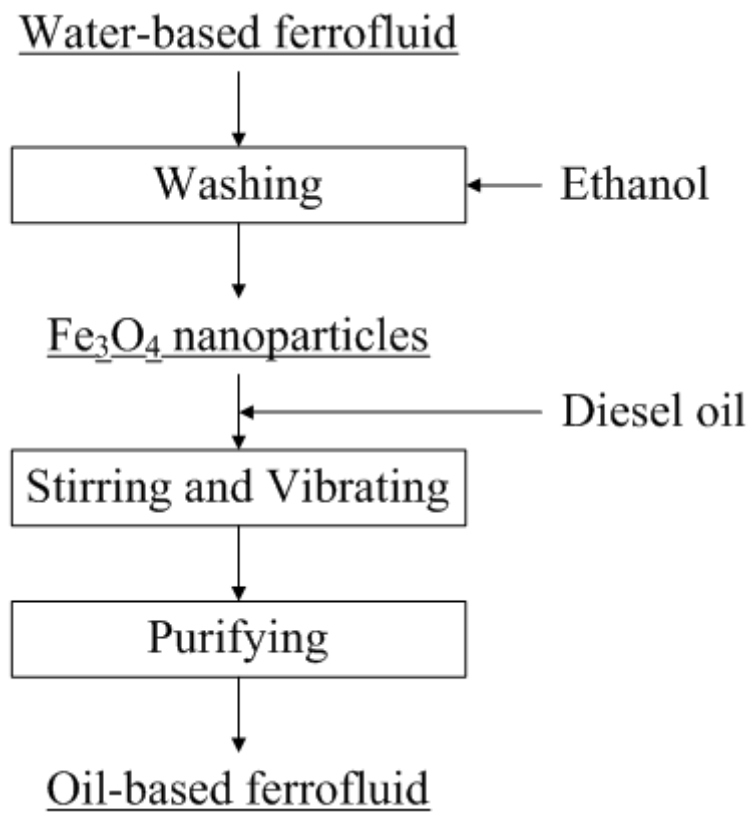
Figure 2.3 The procedure of phase transferring from water to oil
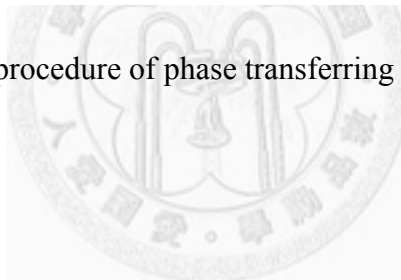
Figure 2.4 The photo of the transformer on a capillary which carries the oil-based Fe_3O_4

nanofluid

```
┌─────────────────────────────┐          ┌─────────────────────────────┐
│  Isolation layer patterning │          │      Wafer cleaning         │
└──────────────┬──────────────┘          └──────────────┬──────────────┘
               │                                         │
               ▼                                         ▼
┌─────────────────────────────┐          ┌─────────────────────────────┐
│     Dry film patterning     │          │    Seed layer sputtering    │
└──────────────┬──────────────┘          └──────────────┬──────────────┘
               │                                         │
               ▼                                         ▼
┌─────────────────────────────┐          ┌─────────────────────────────┐
│      Via electroplating     │          │      Line patterning        │
└──────────────┬──────────────┘          └──────────────┬──────────────┘
               │                                         │
               ▼                                         ▼
┌─────────────────────────────┐          ┌─────────────────────────────┐
│         Die sawing          │          │        Wet etching          │
└──────────────┬──────────────┘          └──────────────┬──────────────┘
               │                                         │
               ▼                                         ▼
┌─────────────────────────────┐          ┌─────────────────────────────┐
│        Wire bonding         │          │     Line electroplating     │
└─────────────────────────────┘          └─────────────────────────────┘
```
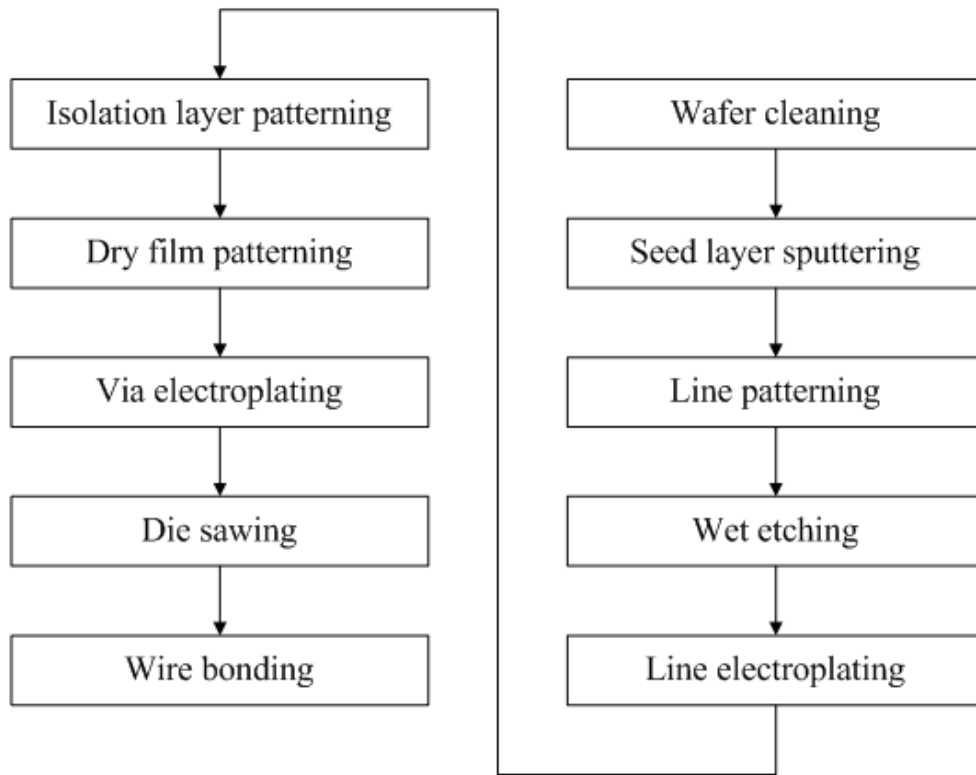
Figure 2.5 The fabrication process of the MEMS transformer

(a)
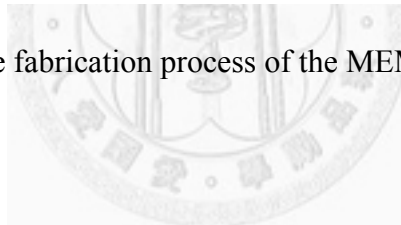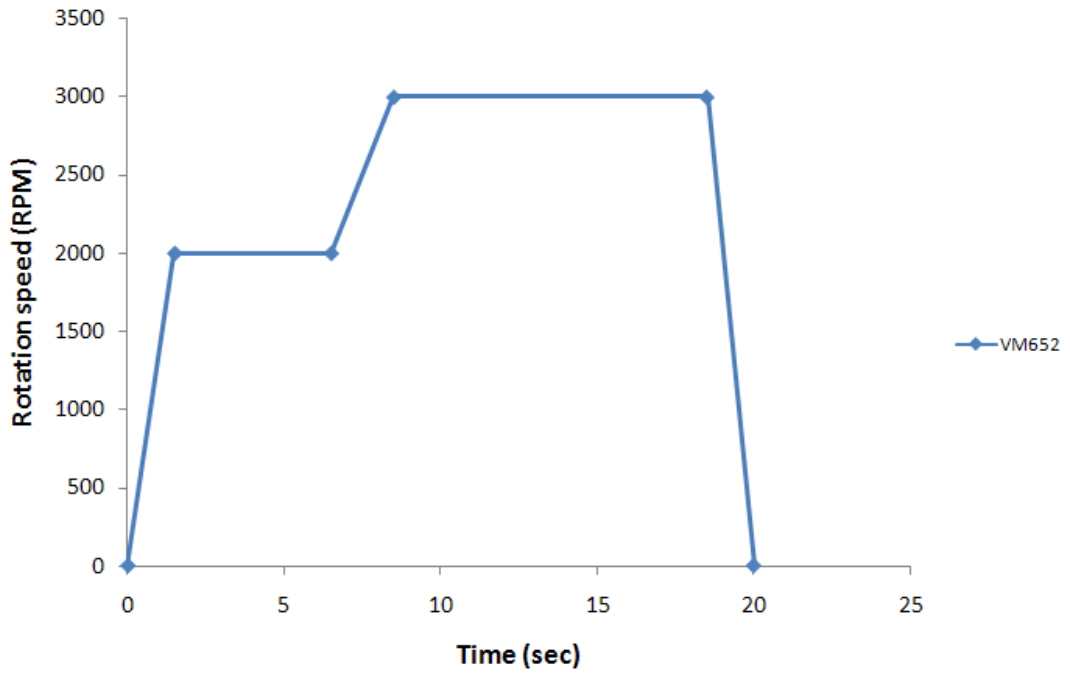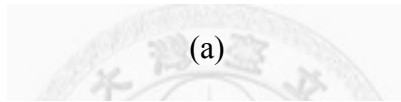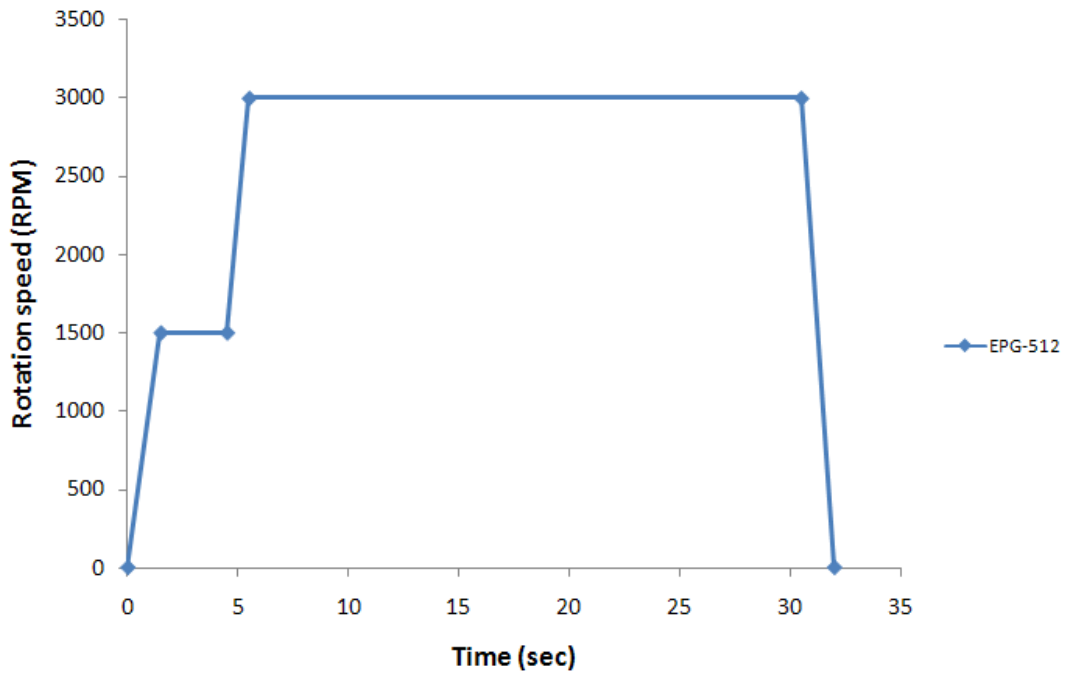
(b)
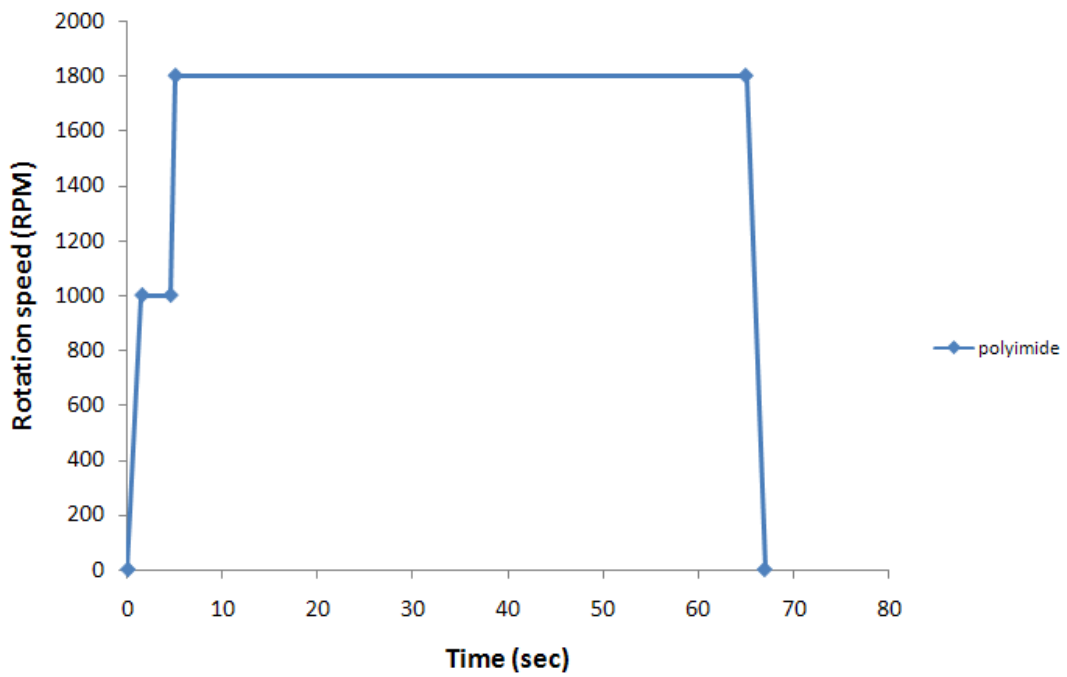
(c)

Figure 2.6 The diagram of the coating rotation speed versus time:

(a) EPG-512; (b) VM652; (c) polyimide

(a)

44
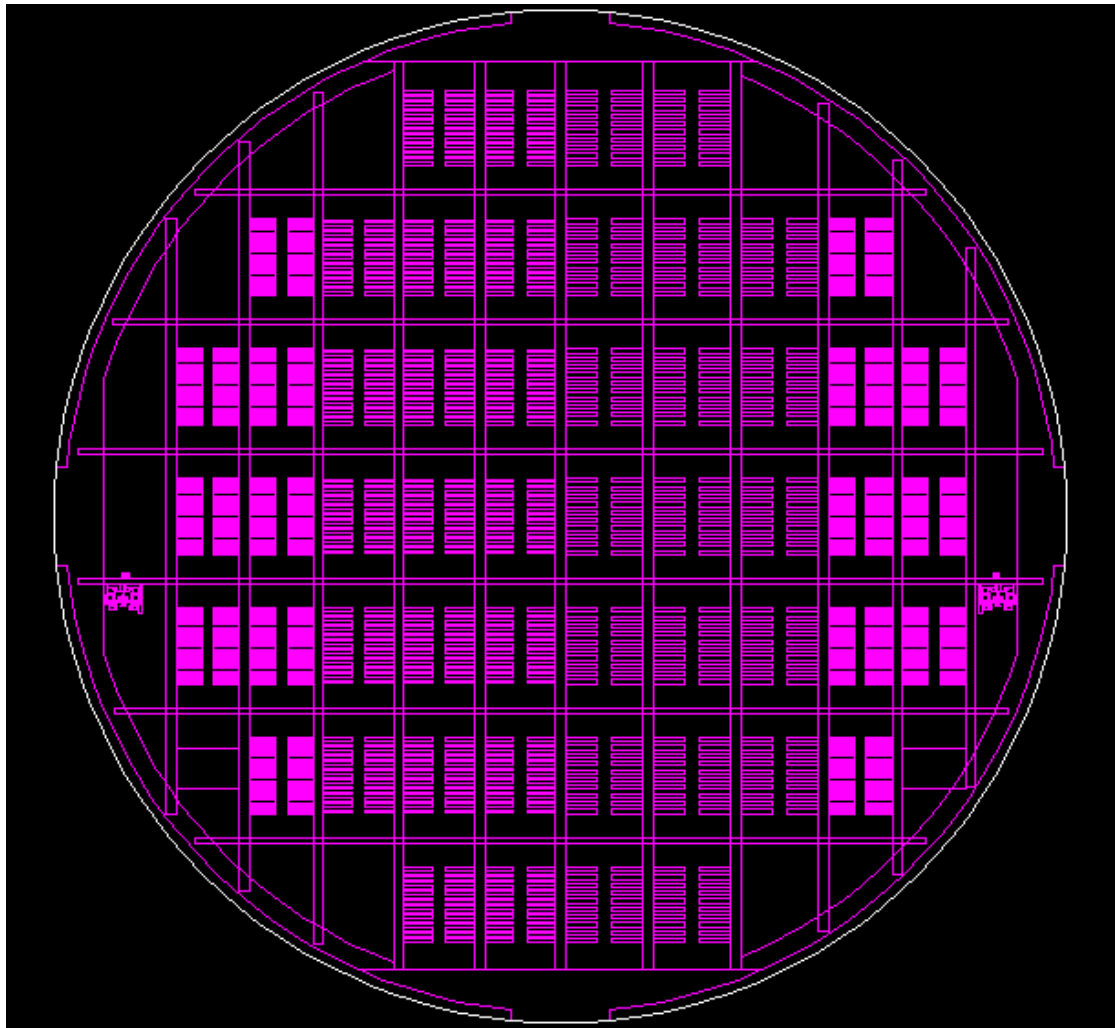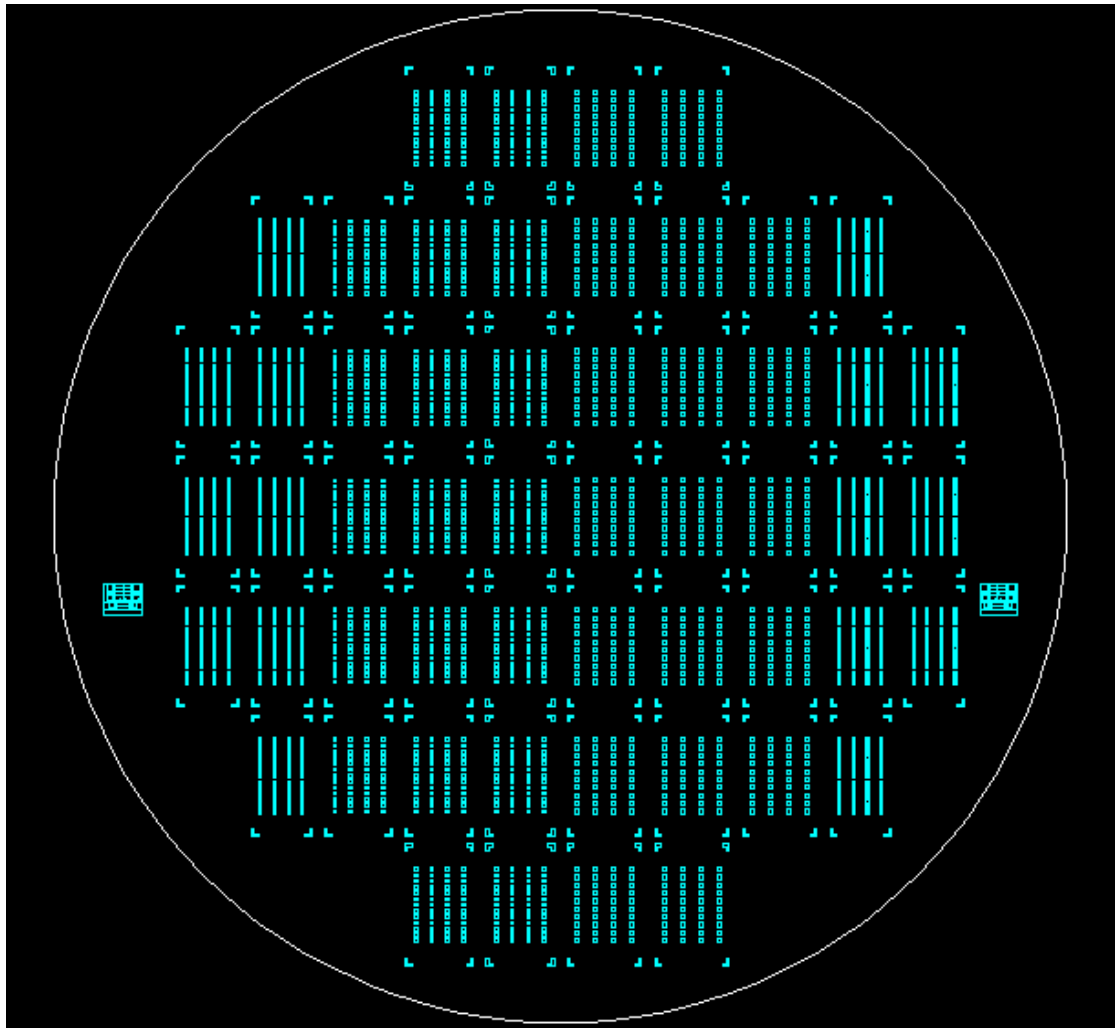
(b)
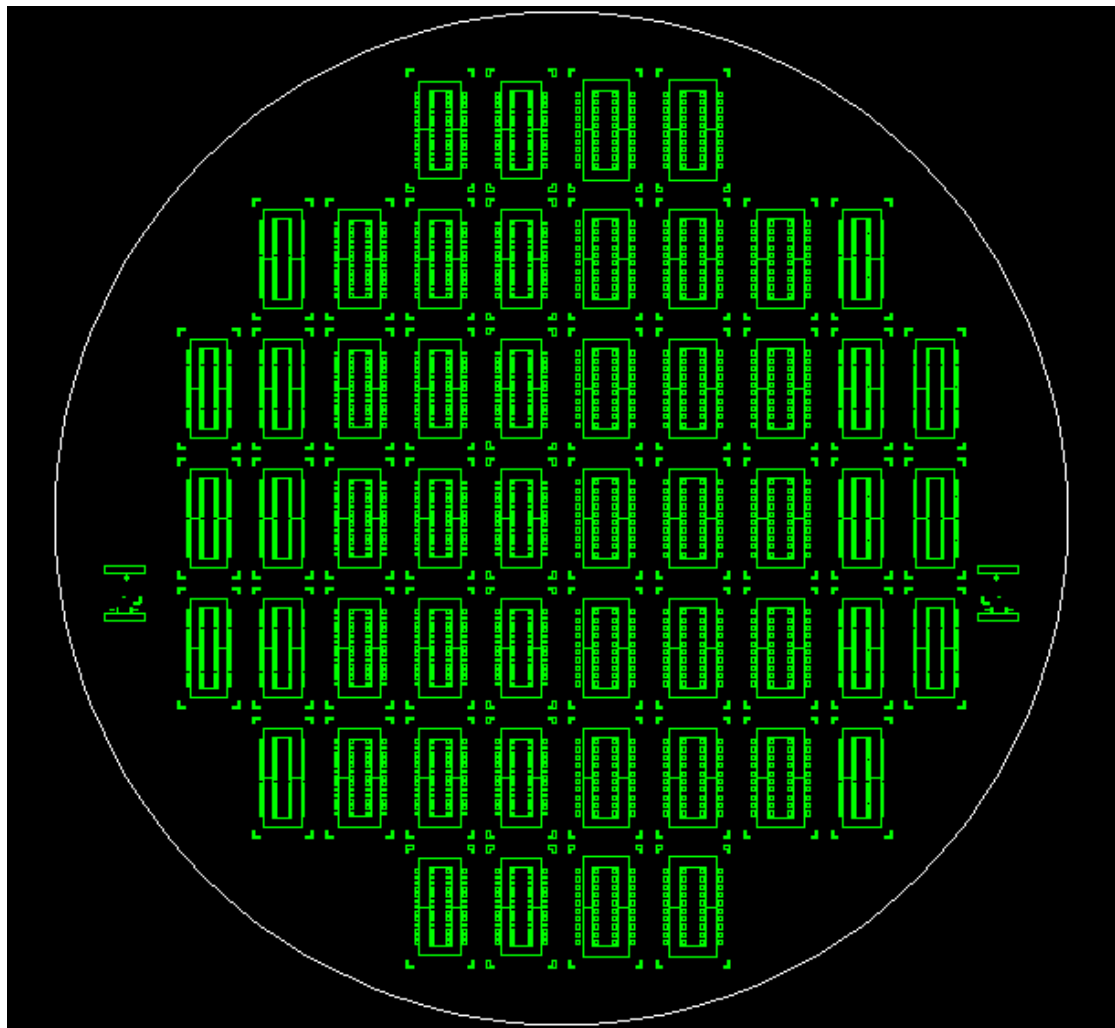
(c)

Figure 2.7 The masks for the photoresist: (a) EPG-512; (b) polyimide; (c) dry film
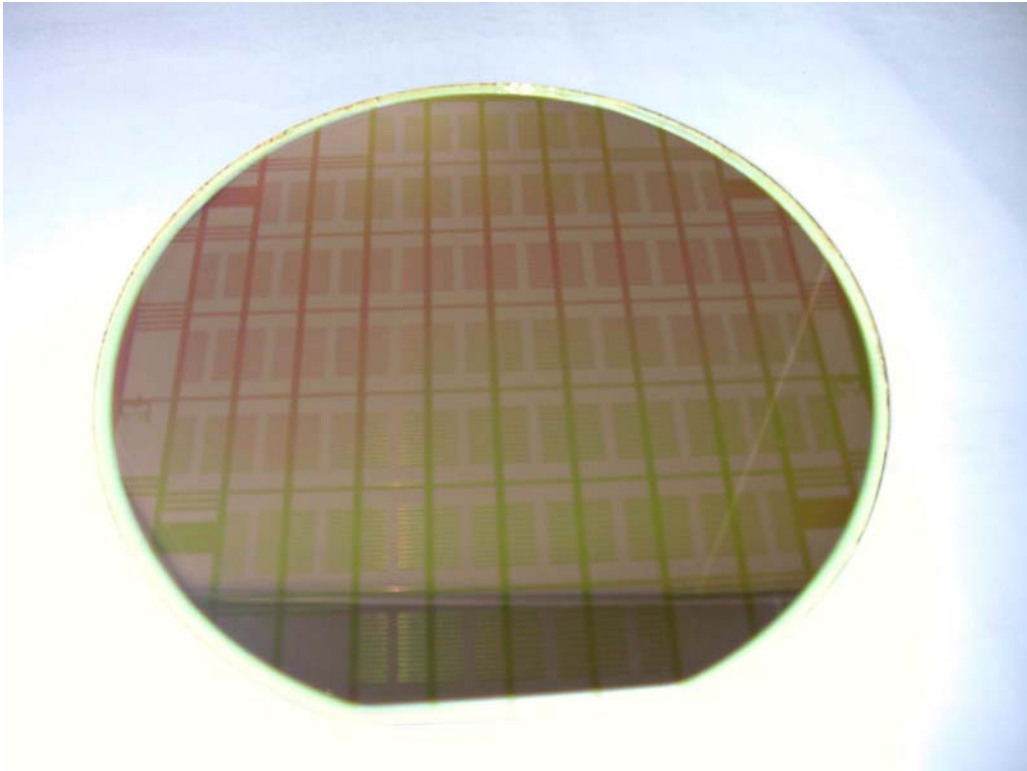
Figure 2.8 The photo of processed wafer after line patterning
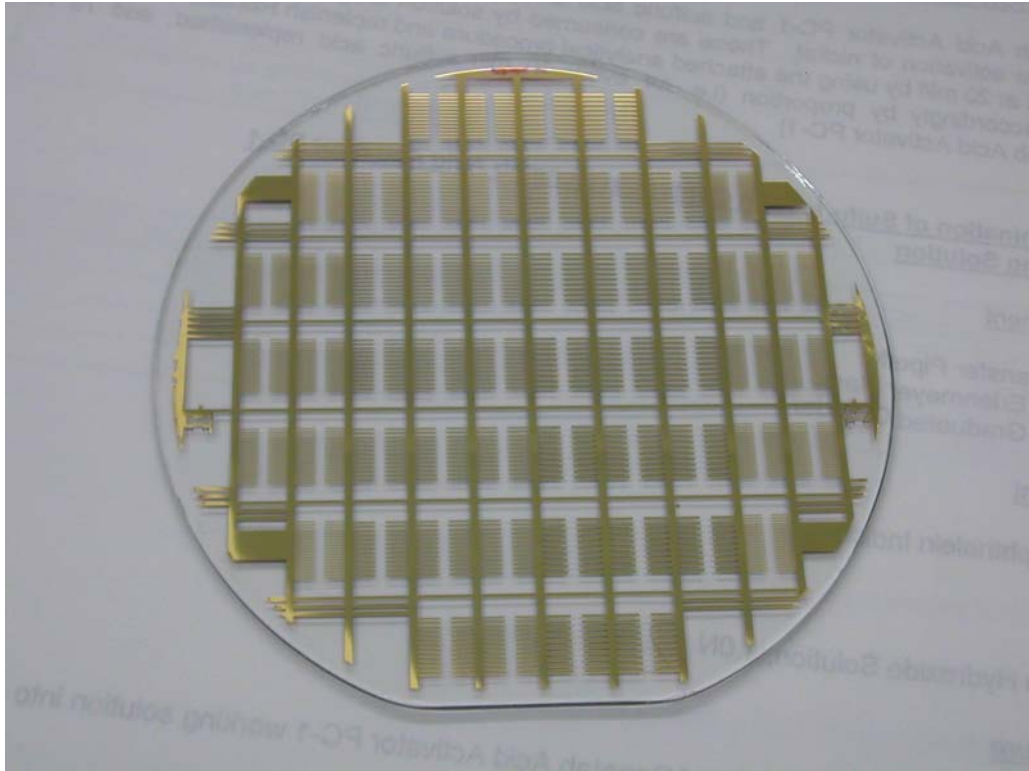
Figure 2.9 The photo of processed wafer after metal etching
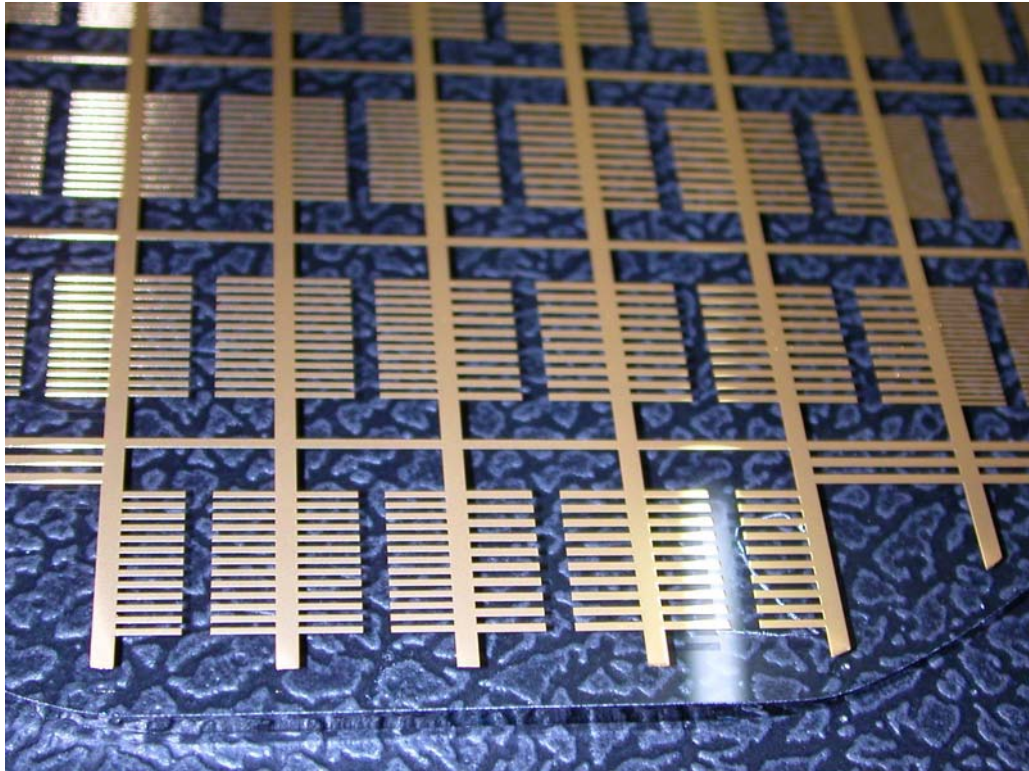
Figure 2.10 The photo of processed wafer after Cu and Au electroplating
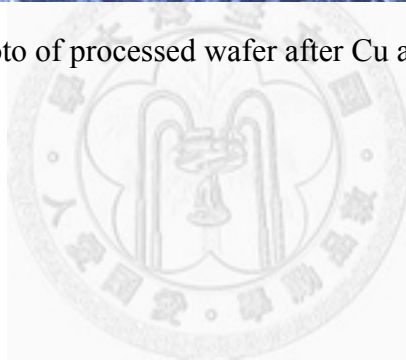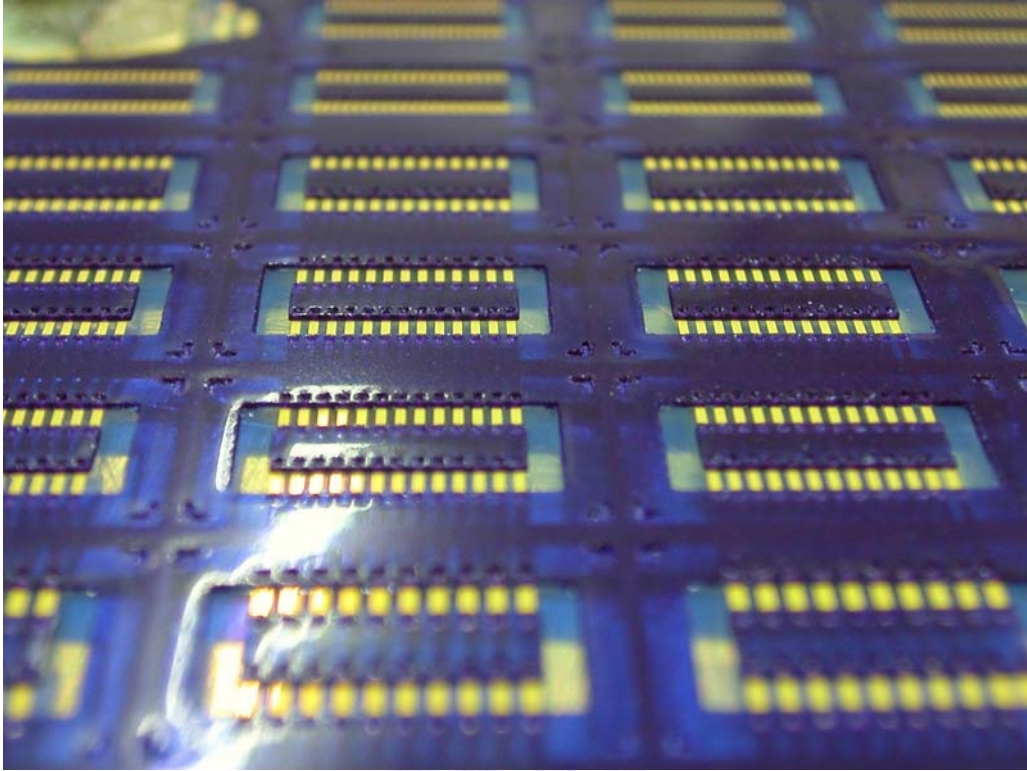
Figure 2.11 The photo of processed wafer after dry film patterning
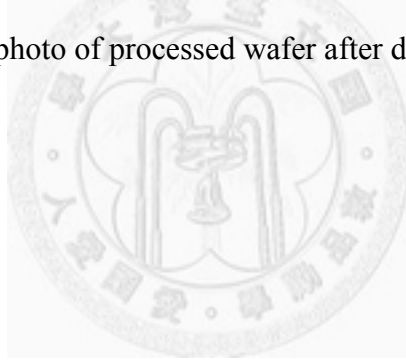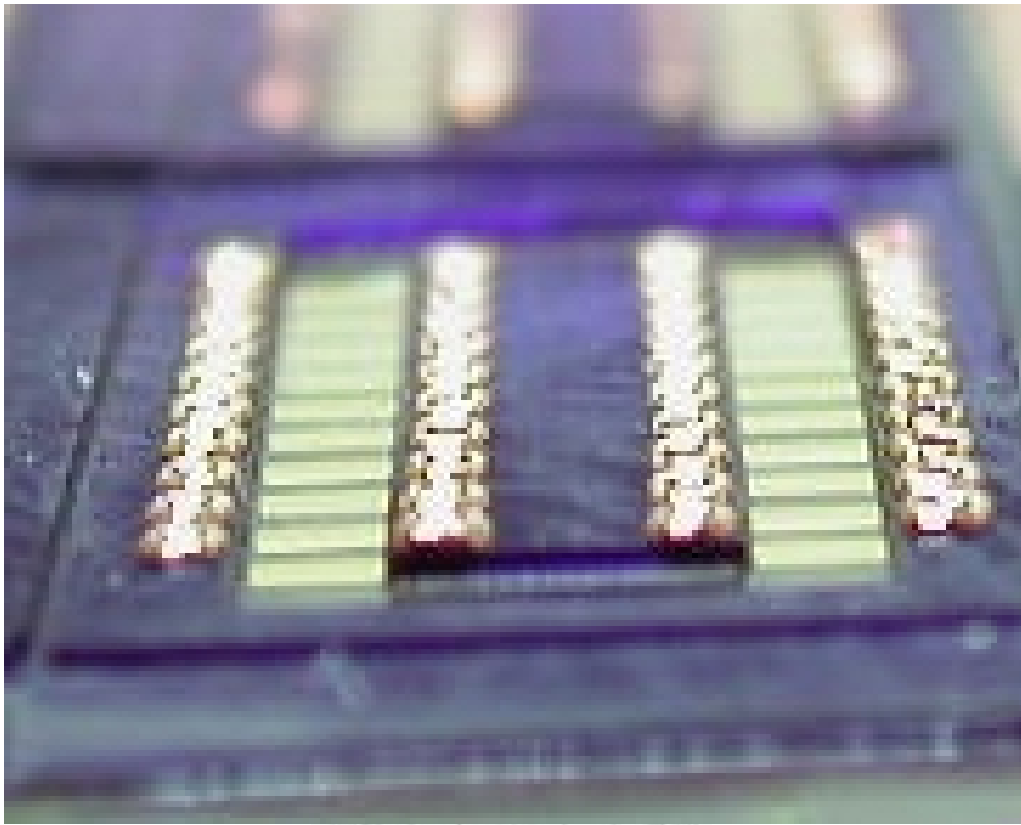
Figure 2.12 The photo of processed wafer after via electroplating
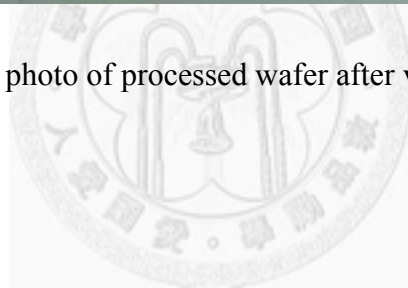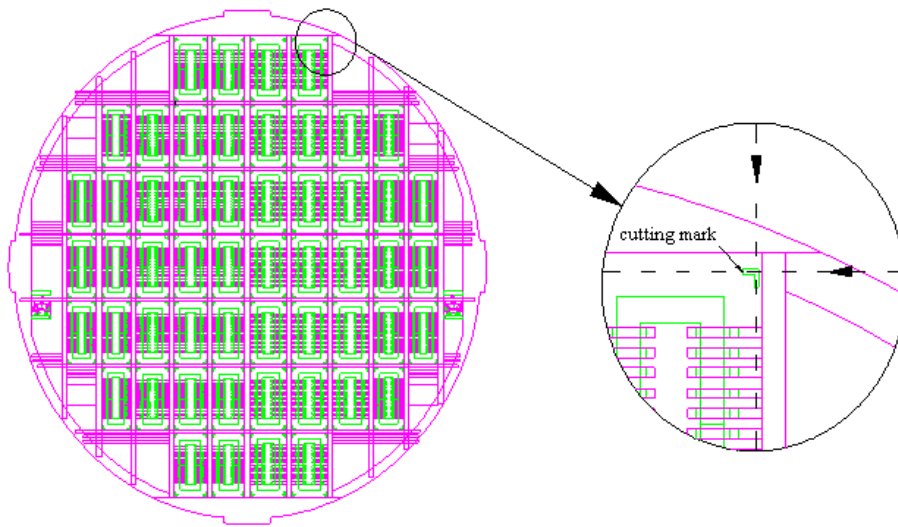
Figure 2.13 The diagram of wafer cutting line

Al wire
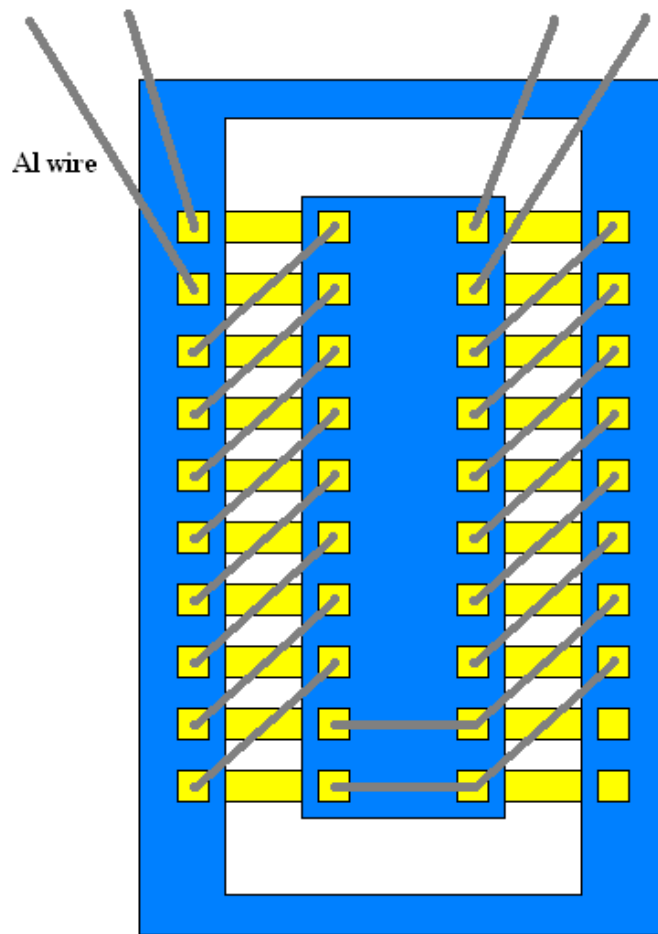
Figure 2.14 The schematic diagram of wire bonding
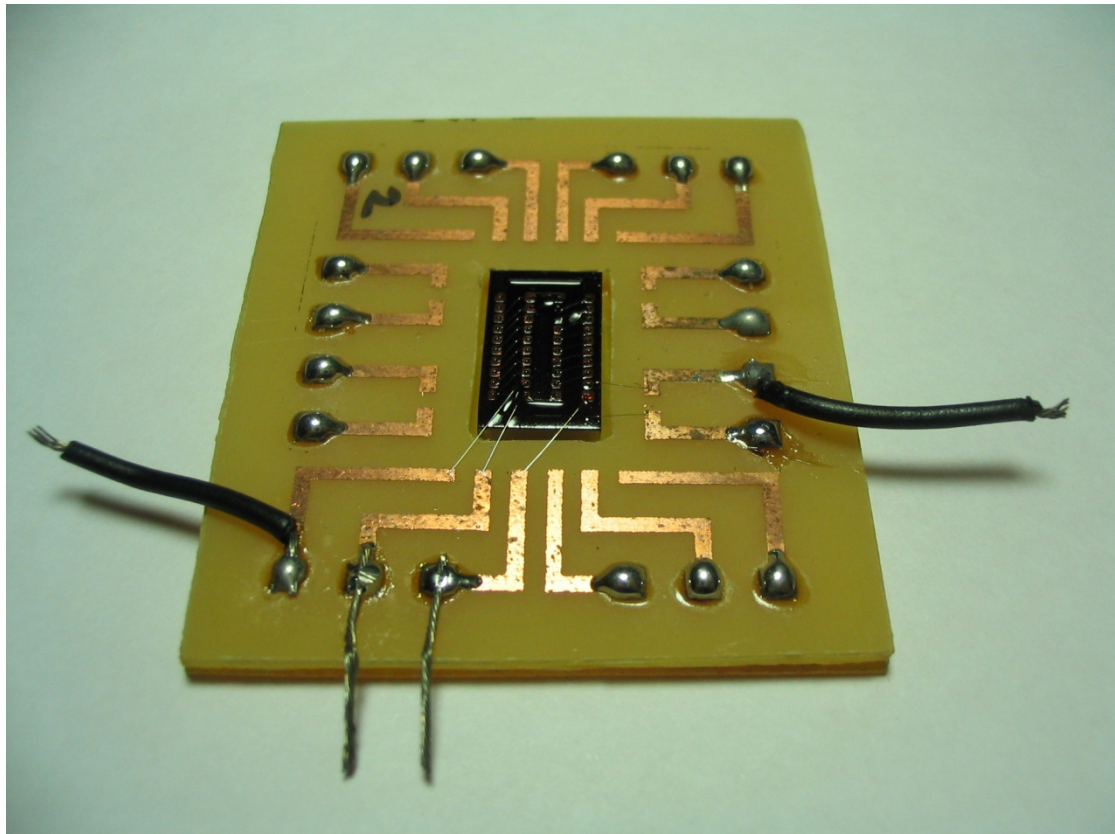
Figure 2.15 The measuring sample of MEMS transformer
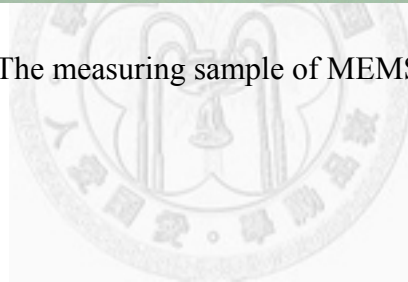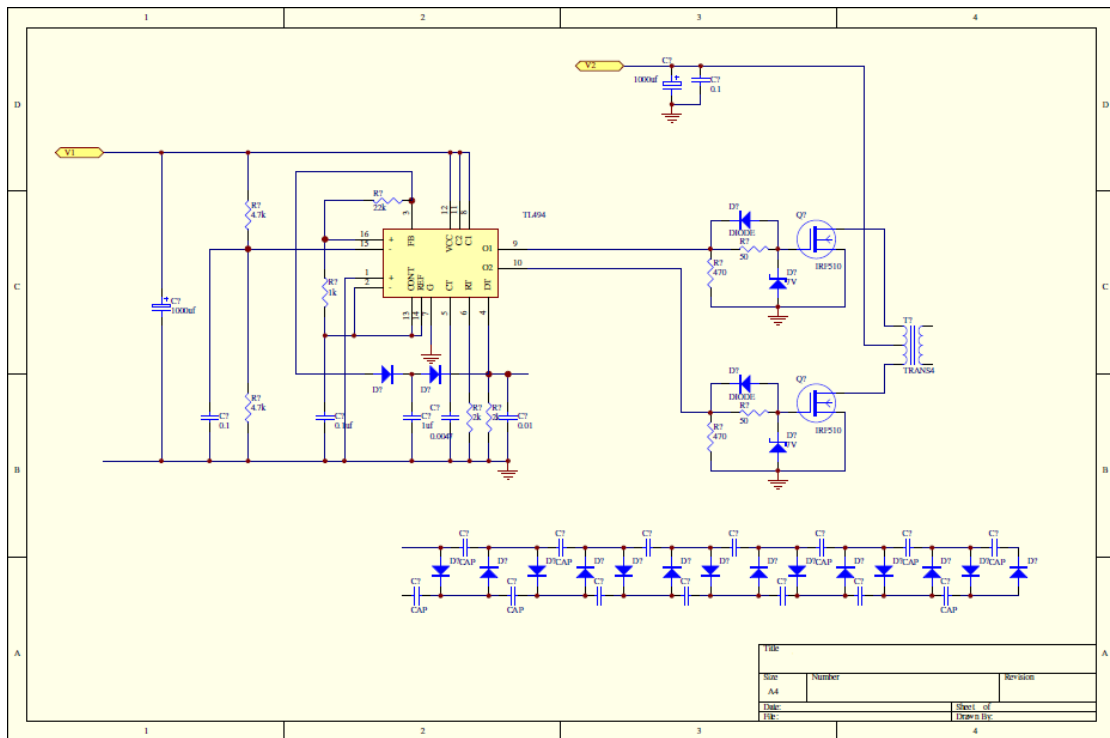
Figure 2.16 The circuit diagram of high voltage output device
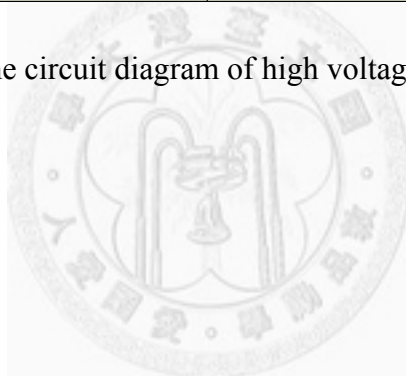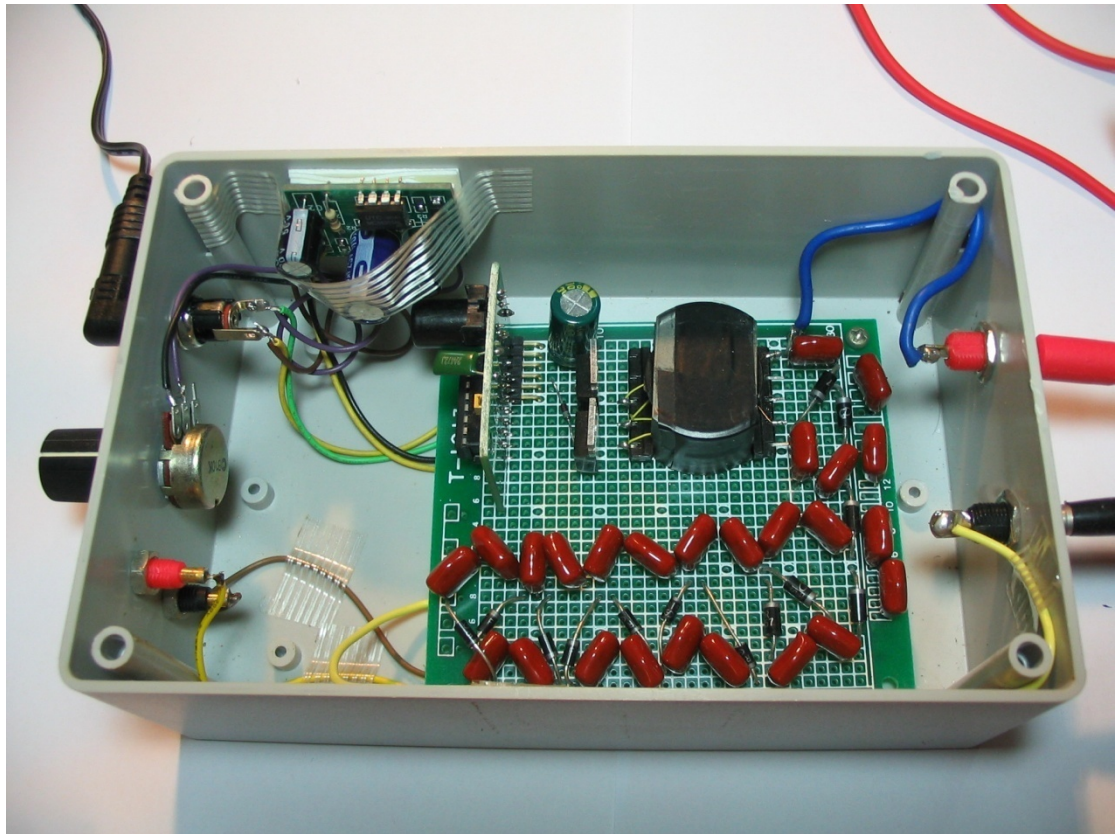
Figure 2.17 The photo of high voltage output device
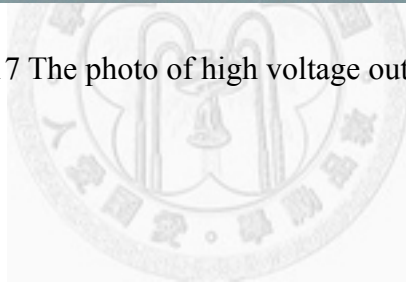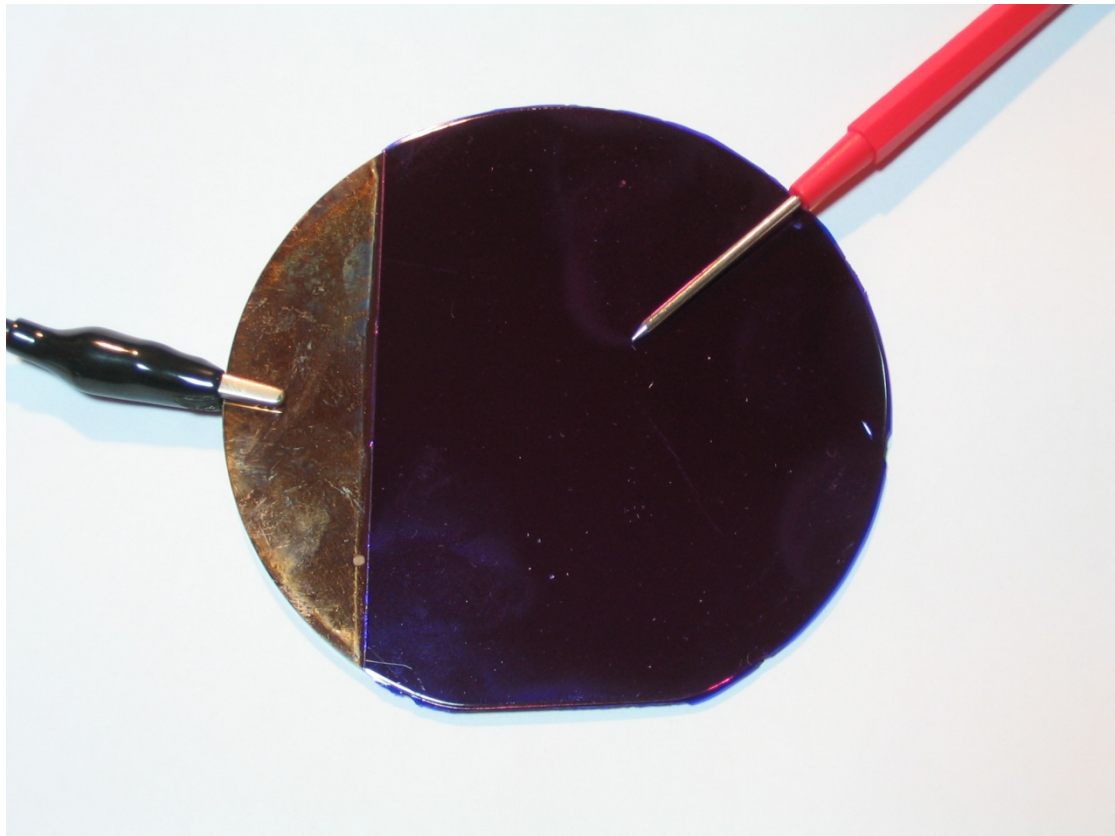
Figure 2.18 The photo of testing sample
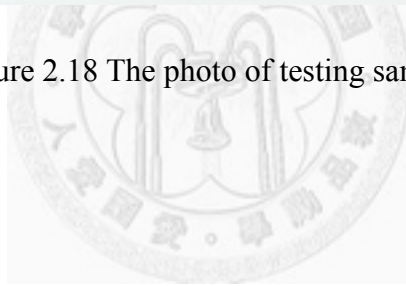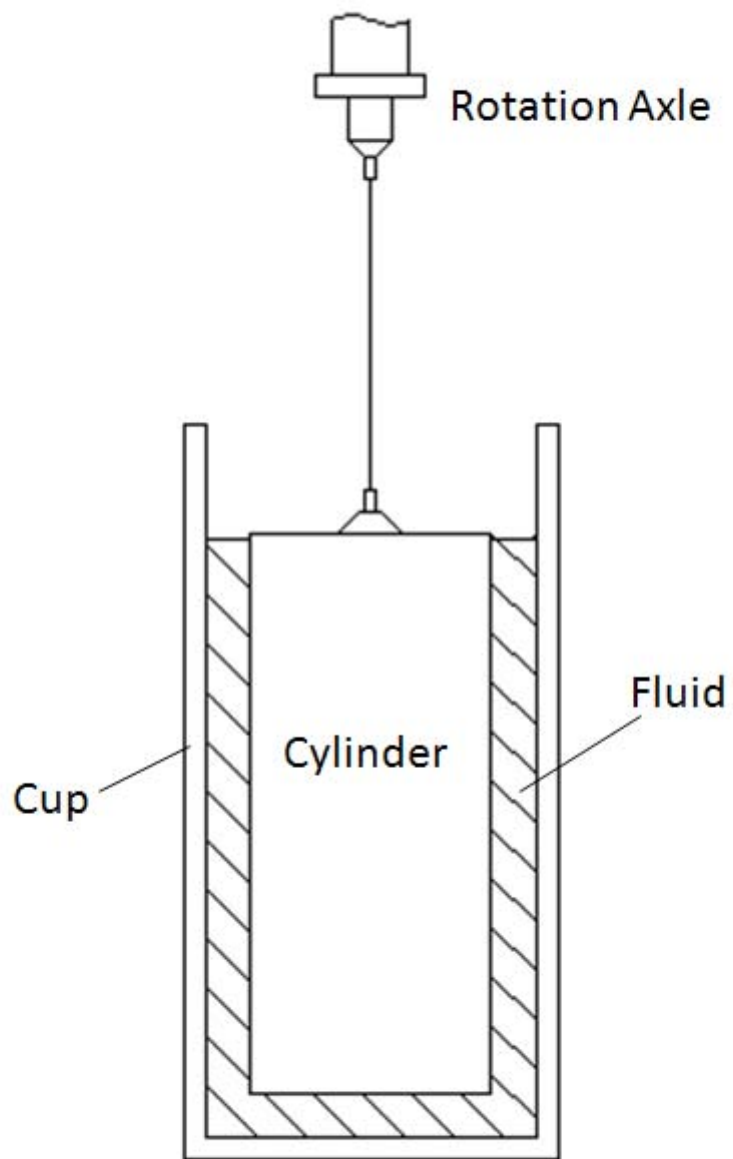
Figure 2.19 The schematic structure of Searle viscometer
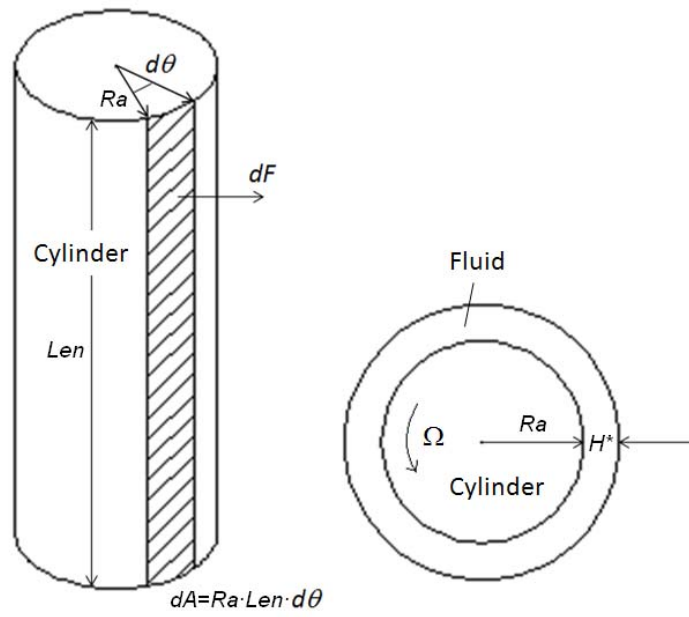
Figure 2.20 The free body diagram of the cylinder
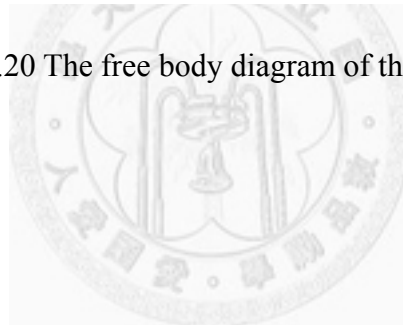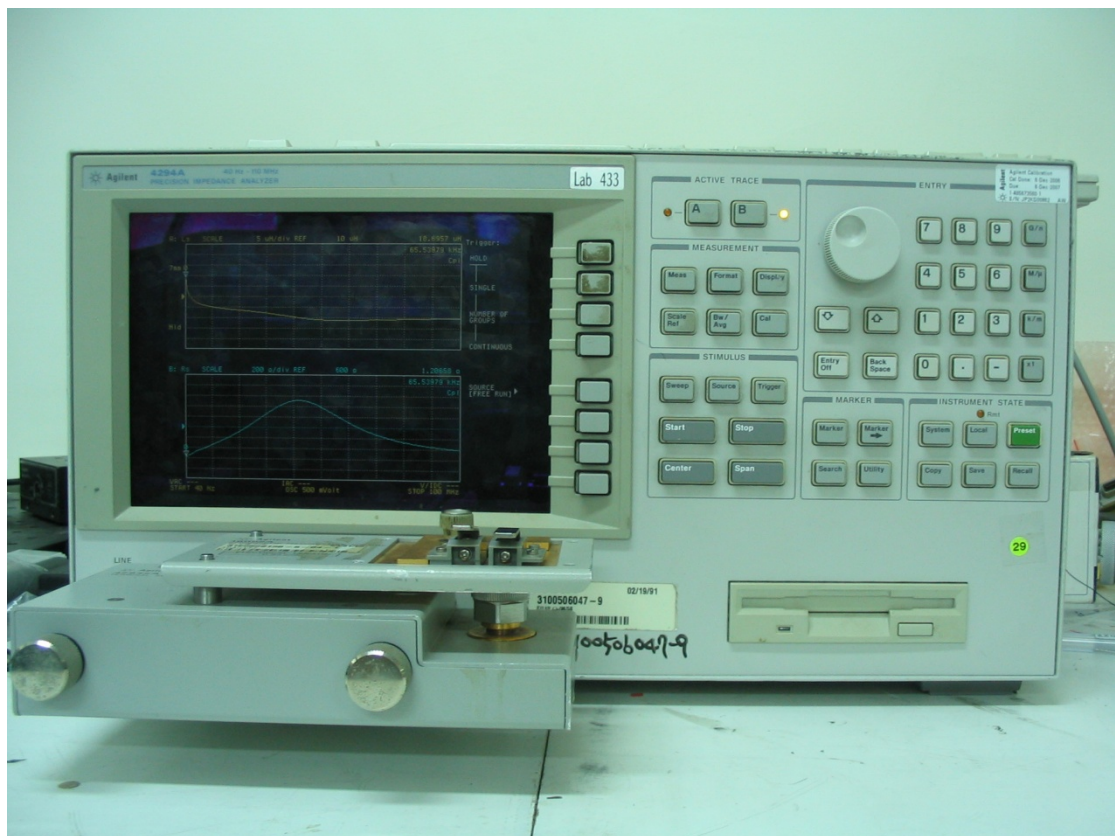
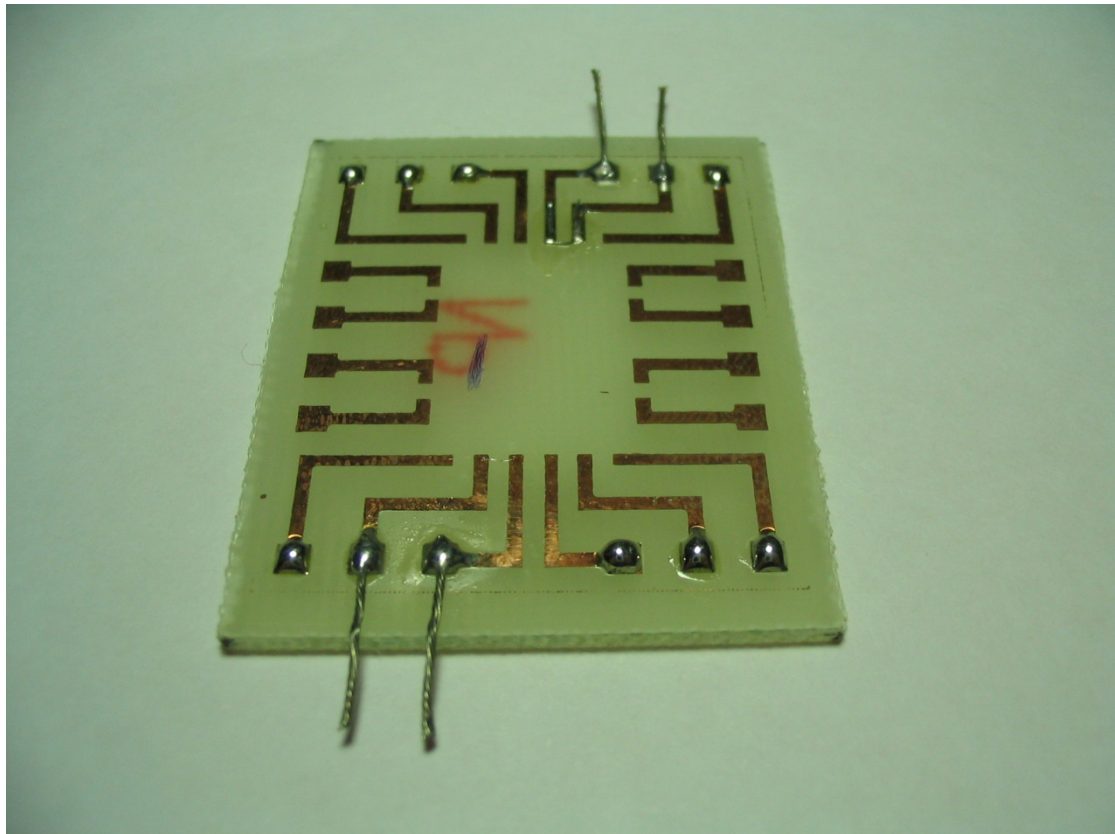Figure 2.21 The photo of the precision impedance analyzer and the spring clip fixture
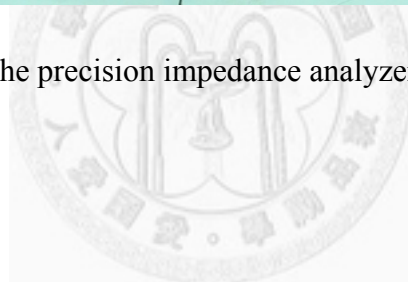
Figure 2.22 The photo of dummy PCB

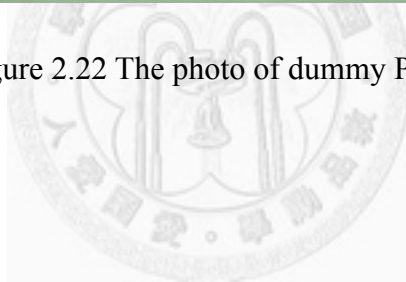Table 2.1 The chemical reagents used in the experiment

Chemical formula	Molecular weight (g/mol)	Manufacturer
$FeCl_2 \cdot 4H_2O$	198.81	J. T. Baker
$FeCl_3 \cdot 6H_2O$	270.30	Riedel-deHaen
NaOH	40.00	Riedel-deHaen
Oleic acid $CH_3(CH_2)_7CH=CH(CH_2)_7COOH$	282.46	J. T. Baker
Ammonia solution NH_3	17.03 (28%~30%)	J. T. Baker

Table 2.2 Testing conditions of nanofluids

Water-based Al_2O_3 nanofluids	
Composition of base fluid	Volume fraction of nanoparticles
100% water	2%
80% water + 20% EG	2%
60% water + 40% EG	2%
40% water + 60% EG	2%
20% water + 80% EG	2%
100% EG	2%
80% EG + 20% glycerol	2%
60% EG + 40% glycerol	2%
40% EG + 60% glycerol	2%
20% EG + 80% glycerol	2%
100% glycerol	2%
Oil-based Fe_3O_4 nanofluids	
Composition of base fluid	Volume fraction of nanoparticles
100% diesel oil	1.12%, 2.24%, 3.36%, 4.48%
75% diesel oil + 25% PDMS	1.12%, 2.24%
50% diesel oil + 50% PDMS	1.12%, 2.24%
25% diesel oil + 75% PDMS	1.12%, 2.24%

Table 2.3 Testing conditions of transformers

Transformer type	
Transformer on a capillary	MEMS transformer on a wafer
Materials of magnetic core	
Air	Air
Bulk Fe3O4	1M ferrofluid
0.25M ferrofluid	
0.5M ferrofluid	
0.75M ferrofluid	
1M ferrofluid	

Chapter 3 Physical Properties of Nanofluids

This chapter focuses on the thermal conductivity of nanofluids with different viscosities

of base fluids. The effect of viscosity of base fluid on thermal conductivity of nanofluids

is studied by applying various viscous base fluids. Two kinds of nanofluids, water-based

Al_2O_3 nanofluid and oil-based Fe_3O_4 nanofluid, are discussed in this chapter.
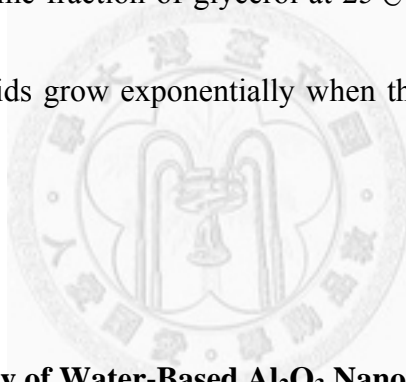
3.1 Water-Based Al_2O_3 Nanofluids

In this section, the physical properties, viscosity and thermal conductivity of Al_2O_3

nanofluids are sequentially discussed.

3.1.1 Physical Properties of Water-Based Al_2O_3 Nanofluid

Figure 3.1 shows the Field Emission Scanning Electron Microscopy (FESEM)

secondary electron image (SEI) of Al_2O_3 nanoparticles of which the diameter is around

10~15 nm [83]. The thermal conductivity of Al_2O_3 nanoparticles is about 37~39 W/m·k.

Other physical properties of Al_2O_3 nanoparticles can be found in Table 3.1 [83]. The

surface of Al_2O_3 nanoparticles is modified with sodium citrate. The sodium citrate is

hydrophilic and served as the surfactant.

3.1.2 Viscosity of Water-Based Al$_2$O$_3$ Nanofluids

For the water-based Al$_2$O$_3$ nanofluids, the compound of water and EG and the compound of EG and Glycerol, are applied as the two kinds of viscous base fluids. The measured viscosities of water, EG and glycerol are 1cP, 16.8cP and 937cP, respectively. These fluids are mixed with different ratios to obtain the base fluids with specific viscosities. Figure 3.2 shows the viscosities of the water-EG base fluids as a function of volume fraction of EG at 25℃. Figure 3.3 shows the viscosities of the EG-glycerol base fluids as a function of volume fraction of glycerol at 25℃. It can be observed that the viscosities of both base fluids grow exponentially when the volume fraction of EG or glycerol increases.

3.1.3 Thermal Conductivity of Water-Based Al$_2$O$_3$ Nanofluids

For the Al$_2$O$_3$ nanofluids, figure 3.4 shows the thermal conductivity of the water-EG based Al$_2$O$_3$ nanofluids and base fluids versus the volume fraction of EG, and figure 3.5 shows the thermal conductivity of the EG-glycerol based Al$_2$O$_3$ nanofluids and base fluids versus the volume fraction of glycerol. The measured thermal conductivities of water, EG and glycerol are 0.60446 W/m·k. 0.24932 W/m·k and 0.28314 W/m·k, respectively, and also a linear relationship is performed between the thermal conductivities of mixed base fluids and the mixing ratio. It can be also observed

that there are some enhancements on the thermal conductivity of Al_2O_3 nanofluids.

In order to detailedly quantify the enhancement on thermal conductivity of nanofluids and find out the relationship between the thermal conductivity and the viscosity of nanofluids, figure 3.6 and figure 3.7 shows the thermal conductivity ratio (k_{nano}/k_{bf}) of the water-EG based and EG-glycerol based Al_2O_3 nanofluids versus the volume fraction of EG and glycerol, respectively. (The parameters k_{nano} and k_{bf} denote the thermal conductivity of nanofluids and the base fluid, respectively.) It can be easily observed that there are enhancements on the thermal conductivity of Al_2O_3 nanofluids versus different viscosities. However, the enhancements on the thermal conductivity of Al_2O_3 nanofluids do not present any regular results. It may result from that the commercial Al_2O_3 nanoparticles are dry powder and cannot be dispersed in the base fluid well. The aggregation may cause the unstable thermal conductivity ratio of nanofluids.
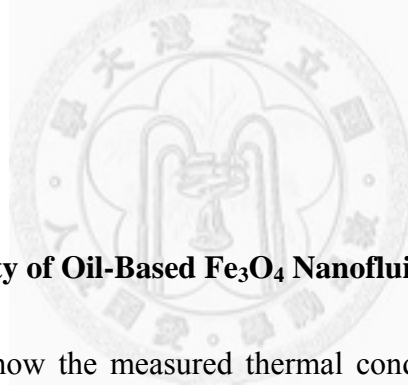
3.2 Oil-Based Fe$_3$O$_4$ Nanofluids

In this section, the physical properties, viscosity and thermal conductivity of Fe$_3$O$_4$ nanofluids are sequentially discussed.

3.2.1 Physical Properties of Oil-Based Fe$_3$O$_4$ Nanofluid

Figure 3.8 shows that the Fe$_3$O$_4$ nanofluid is attracted by a magnet. It is observed that the magnetic effect on the Fe$_3$O$_4$ nanofluid is large enough to overcome the gravity. Because of the function of surfactant, Fe$_3$O$_4$ nanoparticles are still dispersed well even under a strong magnetic field. The morphology and size of Fe$_3$O$_4$ nanoparticles are examined by a transmission electron microscope (TEM). Figure 3.9 shows the TEM photo of Fe$_3$O$_4$ nanoparticles of which the diameter is about 10nm. The crystalline phases of the Fe$_3$O$_4$ nanoparticles are determined by X-ray diffraction (XRD) as shown in Fig. 3.10. The magnetic properties of Fe$_3$O$_4$ nanofluid are measured by a vibrating sample magnetometer (VSM). The magnetized curve of the Fe$_3$O$_4$ nanofluid measured by a VSM is shown in Fig. 3.11. It illustrates the characteristic of super-paramagnetism. The saturated magnetizations of 0.25M, 0.5M, 0.75M and 1M Fe$_3$O$_4$ nanofluids are 3.75emu/g, 8.85emu/g, 12.7emu/g and 16.7emu/g, respectively. Other physical properties of Fe$_3$O$_4$ nanofluid can be found in Table 3.2.

3.2.2 Viscosity of Oil-Based Fe_3O_4 Nanofluids

For the oil-based Fe_3O_4 nanofluids, in order to obtain the viscous base fluids, diesel oil and PDMS, which have similar thermal properties and can be mixed uniformly, are adopted. The viscosity of diesel oil and PDMS are 4.18 cP and 5500 cP, respectively. By mixing different ratio of diesel oil and PDMS, the viscous base fluids with specific viscosities are obtained. Figure 3.12 shows the viscosities of the diesel oil-PDMS base fluids as a function of volume fraction of PDMS at 25°C. It can be also observed that the viscosity of base fluids grows exponentially when the volume fraction of PDMS increases.

3.2.3 Thermal Conductivity of Oil-Based Fe_3O_4 Nanofluids

Figure 3.13 to 3.16 show the measured thermal conductivity ratios, k_{nano}/k_{bf} and $k_{Maxwell}/k_{bf}$, of viscous Fe_3O_4 nanofluids versus the volume fraction of Fe_3O_4 nanoparticles at the viscosities of 4.18 cP, 31.8 cP, 140.4 cP and 648 cP, respectively. The predicted thermal conductivity of nanofluids, $k_{Maxwell}$, is determined by the Maxwell prediction model expressed by

$$k_{Maxwell} = \frac{k_p + 2k_{bf} + 2(k_p - k_{bf})\phi}{k_p + 2k_{bf} - (k_p - k_{bf})\phi} \tag{3.1}$$

where k_p is the thermal conductivity of nanoparticles, k_{bf} is the thermal conductivity of the base fluid, and ϕ is the volume fraction of nanoparticles. The thermal conductivities

of diesel oil and PDMS used in this section are 0.14 and 0.15 W/m·k, respectively.

In Fig. 3.13, 100% diesel oil is used as the low viscous base fluid (4.18 cP). The diagram shows that the thermal conductivity ratio (k_{nano}/k_{bf}) of Fe_3O_4 nanofluids grows linearly when the volume fraction of Fe_3O_4 nanoparticles increases. And the thermal conductivity ratio (k_{nano}/k_{bf}) is also higher than that predicted by the Maxwell prediction model. The enhancements of thermal conductivity are 8.74% and 18.85% at 2.24% and 4.48% volume fraction of Fe_3O_4 nanoparticles, respectively. And the thermal conductivity ratio compared with the Maxwell prediction model ($k_{nano}/k_{Maxwell}$) are 1.007, 1.021, 1.040, and 1.050 at 1.12%, 2.24%, 3.36%, and 4.48% volume fractions of Fe_3O_4 nanoparticles, respectively. The experimental results imply that in the low viscous base fluid, the Brownian motion and the convectionlike behavior are much active, which means the thermal conductivity of dynamic part is evident, and cause the observable enhancement on the thermal conductivity of Fe_3O_4 nanofluids.

In Fig. 3.14, the compound of 75% diesel oil and 25% PDMS is used as the middle viscous base fluid (31.8cP). The thermal conductivity ratio (k_{nano}/k_{bf}) of Fe_3O_4 nanofluids also grows linearly, and it is still a little higher than that predicted by the Maxwell prediction model. The enhancement of thermal conductivity is 7.55% at 2.24% volume fraction of Fe_3O_4 nanoparticles. In such middle viscous base fluid, the values of $k_{nano}/k_{Maxwell}$ are 1.006 and 1.01 at 1.12% and 2.24% volume fractions of Fe_3O_4

nanoparticles, respectively. Different form the case of low viscous base fluid, the Brownian motion and convectionlike behavior are decreased by the higher viscosity of base fluid, which means the thermal conductivity of dynamic part also decreases. This causes the fewer enhancements on thermal conductivity than that of low viscous Fe_3O_4 nanofluids.

In Fig. 3.15, the high viscous base fluid (140.4cP) which consists of 50% diesel oil and 50% PDMS is used. The thermal conductivity ratio (k_{nano}/k_{bf}) of Fe_3O_4 nanofluids becomes the same as that predicted by the Maxwell prediction model. The values of $k_{nano}/k_{Maxwell}$ in the high viscous base fluid are 1 at 1.12% and 2.24% volume fraction of Fe_3O_4 nanoparticles. At this situation, high viscosity of Fe_3O_4 nanofluids makes the Brownian motion and the convectionlike behavior disappear, which means that the thermal conductivity of dynamic part becomes zero. So the measured thermal conductivity of nanofluids only presents that of static part of which the value is the same with that predicted by the Maxwell prediction model.

In order to confirm the relationship between the thermal conductivity of static part and the Maxwell prediction model further, the extra highly viscous nanofluids are investigated. In Fig. 3.16, the extra highly viscous base fluid (648cP) that consists of 25% diesel oil and 75% PDMS is used. The values of $k_{nano}/k_{Maxwell}$ in the extra highly viscous fluid are 1 at 1.12% and 2.24% volume fraction of Fe_3O_4 nanoparticles. The

ratios, k_{nano}/k_{bf} and $k_{nano}/k_{Maxwell}$, are all the same with those of the case with high viscous base fluid (140.4cP) shown in Fig. 3.15.

3.3 Discussions

To generalize above cases, figure 3.17 shows the effect of viscosities of base fluids on the thermal conductivity of Fe_3O_4 nanofluids with 1% and 2% volume fractions of Fe_3O_4 nanoparticles. As the curve shows, the thermal conductivity of Fe_3O_4 nanofluids decreases with increasing viscosity and finally approaches a constant value. And it is observed that the viscosity around 100cP is a critical value of demarcation. Below viscosity of 100cP, the Brownian motion and the convectionlike behavior are more active so that the thermal conductivity of dynamic part is more apparent, and the measured thermal conductivity has a higher value than that of Maxwell prediction model. Over the viscosity of 100cP, the Brownian motion and the convectionlike behavior become inactive so that the thermal conductivity of dynamic part vanishes. In other words, the measured thermal conductivity of nanofluids only presents that of static part of which the value is the same with that predicted by the Maxwell prediction model. These results improve the confidence in believing that the viscosity of base fluid does influence the thermal conductivity of nanofluids, and the thermal conductivity of static

part should be based on the Maxwell prediction model.

On the other hand, because the base fluid used in this experiment is composed of two different fluids, diesel oil and PDMS, the difference in the interfacial thermal resistance [84] should be considered. However, the surface of the Fe_3O_4 nanoparticle is modified by the surfactant, which makes strong bonding strength between nanoparticles and base fluids. And the contact angles between components of viscous base fluids and bulk Fe_3O_4 are less than 5° as shown in Fig. 3.18, which indicates a wetting system [85]. For the reason above, the interfacial thermal resistance is speculated to be small and play a minor role in this experiment.
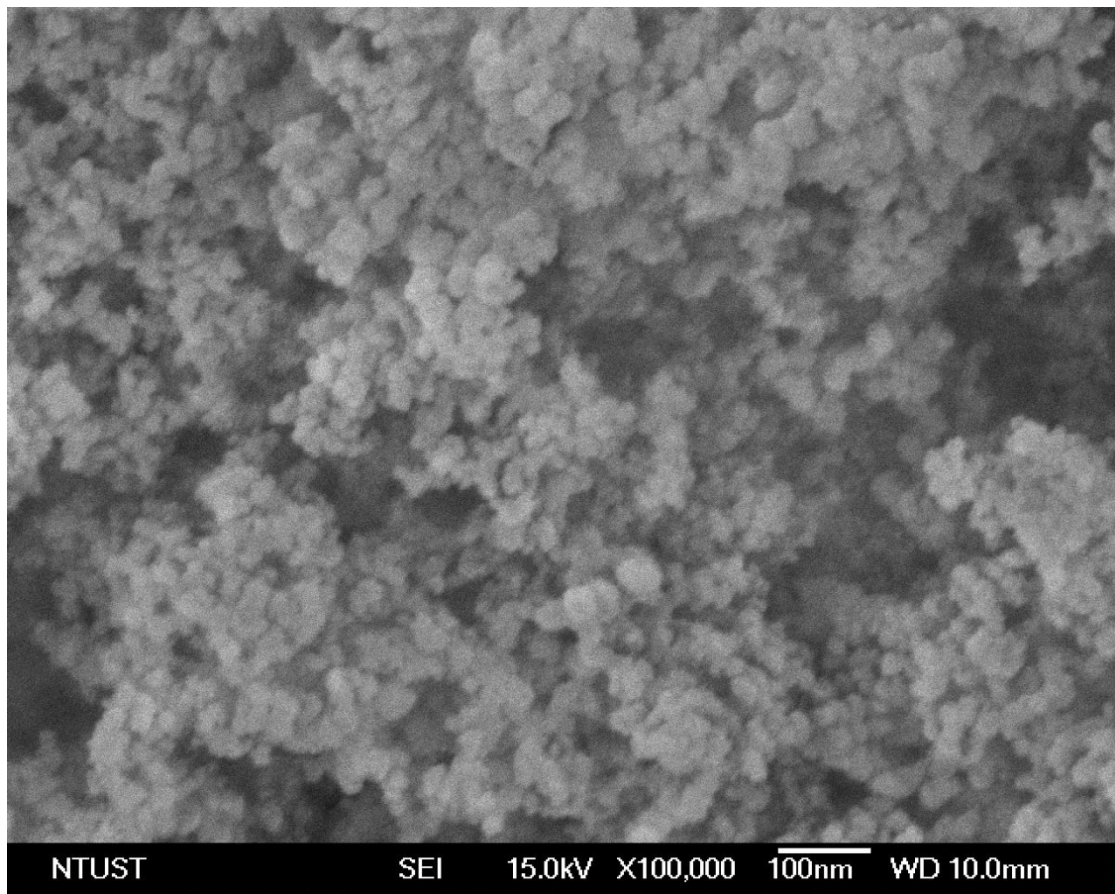
Figure 3.1 FESEM SEI of Al$_2$O$_3$ nanoparticles
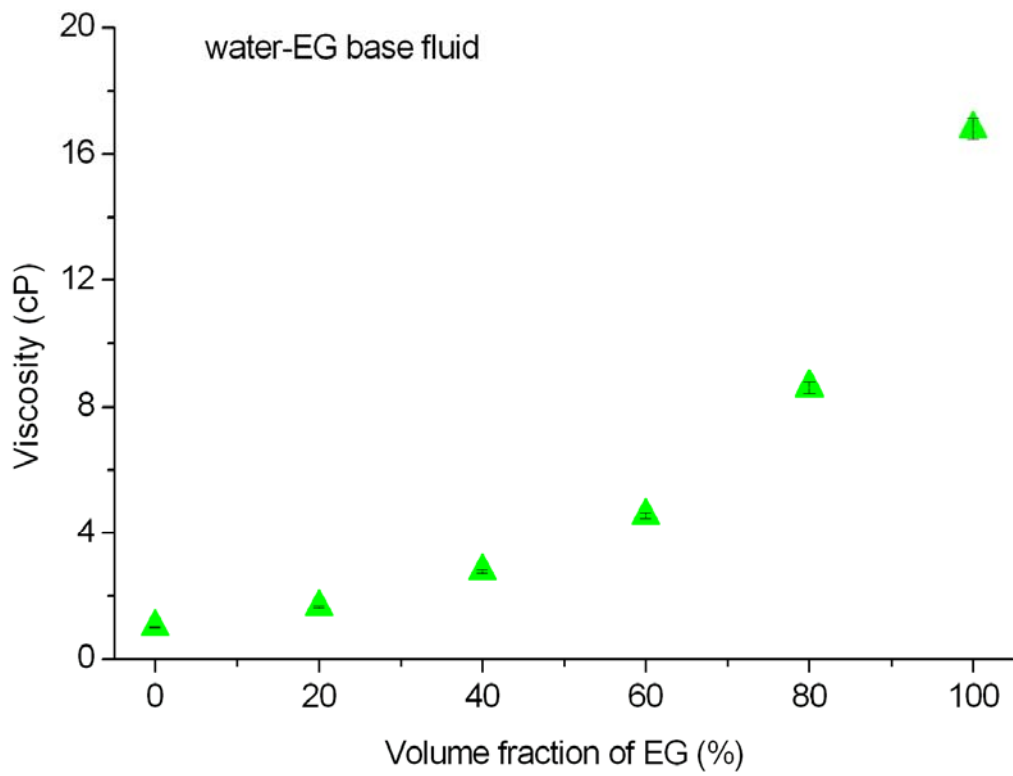
Figure 3.2 The Measured viscosities of the water-EG base fluids as a function of volume
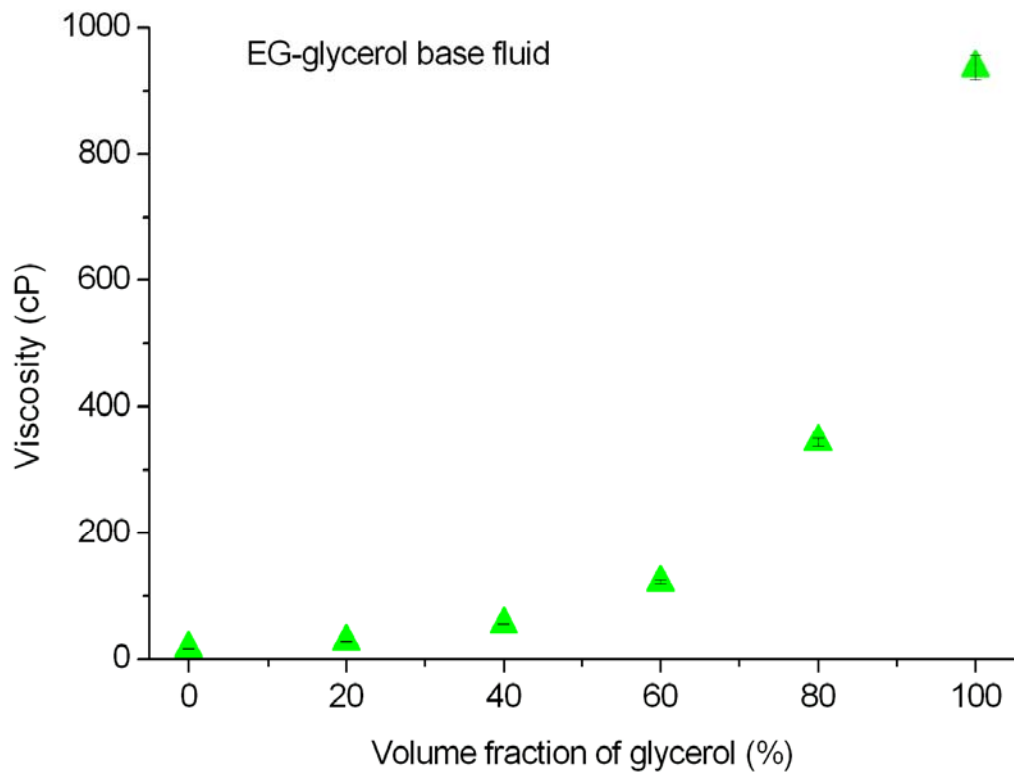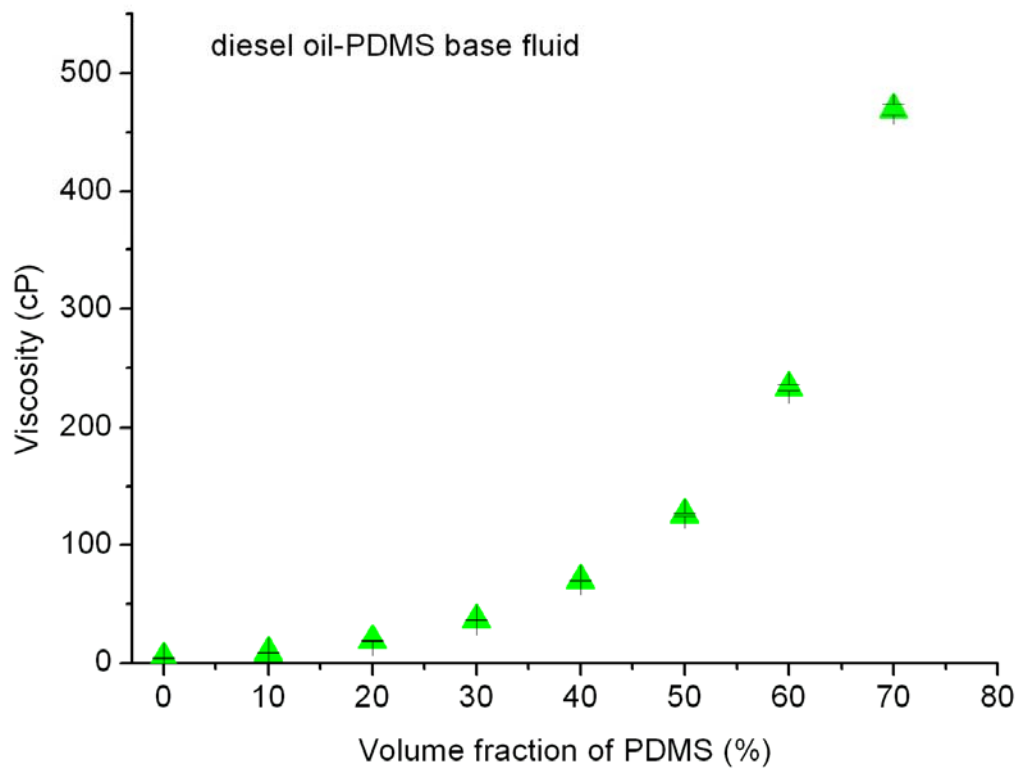
fraction of EG at 25℃

Figure 3.3 The Measured viscosities of the EG-glycerol base fluids as a function of

volume fraction of glycerol at 25℃
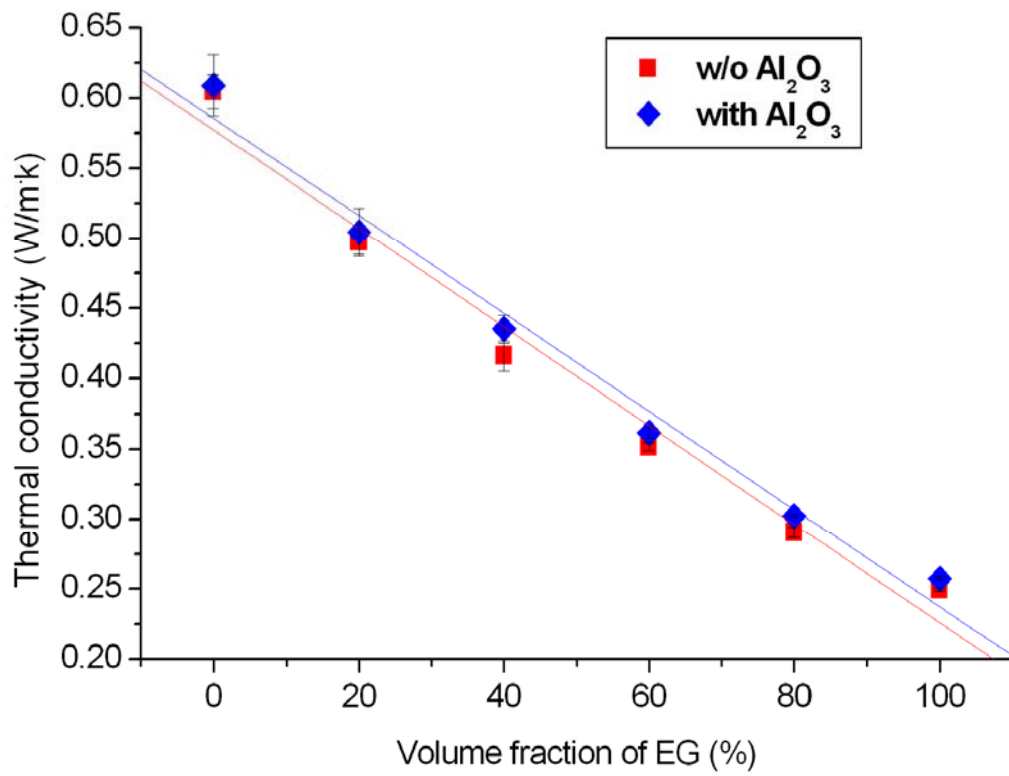
Figure 3.4 The thermal conductivity of the water-EG base fluid and Al$_2$O$_3$ nanofluid

versus the volume fraction of EG
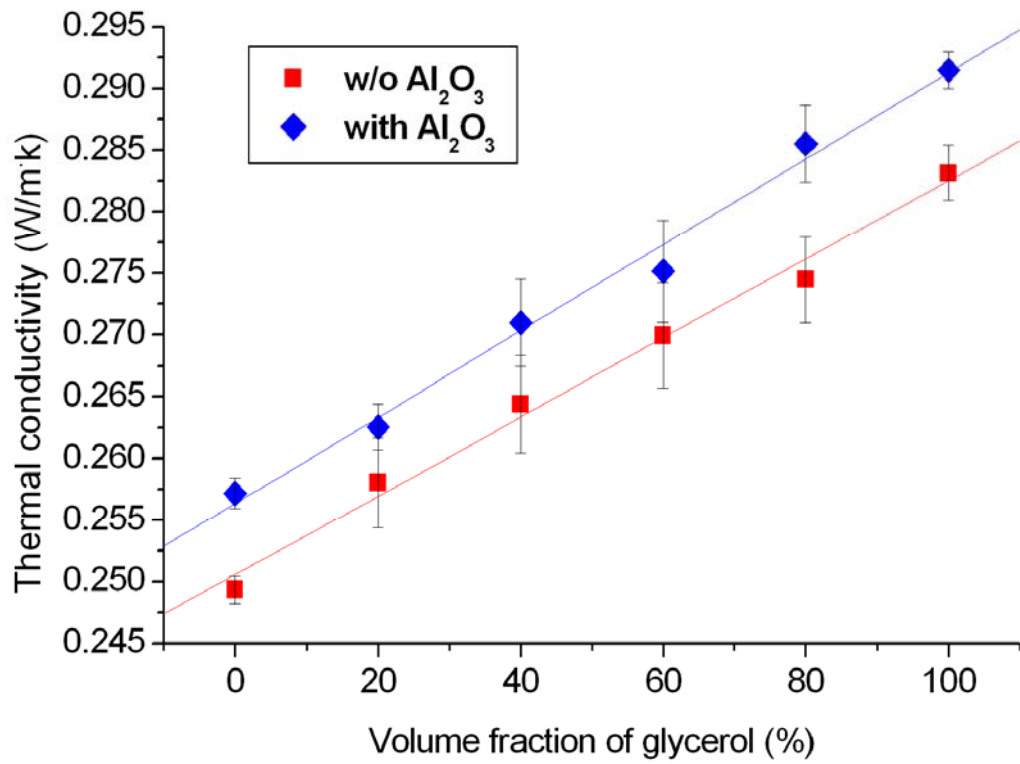
Figure 3.5 The thermal conductivity of the EG-glycerol base fluid and Al$_2$O$_3$ nanofluid

versus the volume fraction of glycerol
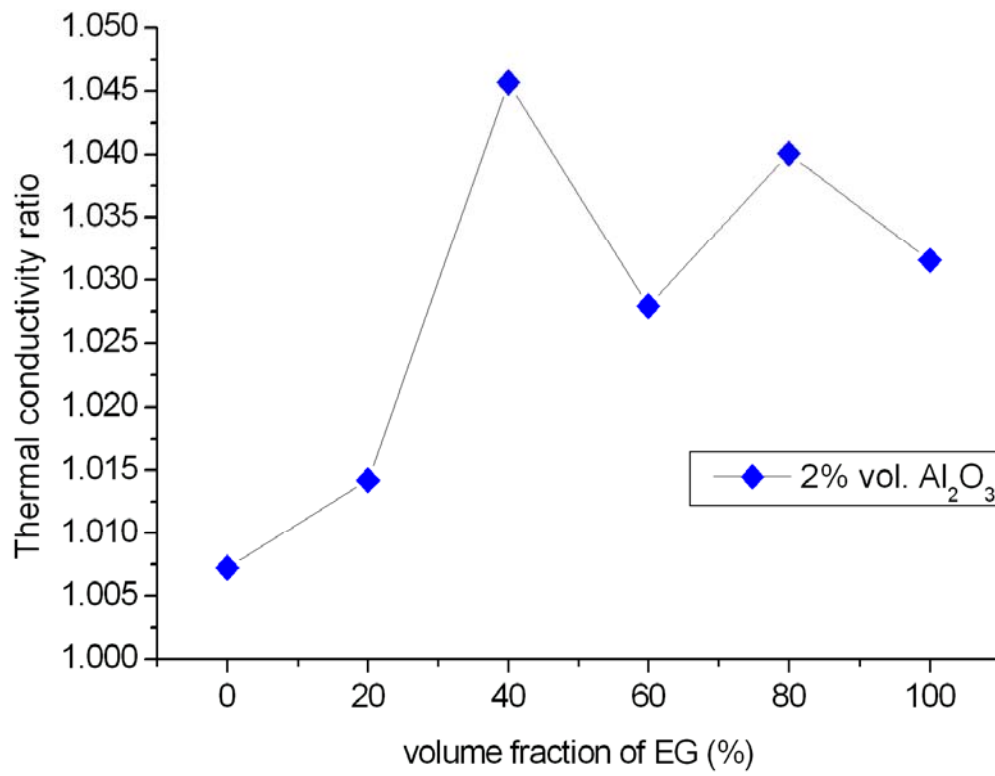
Figure 3.6 The thermal conductivity ratio of the water-EG based Al_2O_3 nanofluid versus

different viscosities
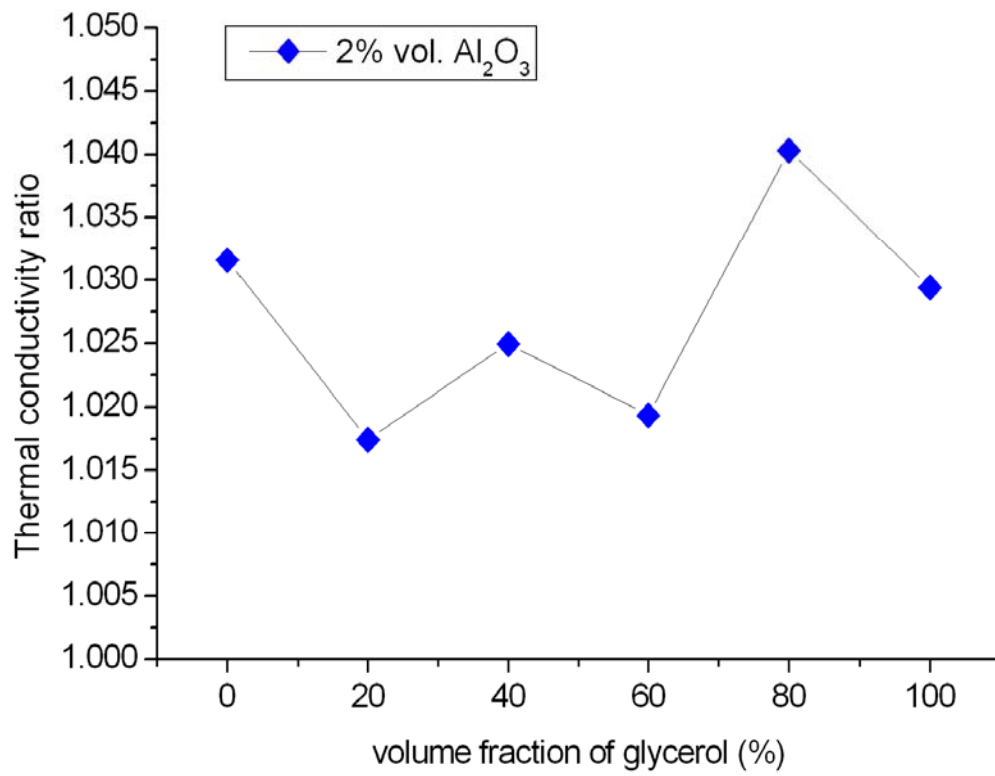
Figure 3.7 The thermal conductivity ratio of the EG-glycerol based Al$_2$O$_3$ nanofluid

versus different viscosities

Figure 3.8 The magnetic effects on the Fe$_3$O$_4$ nanofluid
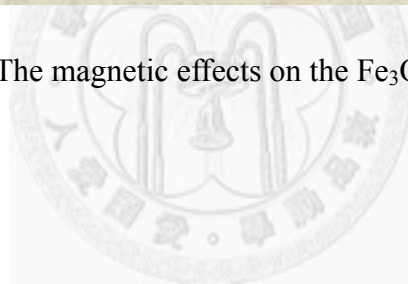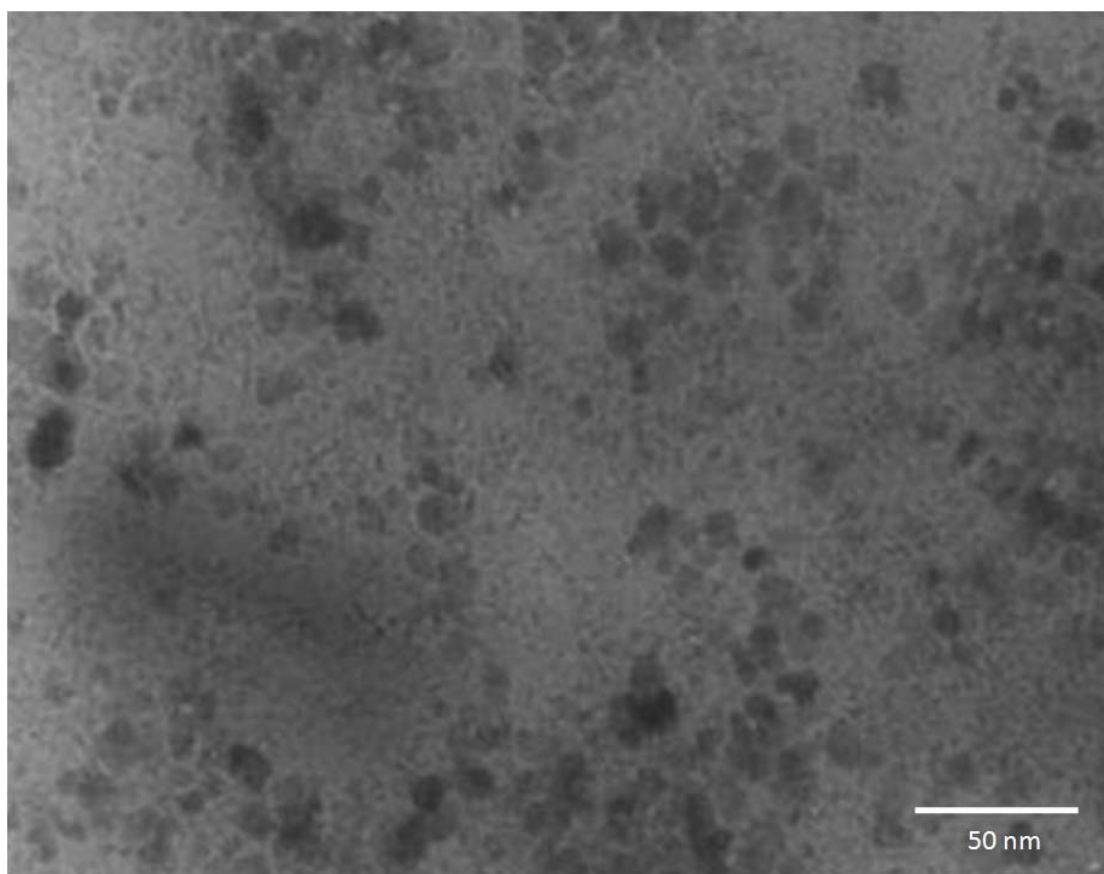
Figure 3.9 The TEM photo of Fe$_3$O$_4$ nanoparticles
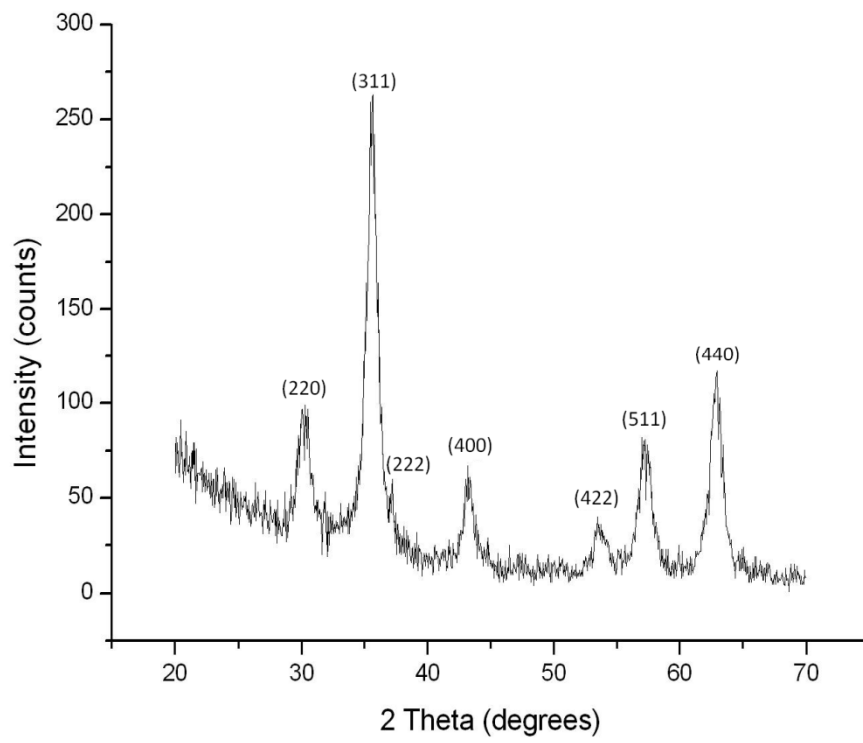
Figure 3.10 The crystalline phases of the Fe$_3$O$_4$ nanoparticles
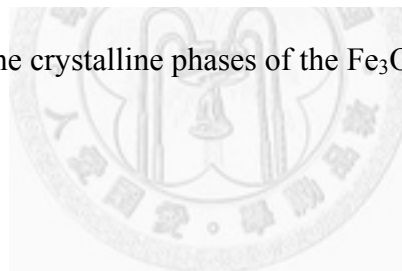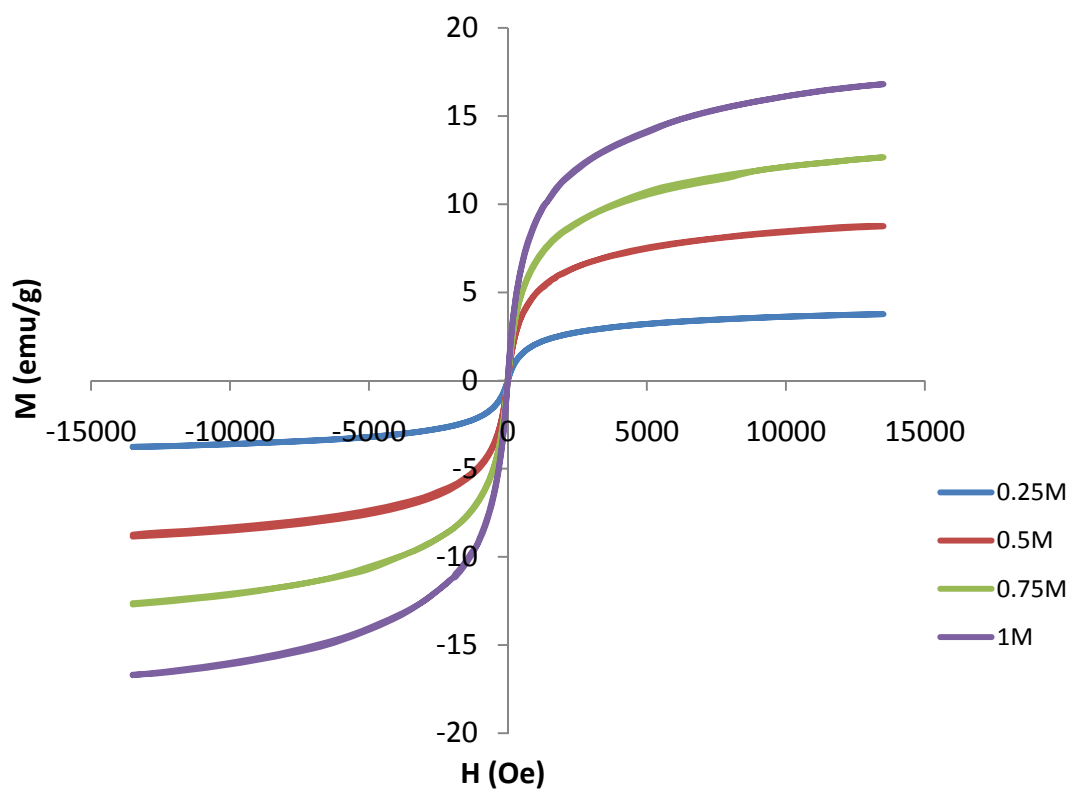
Figure 3.11 The magnetized curve of the Fe_3O_4 nanofluid measured by a VSM
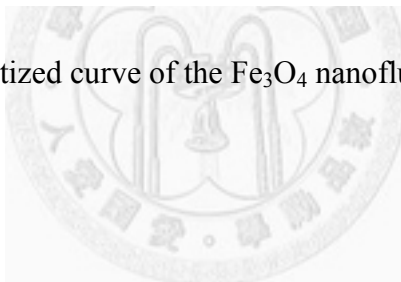
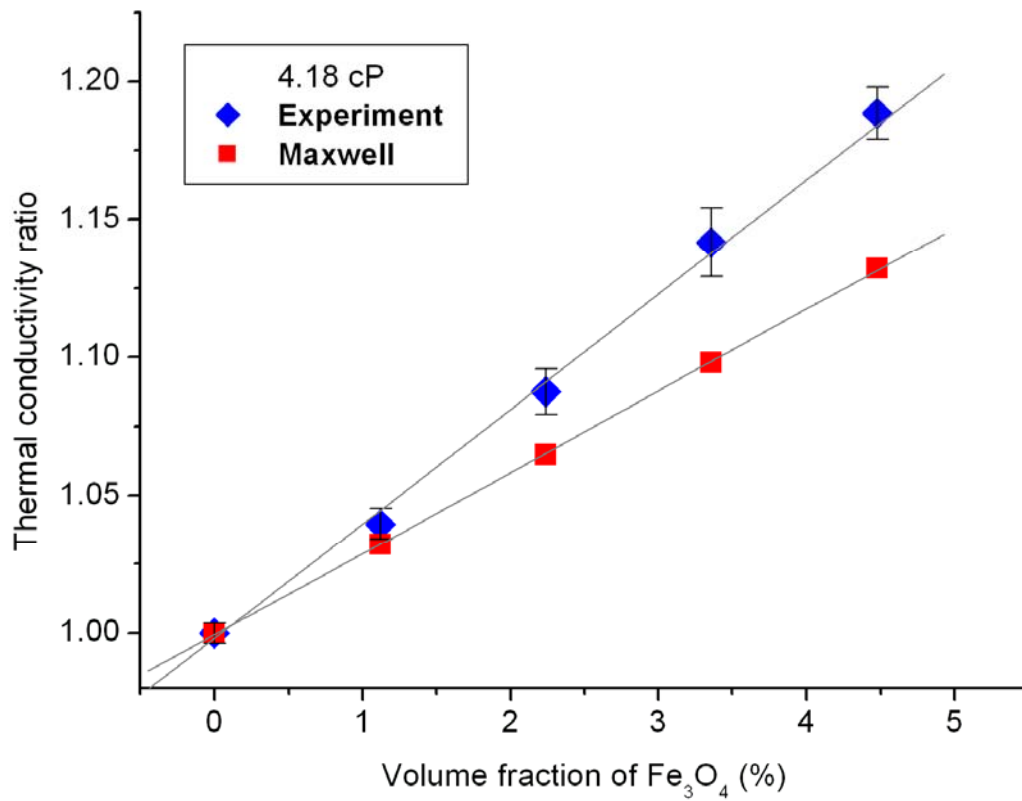Figure 3.12 The measured viscosities of the diesel oil-PDMS base fluids as a function of

volume fraction of PDMS at 25℃

Figure 3.13 The thermal conductivity ratios, k_{nano}/k_{bf} and $k_{Maxwell}/k_{bf}$ of viscous

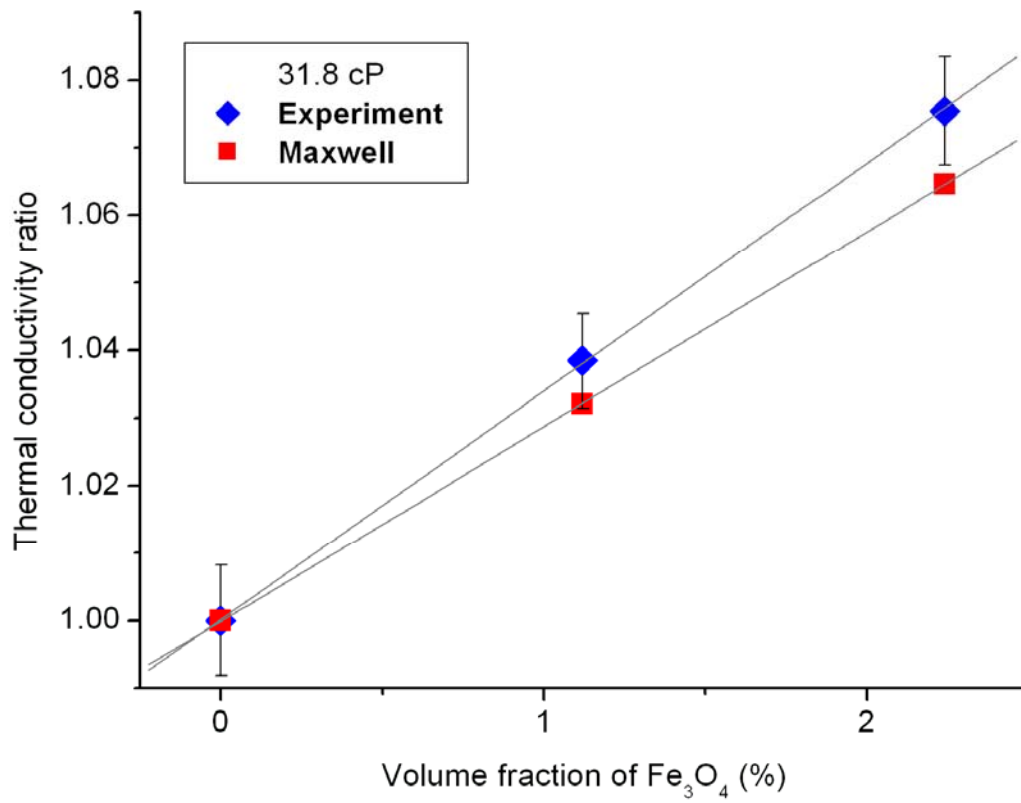nanofluids versus volume fraction of Fe_3O_4 nanoparticles at the viscosity of 4.18 cP

Figure 3.14 The thermal conductivity ratios, k_{nano}/k_{bf} and $k_{Maxwell}/k_{bf}$ of viscous

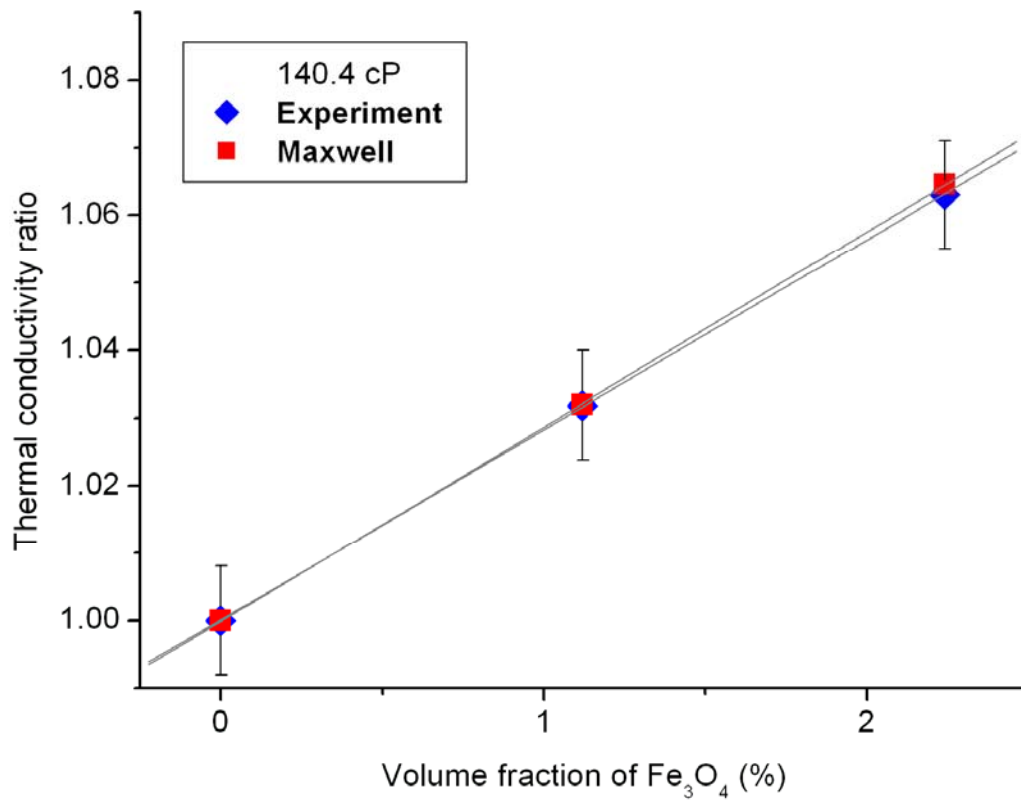nanofluids versus volume fraction of Fe_3O_4 nanoparticles at the viscosity of 31.8 cP

Figure 3.15 The thermal conductivity ratios, k_{nano}/k_{bf} and $k_{Maxwell}/k_{bf}$ of viscous

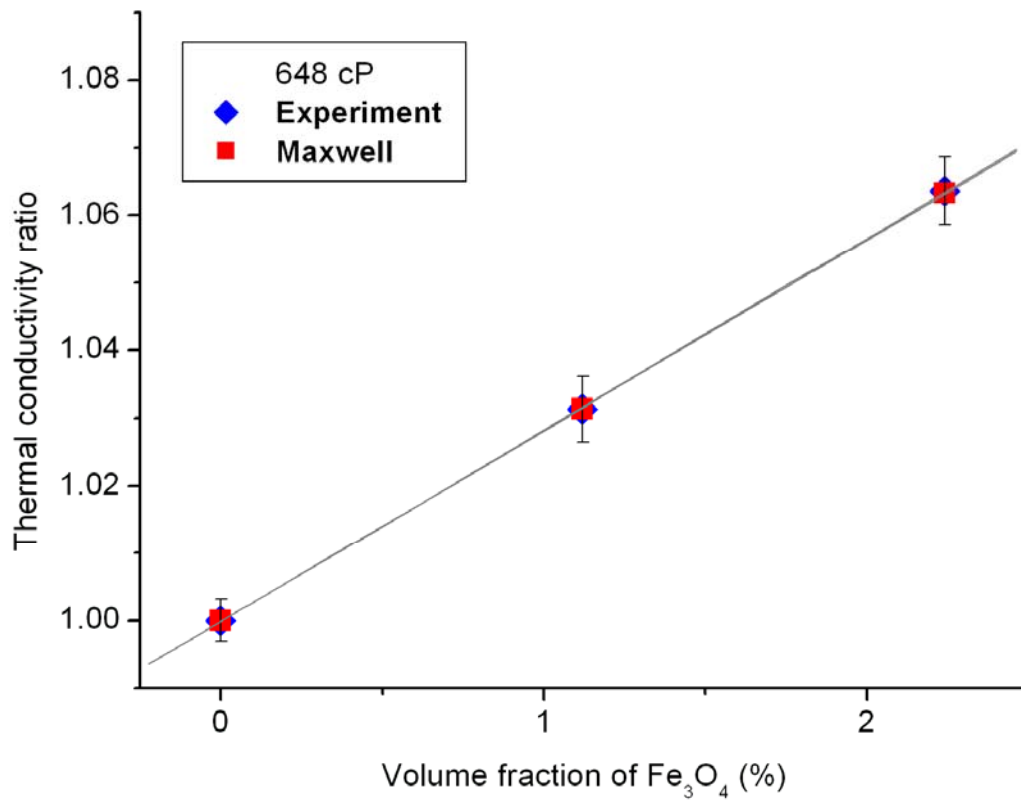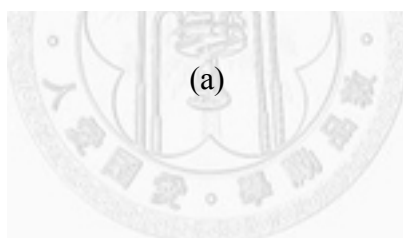nanofluids versus volume fraction of Fe_3O_4 nanoparticles at the viscosity of 140.4 cP
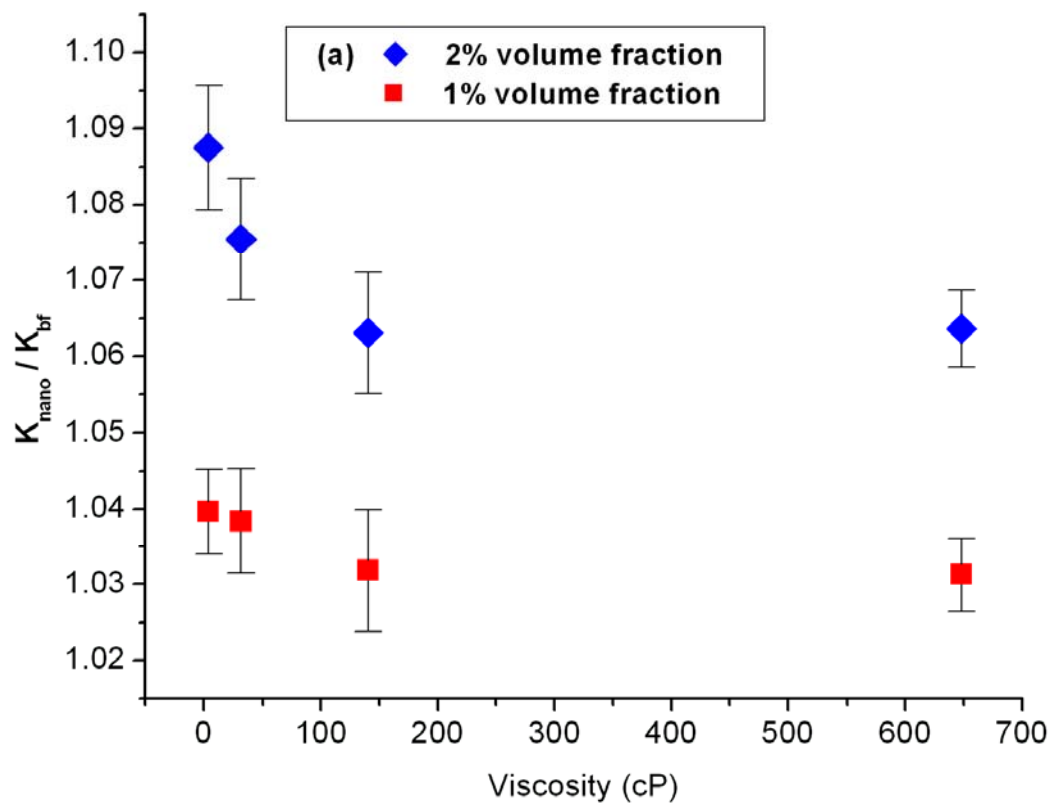
Figure 3.16 The thermal conductivity ratios, k_{nano}/k_{bf} and $k_{Maxwell}/k_{bf}$ of viscous

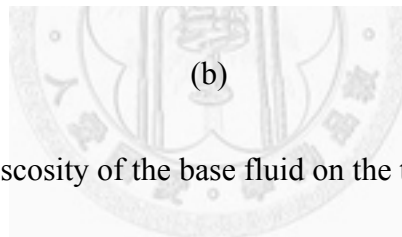nanofluids versus volume fraction of Fe_3O_4 nanoparticles at the viscosity of 648 cP

(a)

(b)
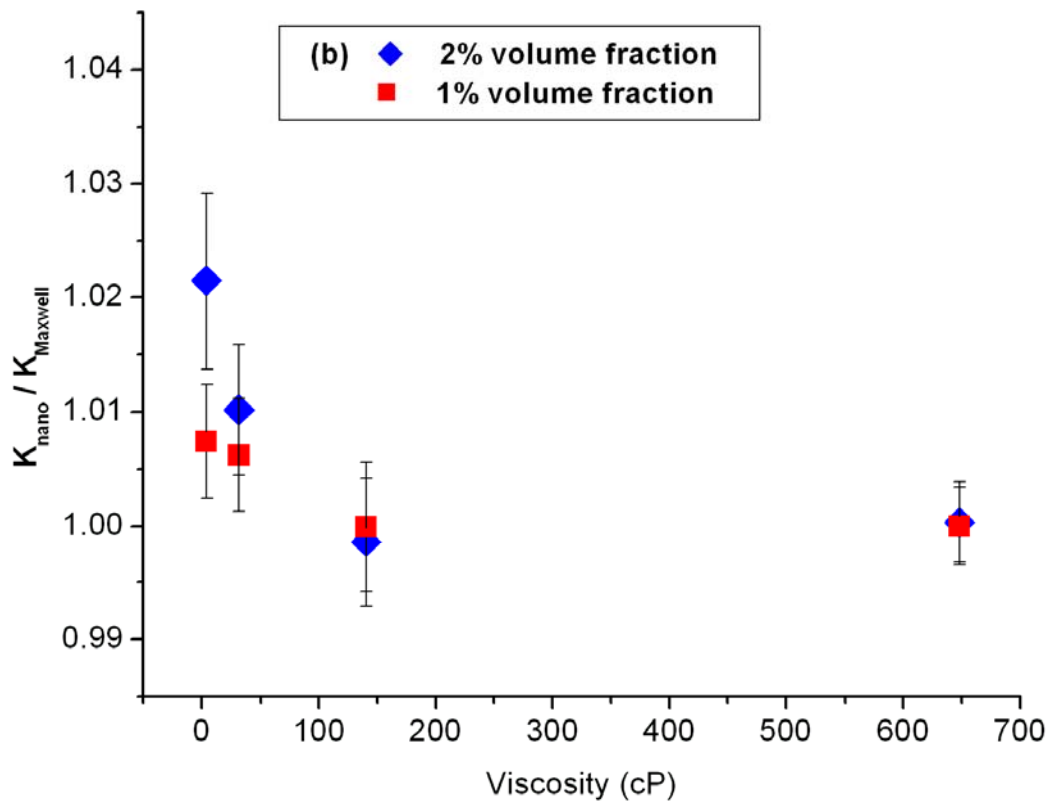
Figure 3.17 Effect of the viscosity of the base fluid on the thermal conductivity ratio of

nanofluids: (a) $k_{nanofluid}/k_{bf}$ and (b) $k_{nanofluid}/k_{Maxwell}$
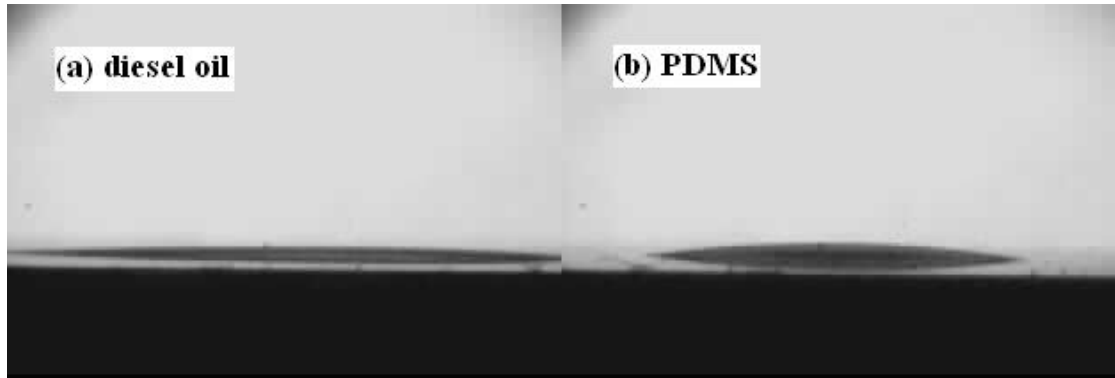
Figure 3.18 The contact angles between bulk Fe$_3$O$_4$ and components of viscous base

fluids: (a) diesel oil; (b) PDMS

Table 3.1 Physical properties of Al_2O_3 nanoparticles

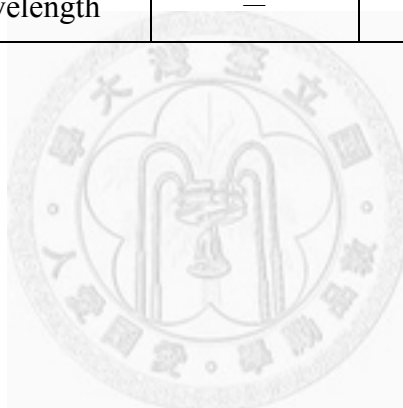| Properties	Unit	Typical value
Appearance	─	White powder
Al_2O_3 content	%	$\geqq 99.8$
Average diameter	nm	13
Specific surface area	m^2/g	$\geqq 100$
Apparent density	g/cm^3	0.05
Thermal conductivity	W/m·k	37~39
Refraction index	─	1.48~1.51
Emissivity and range of wavelength	─	0.915~0.920 at 5~20μm

Table 3.2 Physical properties of Fe_3O_4 nanofluids
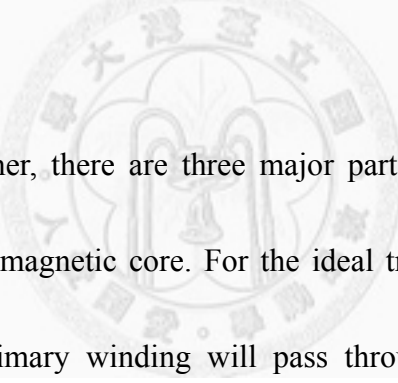
	Volume fraction (%)	Density (g/cm³)	$M_{saturation}$ (emu/g)	Initial relative permeability
Diesel oil	0	0.7381	0	1
0.25M	1.12	0.7709	3.85	1.055
0.5M	2.24	0.8203	8.85	1.120
0.75M	3.36	0.8612	12.7	1.188
1M	4.48	0.9313	16.7	1.251

Chapter 4 Application of Fe$_3$O$_4$ Nanofluids on Transformers

This chapter focuses on the performance of transformers which applies the ferrofluids as the magnetic core. One transformer is constructed on a capillary, and the other one is constructed on a wafer by the MEMS process. Firstly, the definitions of coupling coefficient and quality factor are described. Then, the inductance, resistance, coupling coefficient and quality factor of transformers are measured and simulated.

4.1 Definitions of Coupling Coefficient and Quality Factor

For a simple transformer, there are three major parts: the primary winding, the secondary winding and the magnetic core. For the ideal transformer, all the magnetic flux produced from the primary winding will pass through the secondary winding without any leakage. But actually, part of magnetic flux will not pass through the secondary winding. This is due to the imperfect coupling of windings, which results from the design of the windings and magnetic core. The leakage flux stores and discharges magnetic energy alternately, which acts effectively as inductors in series with the primary and secondary windings and causes the voltage drop. So the coupling coefficient is an important factor of transformer performance. In this study, according to the Japanese industrial standard (JIS) C6435, the coupling coefficient K is defined as

follow:

$$K = \sqrt{1 - \frac{L_{sc}}{L_{open}}} \qquad (4.1)$$

As Fig. 4.1 shown, the leakage inductance L_{sc} is measured from the one side while the

other side is closed, and the inductance L_{open} is measured form the one side while the

other side is open. The leakage inductances of the primary and secondary sides, L_{sc1} and

L_{sc2}, are respectively shown as follow:

$$L_{sc1} = (1 - K^2) \cdot L_{open1} \qquad (4.2)$$

$$L_{sc2} = (1 - K^2) \cdot L_{open2} \qquad (4.3)$$

The coupling coefficient K measured from primary and secondary side should be the

same. In order to avoid the error of measurement, the precise coupling coefficient

should be measured form the side with higher inductance. Besides, a simple transformer

is composed of two inductors. For an ideal inductor, there are no energy loss whiles the

current goes through the coil. However, real inductors include the resistance in series

and the capacitance in parallel with the inductance, as shown in Fig. 4.2. The series

resistance of inductor will consumes energy and causes energy loss. The criterion of

efficiency of inductors is the quality factor (Q) which is the ratio of inductive reactance

to resistance at a given frequency. The quality factor of an inductor is shown as follow:

$$Q = \frac{\omega L}{R} \qquad (4.4)$$

An inductor with high Q factor has performance approaching the behavior of an ideal

96

inductor.

4.2 Transformer on a Capillary

In this section, different magnetic cores, the air, bulk Fe_3O_4 and Fe_3O_4 nanofluids

of 0.25M, 0.5M, 0.75M and 1M, are applied as the magnetic core of transformers. The

self-inductance L_{open}, leakage inductance L_{sc}, coupling coefficient K, resistance and

quality factor Q are measured and calculated at the frequency ranging from 100 kHz to

100 MHz.

Fig. 4.3 shows the self-inductances of coils of transformers with different magnetic

cores. It illustrated that the overall inductances increase with the increase of Fe_3O_4

concentration. At the frequency ranging from 100 kHz to 15 MHz, the inductances

decrease rapidly due to the skin effect of coils. The inductance formula of a solenoid is

shown as follow:

$$L = \frac{\mu^* N^2 A}{l} \tag{4.5}$$

where μ^* is the permeability, N is the number of coil turns, A is the cross-section area,

and l is the length of solenoid. When the frequency increases, the current gathers at the

skin of coils, which decreases the effective cross-section area A of solenoid and results

in the decrease of inductance. At the frequency ranging from 15 MHz to 100 MHz, the

inductances increase gradually and approach the maximum inductance at the resonance frequency. Over the resonance frequency, the inductor will drop sharply and transfer the inductive to the capacitive. Although the inductances with the core of air, Fe_3O_4 nanofluids of 0.25M, 0.5M, 0.75M and 1M increase linearly with the increase of Fe_3O_4 concentration, the inductance with the core of bulk Fe_3O_4 does not increase by several times as we expect. One of the reasons to explain this phenomenon is that a lot of cavities are formed in the bulk Fe_3O_4 during the fabricating process, and the density of bulk Fe_3O_4 is not as high as it is expected. The measured density of bulk Fe_3O_4 is 0.34472 g/cm^3 which is much smaller than that of magnetite, and the bulk Fe_3O_4 has high porosity up to 0.9337. Fig. 4.4 shows the leakage inductances of coils of transformers with different magnetic cores. Similar with the self-inductance of coils, the leakage inductance decreases at lower frequency due to the skin effect and increases at higher frequency due to the resonance. Fig 4.5 shows the coupling coefficient of transformers with different magnetic cores. The coupling coefficient increases with the increase of Fe_3O_4 concentration. The coupling coefficient increases rapidly below the frequency of 5 MHz and increases gently over the frequency of 5 MHz.

The experimental results mentioned above shows improvements on the inductance and coupling coefficient of transformers. However, as shown in Fig. 4.6, the resistance of each pattern increases as a function of frequency, and also increases with the increase

of Fe_3O_4 concentration. At the frequency of 100 MHz, the resistance with the magnetic core of 0.25 M and 1 M Fe_3O_4 nanofluids is respectively two and five times to the resistance with the air core. It is because that when the magnetic core is magnetized alternately, the magnetization of material always lags behind the external magnetic field. At the low frequency, the external magnetic field and the magnetization of material can be regarded as proportional to each other through the scalar permeability. But at the high frequency, they will react to each other with some lag so that the permeability can be expressed as a complex number:

$$\mu^* = \mu' - j\mu''$$ (4.6)

The real part of complex permeability, μ', which has the same phase with the magnetic field, presents the stored energy coefficient when the material is magnetized. And the imaginary part of complex permeability, μ'', which has the phase of 90 degree delay comparing to the magnetic field, presents the consumed energy coefficient when the material is magnetized. The impedance of a real inductor is expressed as follow:

$$Z = R + j\omega L$$ (4.7)

Substituting (4.5) and (4.6) into (4.7) and rearranging, the real part of impedance is related to the frequency:

$$Z = R + \omega\frac{\mu'' N^2 A}{l} + j\omega\frac{\mu' N^2 A}{l}$$ (4.8)

The imaginary part of complex permeability will reflect dramatically on the resistance

when the frequency increases. Moreover, the resistance with bulk Fe_3O_4 shows an exceptional value. The resistance with bulk Fe_3O_4 is lower than that with 1M Fe_3O_4 nanofluid below the frequency of 100 MHz. But it can be observed that the slope of curve of bulk Fe_3O_4 increases faster than that of 1M Fe_3O_4 nanofluid, and it is speculated that the imaginary part of frequency-dependent complex permeability of bulk Fe_3O_4 will be larger than that of 1M Fe_3O_4 nanofluid at higher frequency.

Fig. 4.7 shows the quality factor of coils of transformers with different magnetic cores. Because the increase of resistance is larger and faster than the increase of inductance with the present of Fe_3O_4 nanofluids, the quality factor decreases with the increase of Fe_3O_4 concentration. With the present of bulk Fe_3O_4, the quality factor still lower than that with the air core at high frequency. However, below the frequency of 4 MHz, the quality factor with the magnetic core of bulk Fe_3O_4 is higher than that with the air core as shown in Fig. 4.8.

4.3 MEMS Transformer on a Chip

In this section, two magnetic cores, the air core and the magnetic core of 1 M Fe_3O_4 nanofluid are applied on a MEMS transformer. The self-inductance L_{open}, leakage inductance L_{sc}, coupling coefficient K, resistance and quality factor Q are measured and

calculated under the frequency ranging from 100 kHz to 100 MHz.

Fig. 4.9 shows the self-inductances and leakage inductances of coils of MEMS transformers with the air core and magnetic core of 1 M Fe_3O_4 nanofluid. It illustrated that the self-inductances and leakage inductances increase with the present of 1M Fe_3O_4 ferrofluid. At the frequency ranging from 100 kHz to 20 MHz, the inductances slightly decrease due to the skin effect. Over the frequency of 20 MHz, the inductances increase gradually and approach the maximum inductance at the resonance frequency. Fig. 4.10 shows the coupling coefficient of MEMS transformers with the air core and magnetic core of 1 M Fe_3O_4 nanofluid. The coupling coefficient increases slightly with the present of 1M Fe_3O_4 nanofluid.

Fig. 4.11 and Fig. 4.12 show the resistance and quality factor of coils of MEMS transformer with the air core and magnetic core of 1 M Fe_3O_4 nanofluid, respectively. The resistance with 1M Fe_3O_4 nanofluid is higher than that with the air core due to the imaginary part of complex permeability, which results in the lower quality factor with 1M Fe_3O_4 nanofluid.

4.4 HFSS Simulation

In this section, the performance of transformer on a capillary and MEMS transformer on a chip is simulated by Ansoft HFSS. To generate an electromagnetic field solution,

HFSS employs the finite element method. In general, the finite element method divides the full problem space into thousands of smaller regions and represents the field in each element with a local function. In HFSS, the geometric model is automatically divided into a large number of tetrahedra, where a single tetrahedron is a four-sided pyramid. This collection of tetrahedra is referred to as the finite element mesh. The governing equations, Maxwell's equations, are shown as follow:

$$\nabla \times E = -\frac{\partial B}{\partial t} \tag{4.9}$$

$$\nabla \times H = J + \frac{\partial D}{\partial t} \tag{4.10}$$

$$\nabla \cdot D = \rho \tag{4.11}$$

$$\nabla \cdot B = 0 \tag{4.12}$$

where E is the electric field, B is the magnetic field , H is the magnetizing field, J is the free current density, D is the electric displacement field, and ρ is the free charge density.

To calculate the S-matrix associated with a structure with ports, HFSS does the following: [86]

1. The structure is divided into a finite element mesh

2. The modes is computed on each port of the structure that are supported by a transmission line having the same cross-section as the port

3. The full electromagnetic field pattern is computed inside the structure, assuming that one mode is excited at a time

4. The generalized S-matrix is computed from the amount of reflection and transmission that occurs

The resulting S-matrix allows the magnitude of transmitted and reflected signals to be computed directly from a given set of input signals, reducing the full 3D electromagnetic behavior of a structure to a set of high frequency circuit parameters.

4.4.1 Simulation of Transformer on a Capillary

For the case of transformer on a capillary, some assumptions are adopted to simplify the complex model and reduce the calculating time. Firstly, on the geometry, the circular cross-sections of the wires and capillary are simplified as a hexagon and a dodecagon, respectively, to reduce the number of elements. On the material property, the relative permittivity, relative permeability and magnetic loss tangent are assumed as frequency-independent constants.

Fig. 4.13 shows the model of transformer on a capillary which consists of two coils, the glass tube and the core. Before discussing the result of simulation, the convergence of simulation is verified. The default criterion used by HFSS to determine the convergence of solution is the maximum magnitude delta S which means the maximum difference of S-Matrix magnitude between two consecutive passes. Fig. 4.14 shows the convergence curve of simulation with the model of transformer on a capillary. The

maximum magnitude delta S decreases when the number of tetrahedra increases, which indicates that the simulation has a converged solution. When the number of tetrahedra reaches 205395, the maximum magnitude delta S is 0.010308, which is a half of 0.02 of the default value. And when the number of tetrahedral reaches 255112, the maximum magnitude delta S is 0.00185, which is a tenth of the default value. Considering the solving efficiency, the model is meshed into about 220000 tetrahedra.

Fig. 4.15 shows the simulated self-inductance of coils of transformers with different magnetic cores, which shows the same tendency in Fig. 4.3. The simulated self-inductance increases linearly with the increase of permeability, and also shows the decrease due to the skin effect and the increase due to the resonance. Fig. 4.16 and Fig. 4.17 show the simulated leakage inductance and coupling coefficient with different magnetic cores. These simulation results are quite agree with the measured results in Fig 4.3, Fig. 4.4 and Fig. 4.5.

Fig. 4.18 shows the simulated resistance of coils of transformers with different magnetic cores. Because of the lag between the magnetization of material and the external magnetic field, the magnetic tangent loss, $\tan\delta$, should be considered:

$$\tan\delta = \frac{\mu''}{\mu'} \tag{4.13}$$

The researches of Hrianca et al. [87] and Sutariya et al. [88] are referred to estimate the values of $\tan\delta$ used in this study. Fig. 4.19 shows the simulated quality factor of coils of

transformers with different magnetic cores. And the quality factor decreases due to the dramatic increase of resistance as the same as the results in Fig. 4.7.

4.4.2 Simulation of MEMS Transformer on a Chip

For the case of MEMS transformer, some assumptions are also adopted to simplify the complex model and reduce the calculating time. On the geometry, the circular cross-section of connecting wires is simplified as a hexagon to reduce the number of elements. On the material property, the relative permittivity, relative permeability and magnetic loss tangent are also assumed as frequency-independent constants.

Fig. 4.20 and Fig. 4.21 show the models of MEMS transformer and the dummy PCB. The convergence curve of simulation with the model of MEMS transformer is shown in Fig. 4.22. The maximum magnitude delta S decreases when the number of tetrahedra increases, which indicates that the simulation has a converged solution. When the number of tetrahedra reaches 39606, the maximum magnitude delta S is 0.0086597, which is less than a half of default value. And when the number of tetrahedral reaches 74443, the maximum magnitude delta S is 0.0021021, which is a tenth of the default value. Considering the solving efficiency, the model is meshed into about 40000 tetrahedra.

Fig. 4.23 shows the simulated self-inductance and leakage inductance of coils of

MEMS transformer with the air core and magnetic core of 1 M Fe_3O_4 nanofluid.

Comparing to the measured results, the simulated results shows that the parasitical

capacitance is underestimated so that a higher resonance frequency is obtained, and the

simulated inductances at the frequency of 100MHz are lower than the measured. Fig.

4.24 shows the simulated coupling coefficient of MEMS transformer with the air core

and magnetic core of 1 M Fe_3O_4 nanofluid. With the present of magnetic core of 1 M

Fe_3O_4 nanofluid, the coupling coefficient increases slightly but still poor.

Fig. 4.25 and Fig. 4.26 show the simulated resistance and quality factor of coils of

MEMS transformer with the air core and magnetic core of 1 M Fe_3O_4 nanofluid. The

measured resistance is higher than the simulated, and it is speculated that the high

resistance results from the bad contact between bonding wires and copper pads. Due to

the lag between the magnetization of material and the external magnetic field, with the

present of magnetic core of 1 M Fe_3O_4 nanofluid, the resistance increases and the

quality factor decreases.

4.5 Discussions

As shown in Fig. 2.10, it illustrates the characteristic of super-paramagnetism of

Fe_3O_4 nanofluid. Thus, the Fe_3O_4 nanofluid is applied as the magnetic core to reduce the

hysteresis loss in this study. However, due to the lag between the magnetization of

material and the external magnetic field, the resistance increases as a function of frequency, which results in a low quality factor. The reasons of lag are speculated as follow:

1. On the macroscopic view, a nanoparticle can be regard as a small magnetic dipole as shown in Fig. 4.27(a). While the external magnetic field is applied, the directions of the magnetic dipoles will turn to the direction of external magnetic field and produce a non-zero total magnetic dipole moment as shown in Fig. 4.27(b). Once the external magnetic field is removed, the directions of the magnetic dipoles will turn to random directions due to the Brownian motion, and the total magnetic dipole moment will reduce to zero in a short time.

2. On the microscopic view, a nanoparticle is composed of numerous magnetic dipoles as shown in Fig. 4.28(a). These magnetic dipoles are also influenced while the external magnetic field is applied as shown in Fig. 4.28(b). Once the external magnetic field is removed, the directions of the magnetic dipoles will turn to random directions, and the total magnetic dipole moment will reduce to zero in a short time.

Therefore, when the frequency of alternate external magnetic field is high enough, which means that the alternate time of magnetic field is smaller than the relaxation time, the lag will occur and cause the increase of resistance.

For the reasons mentioned above, the lag results in the increase of resistance. And the resistance increases faster and larger than that of inductance. Finally, the quality factor decreases with the present of Fe_3O_4 at high frequency.
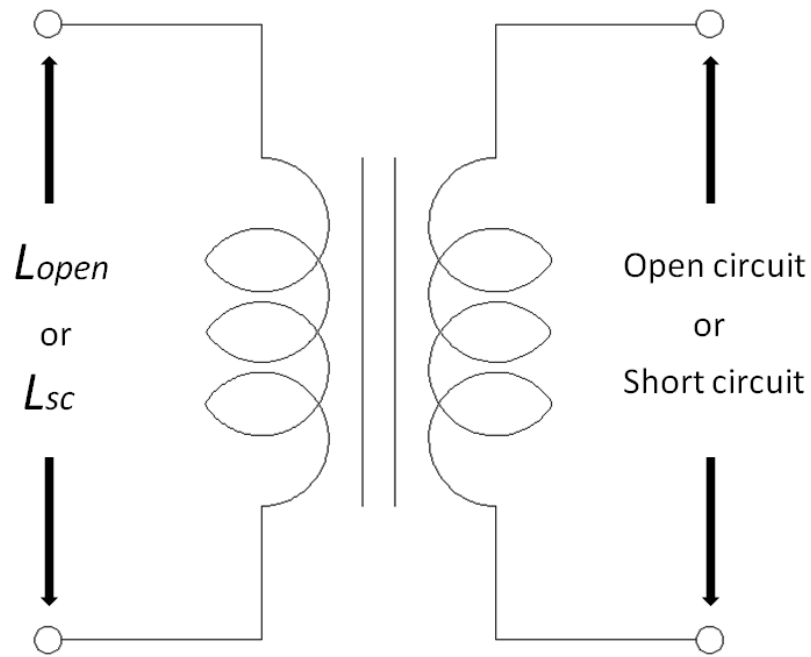
Fig. 4.1 The schematic measurement of self inductance and leakage inductance
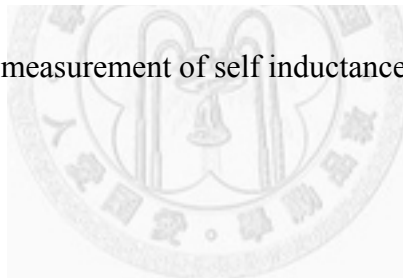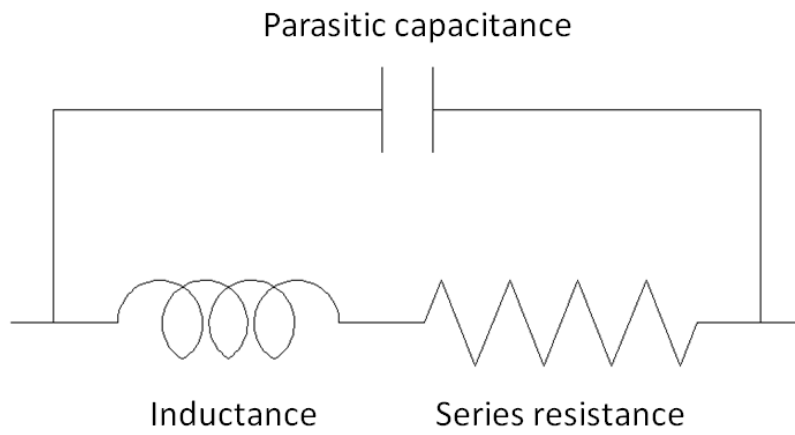
Fig. 4.2 The effective circuit model of real inductors containing the series resistance and

parasitic capacitance
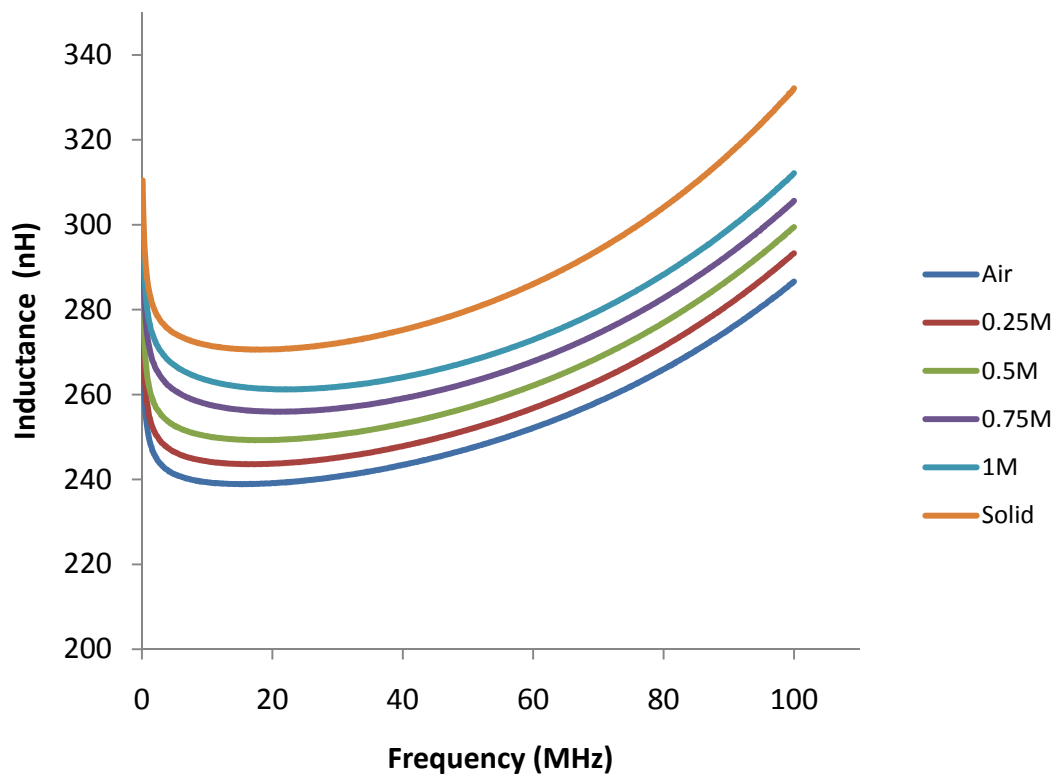
Fig. 4.3 The self-inductance of coils of transformers with different magnetic cores
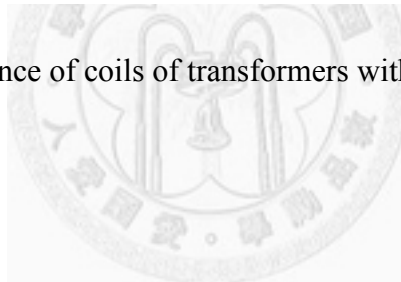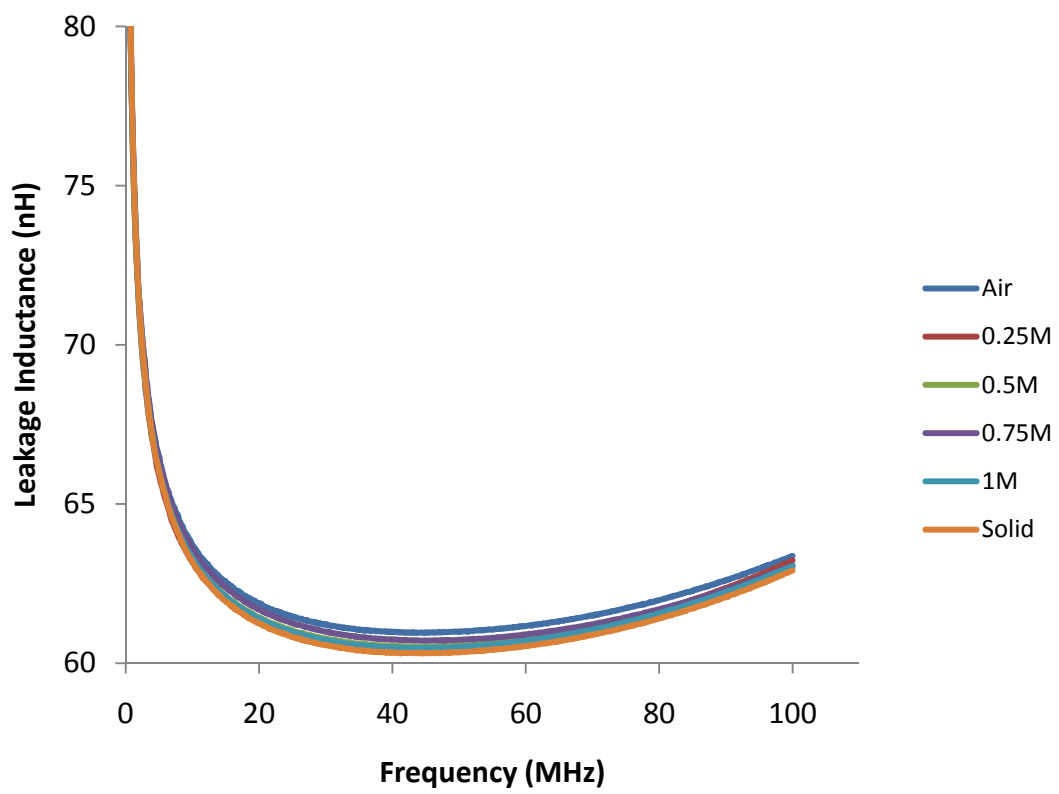
Fig. 4.4 The leakage inductance of coils of transformers with different magnetic cores
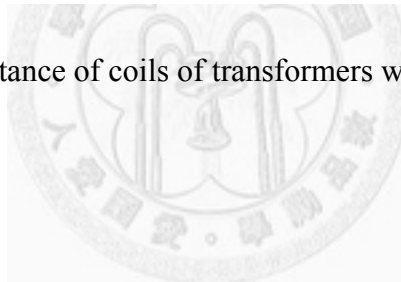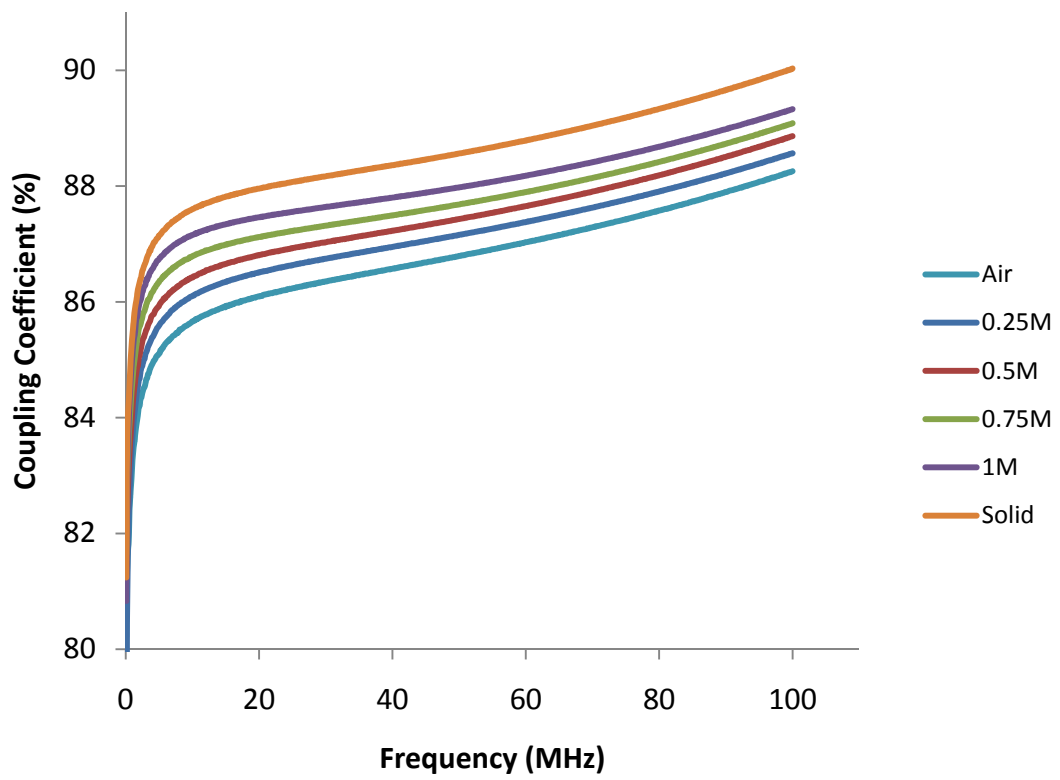
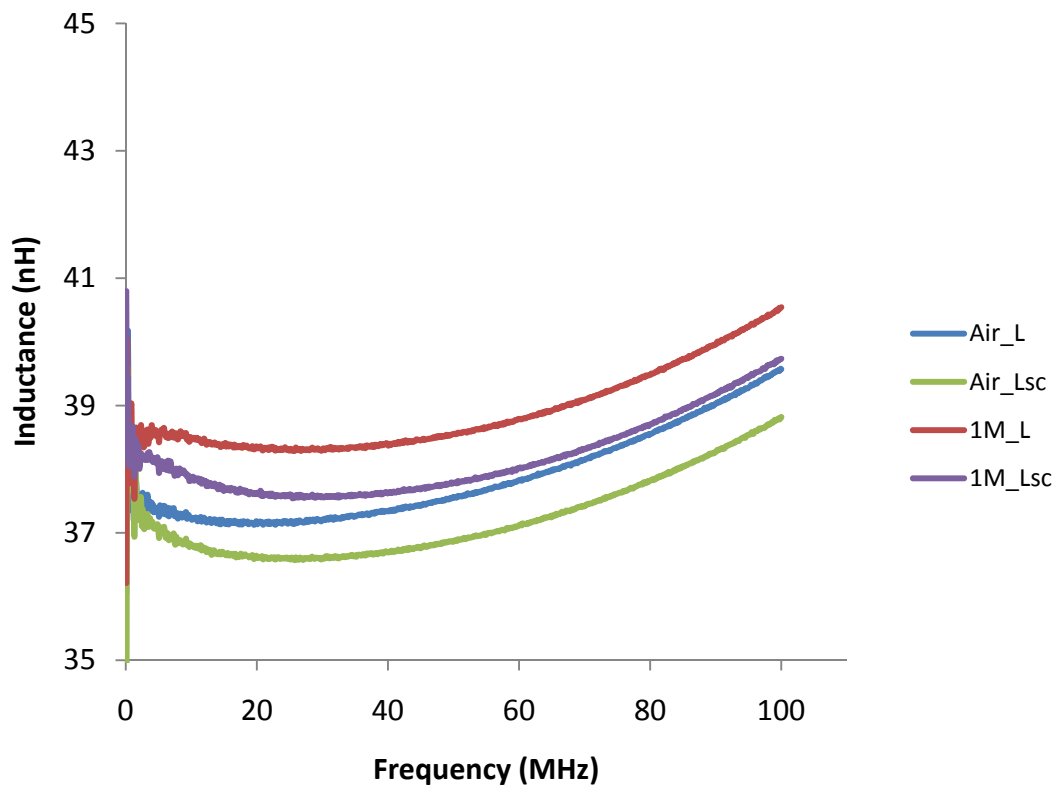Fig. 4.5 The coupling coefficient of transformers with different magnetic cores
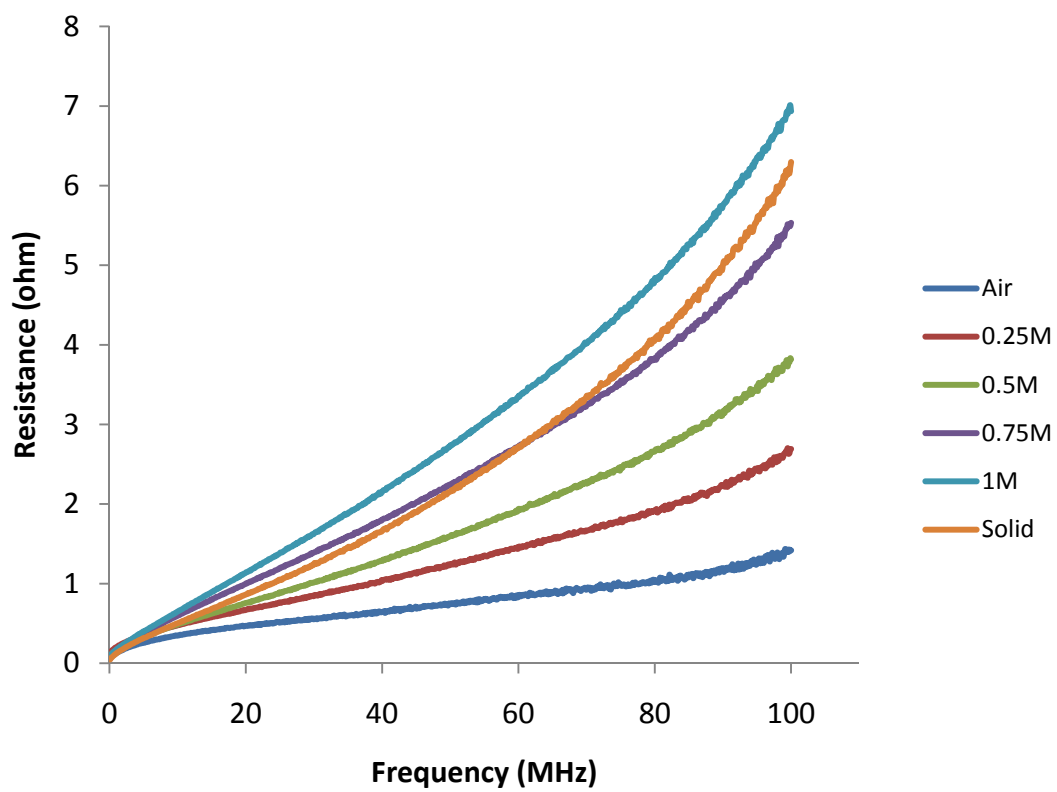
Fig. 4.6 The resistance of coils of transformers with different magnetic cores
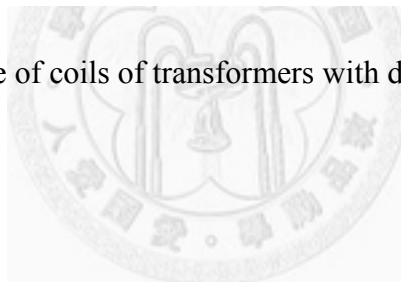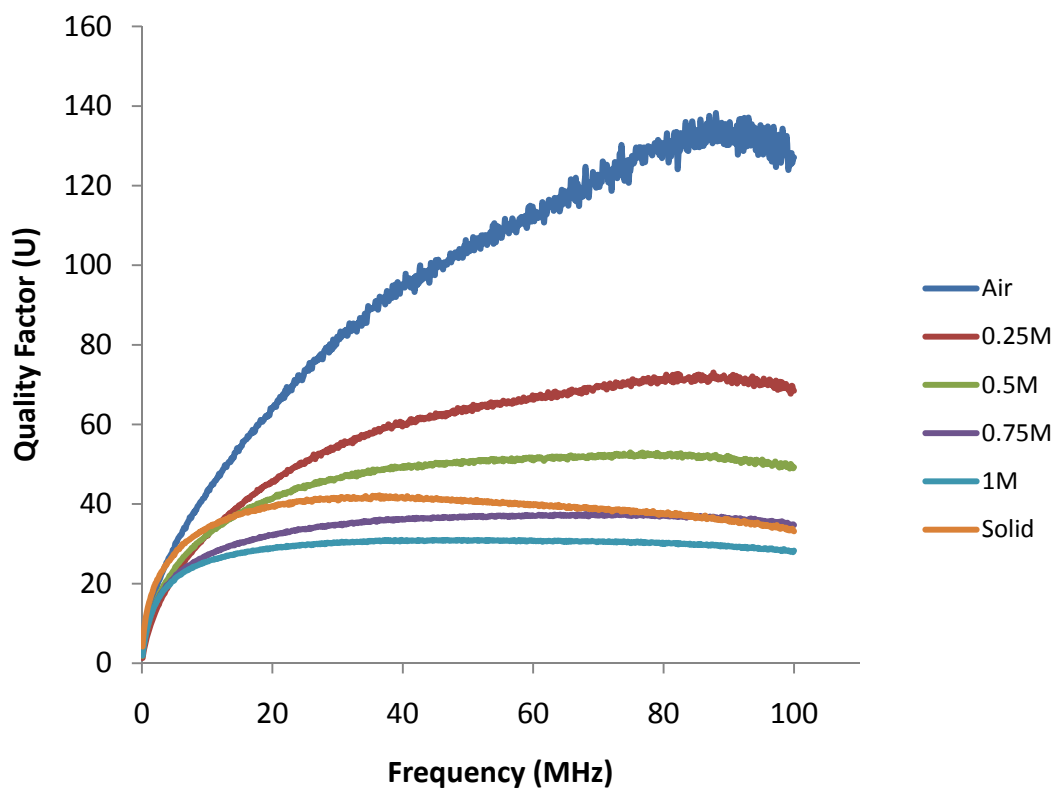
Fig. 4.7 The quality factor of coils of transformers with different magnetic cores
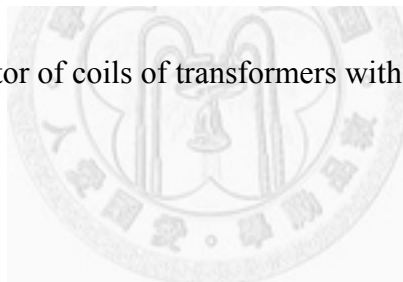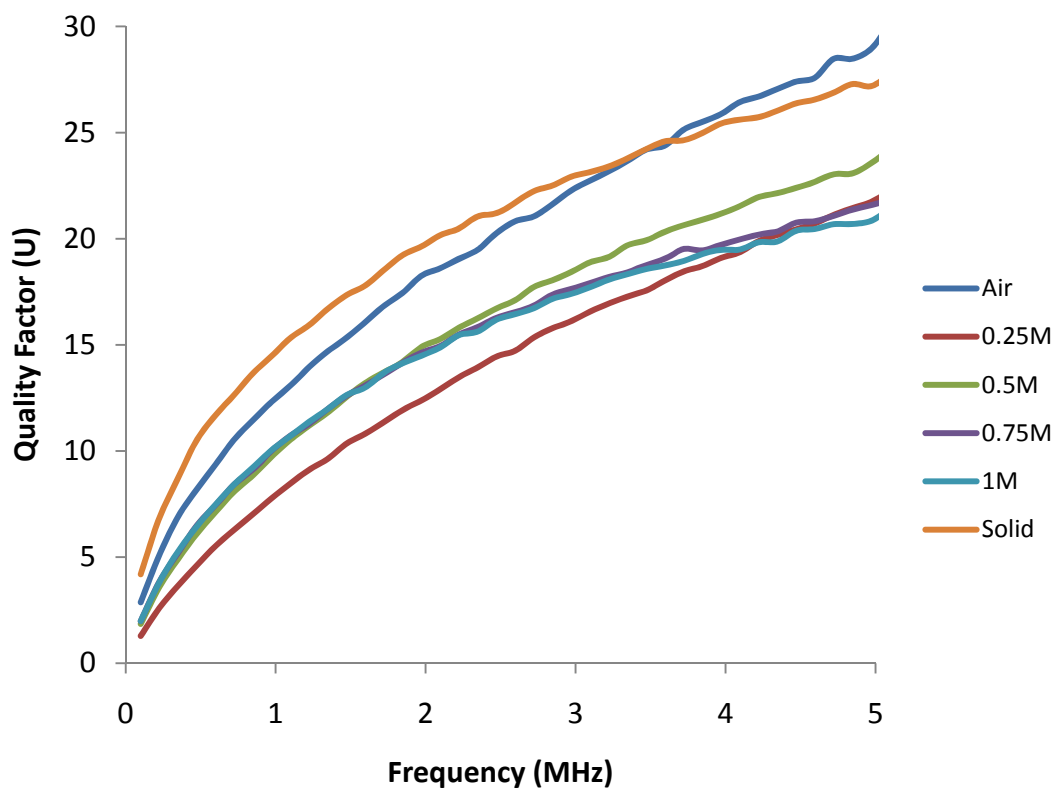
Fig. 4.8 The quality factor of coils of transformers with different magnetic cores at low

frequency
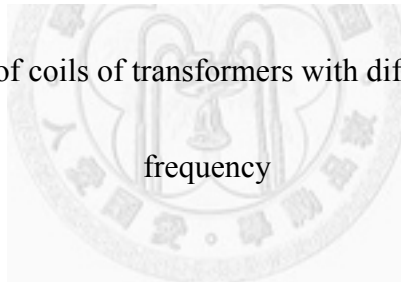
Fig. 4.9 The self-inductances and leakage inductances of coils of MEMS transformer

with the air core and magnetic core of 1 M Fe_3O_4 nanofluid
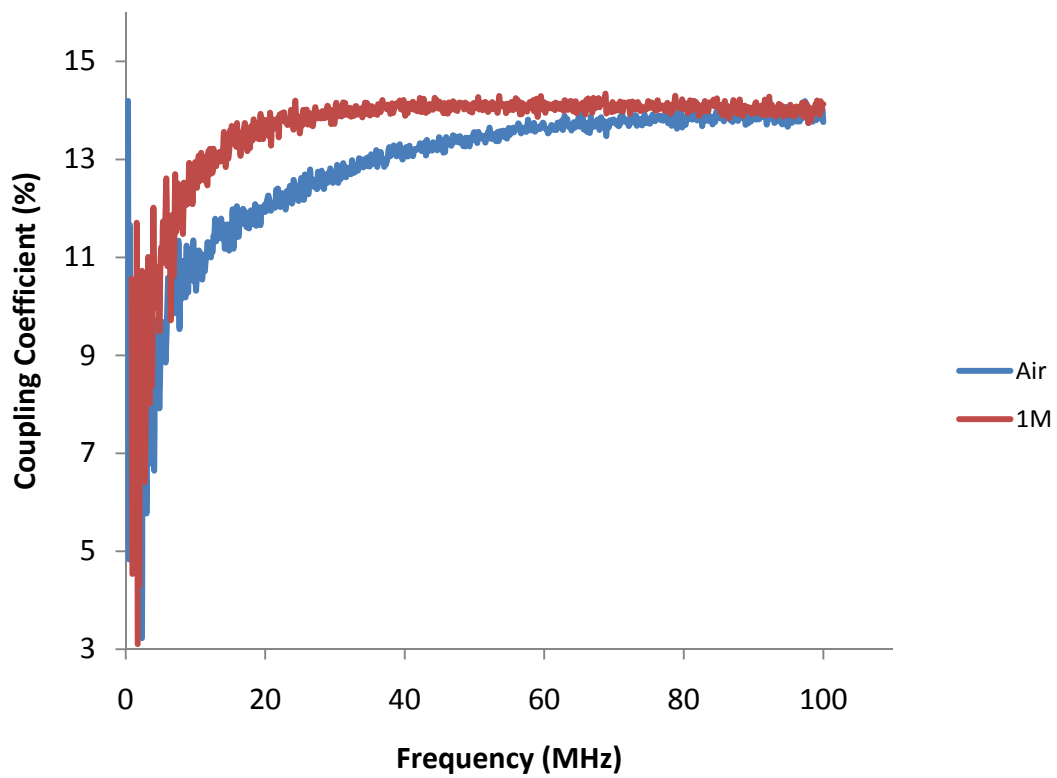
Fig. 4.10 The coupling coefficient of MEMS transformers with the air core and
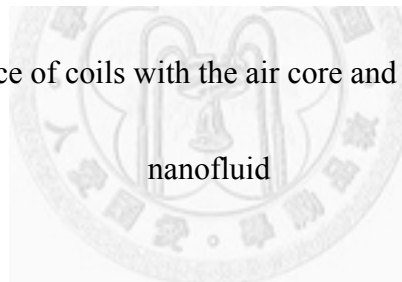
magnetic core of 1 M Fe_3O_4 nanofluid
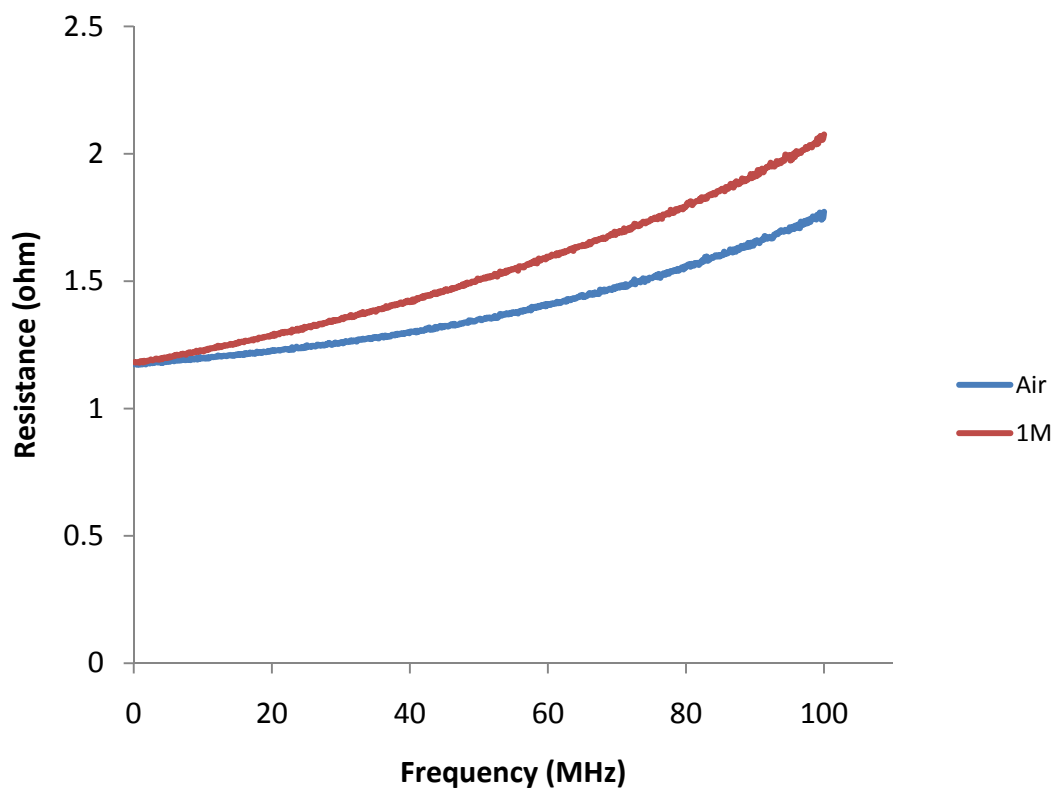
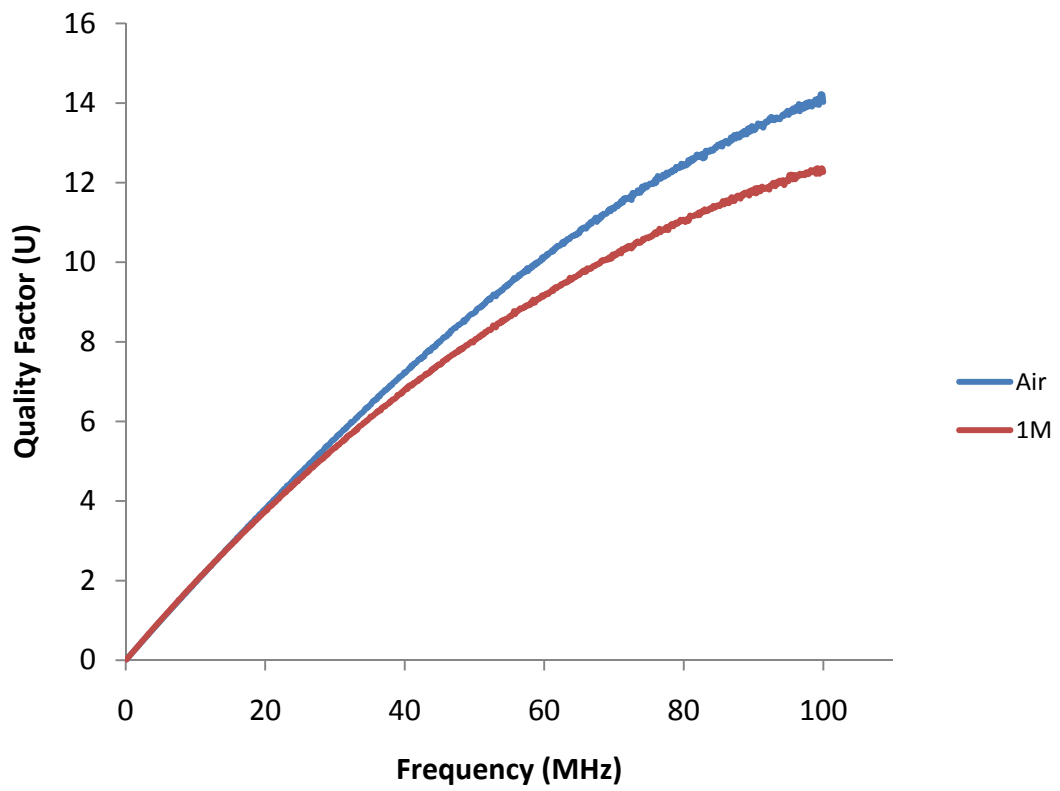Fig. 4.11 The resistance of coils with the air core and magnetic core of 1 M Fe_3O_4
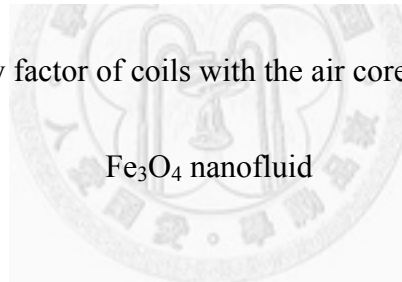
nanofluid

Fig. 4.12 The quality factor of coils with the air core and magnetic core of 1 M
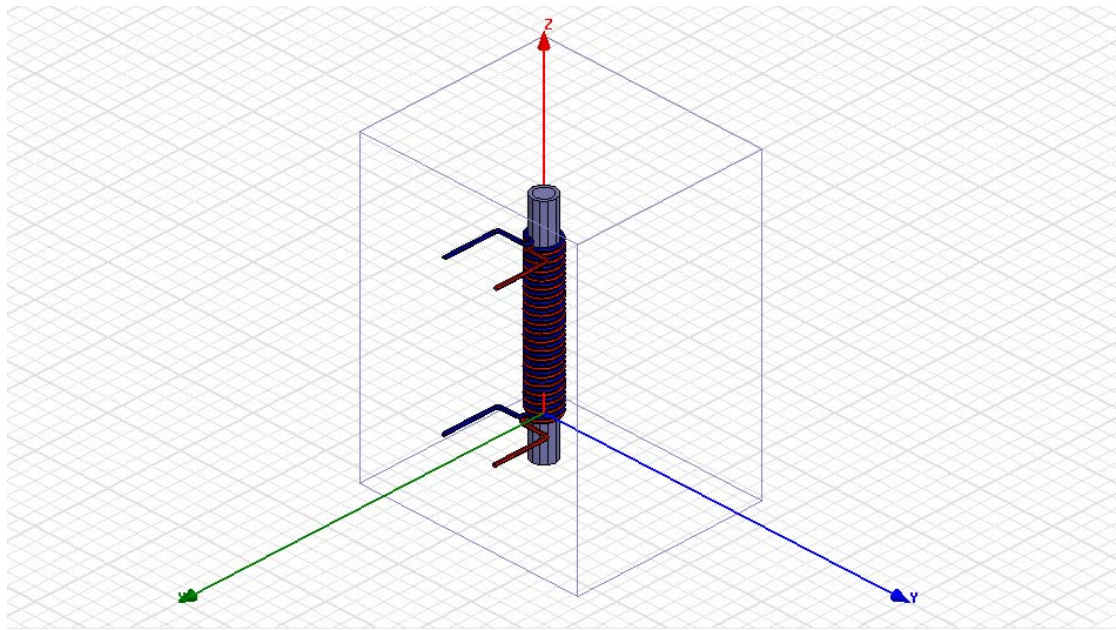
Fe_3O_4 nanofluid

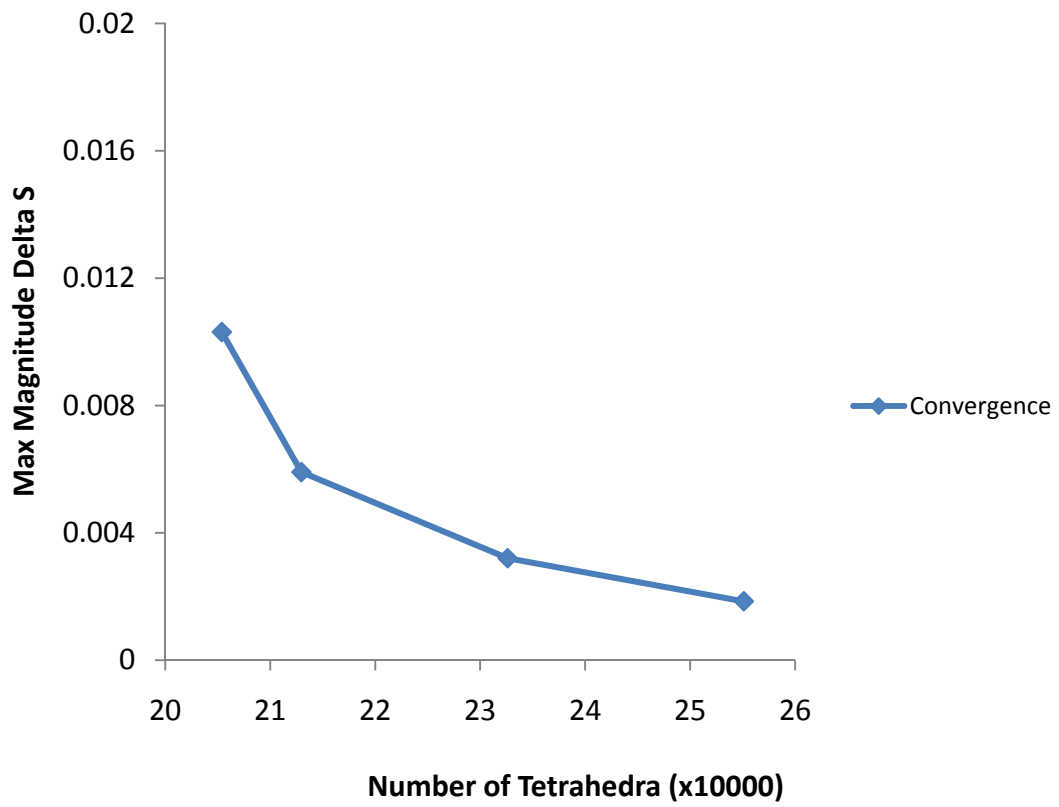Fig. 4.13 The HFSS model of transformer on a capillary

Fig. 4.14 The convergence curve of simulation with the model of transformer on a
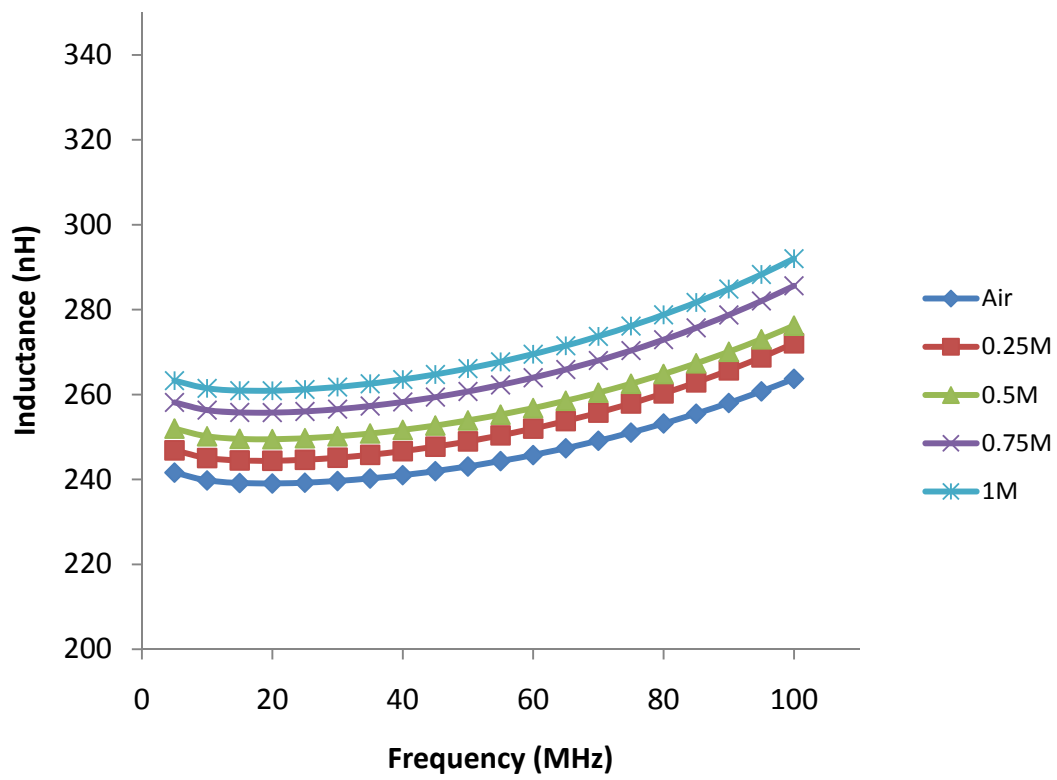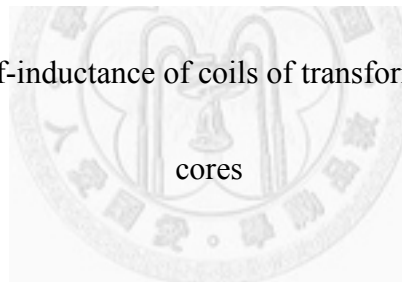
capillary

Fig. 4.15 The simulated self-inductance of coils of transformers with different magnetic
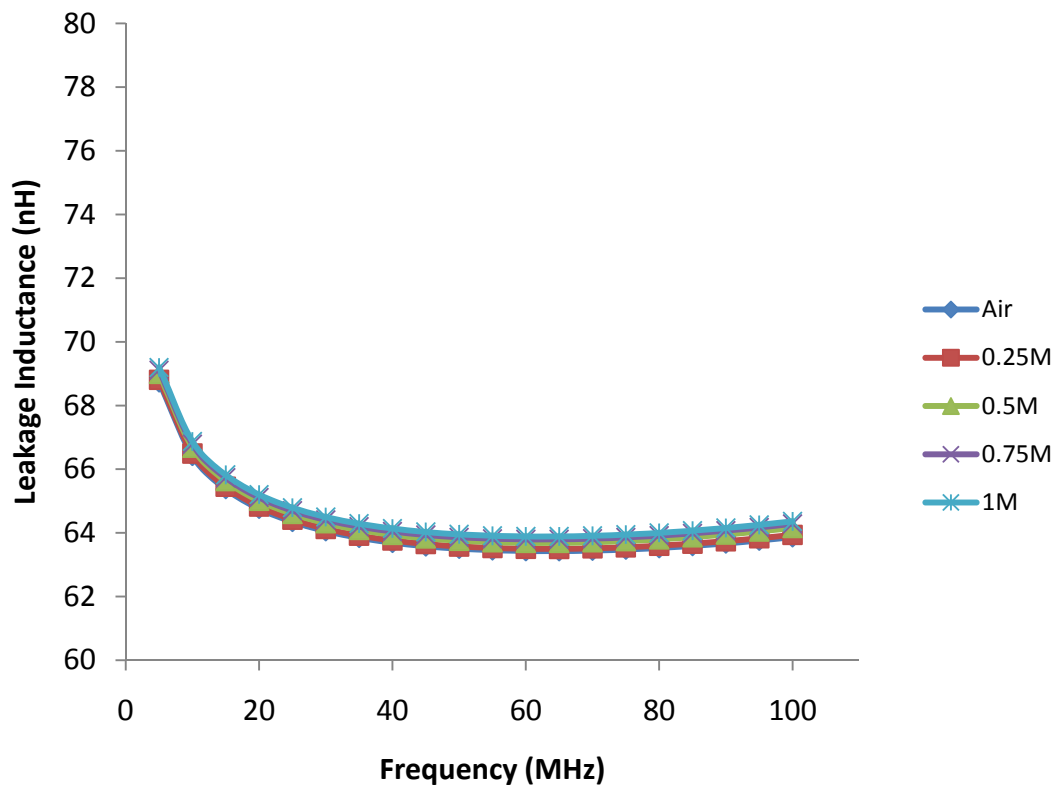
cores

Fig. 4.16 The simulated leakage inductance of coils of transformers with different
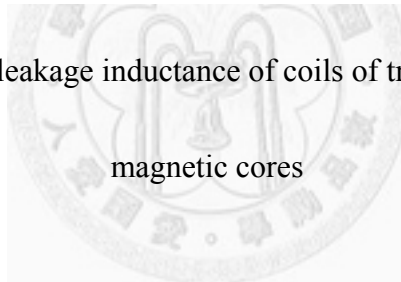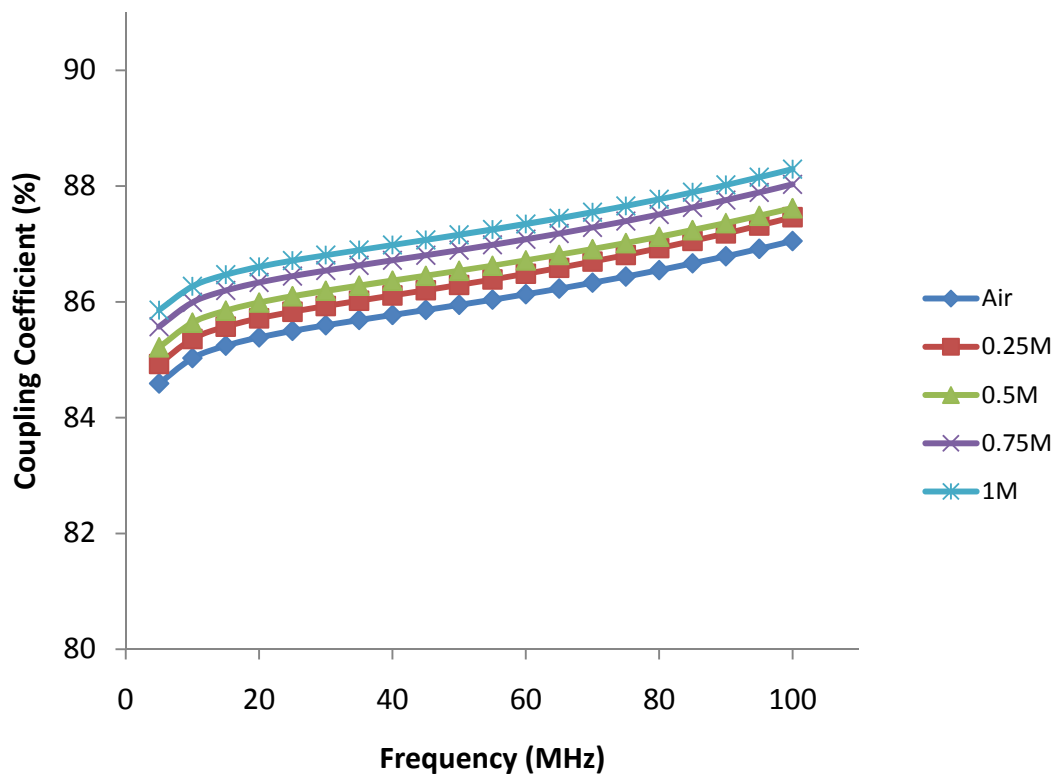
magnetic cores

Fig. 4.17 The simulated coupling coefficient of transformers with different magnetic
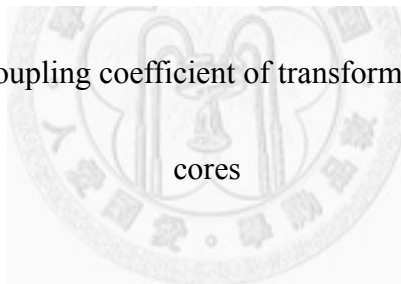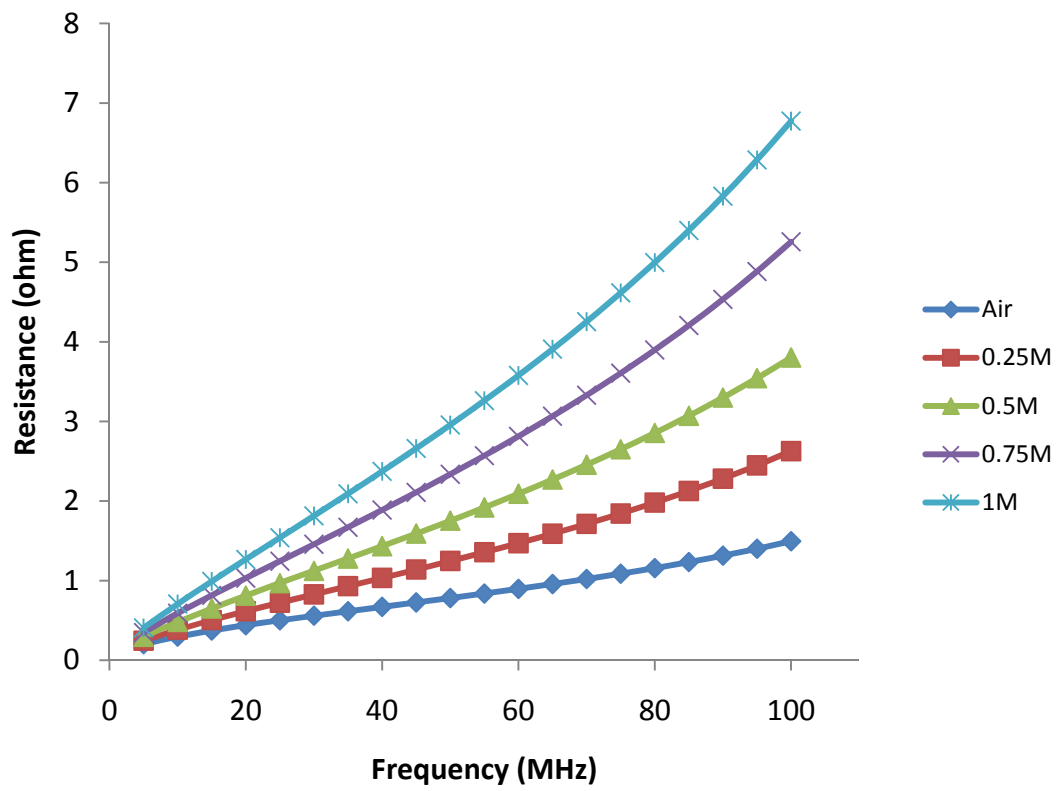
cores

Fig. 4.18 The simulated resistance of coils of transformers with different magnetic cores
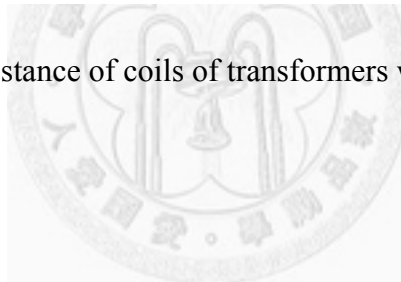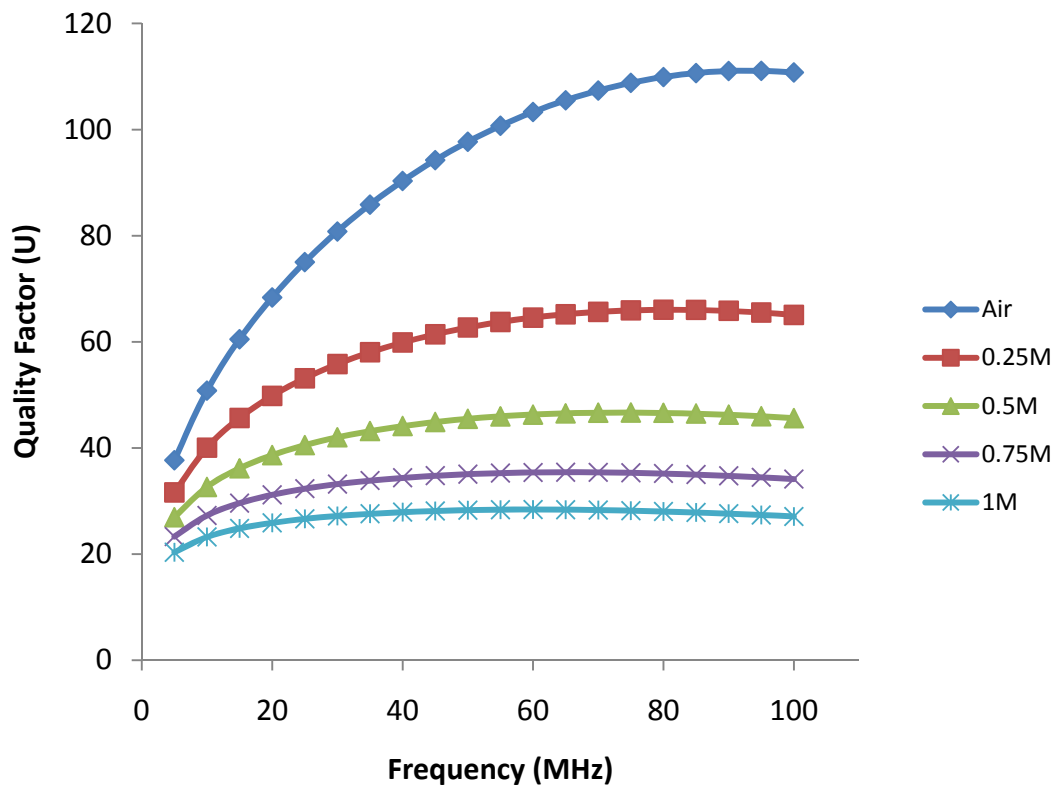
Fig. 4.18

Fig. 4.19 The simulated quality factor of coils of transformers with different magnetic

cores
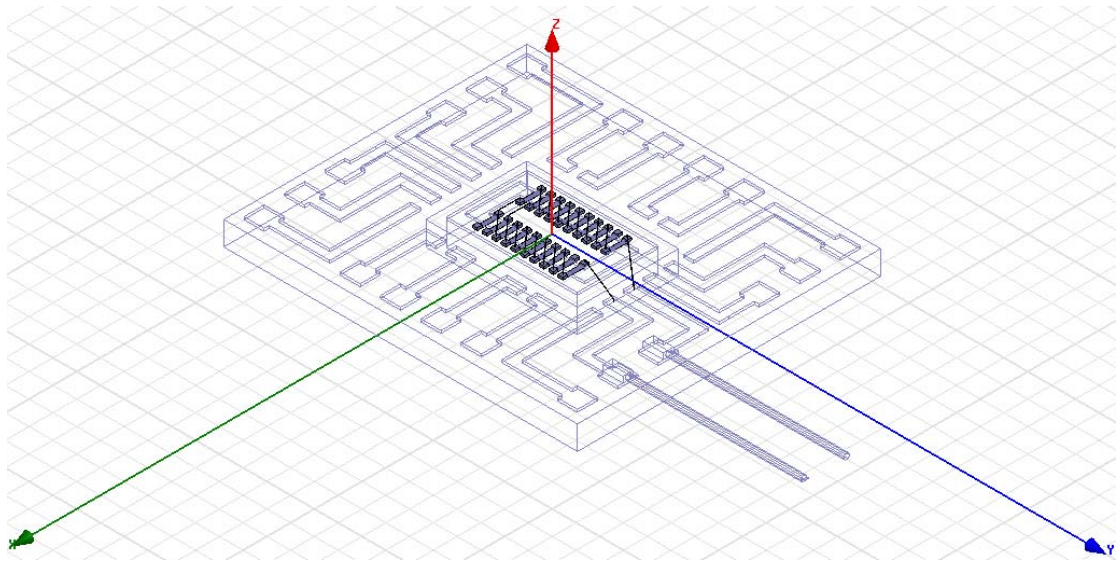
Fig. 4.20 The HFSS model of MEMS transformer with the PCB
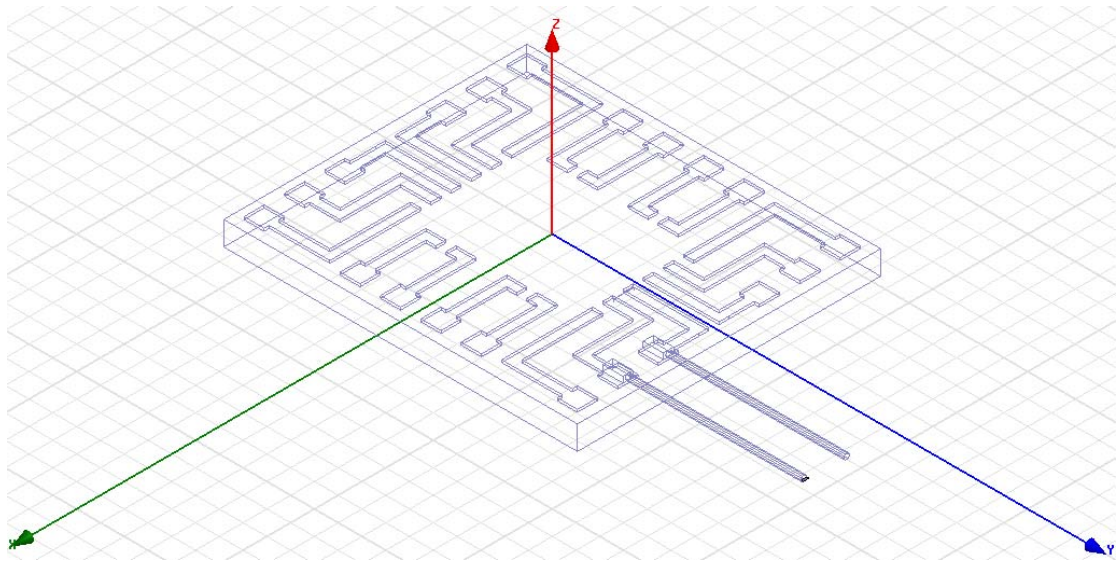
Fig. 4.21 The HFSS model of dummy PCB
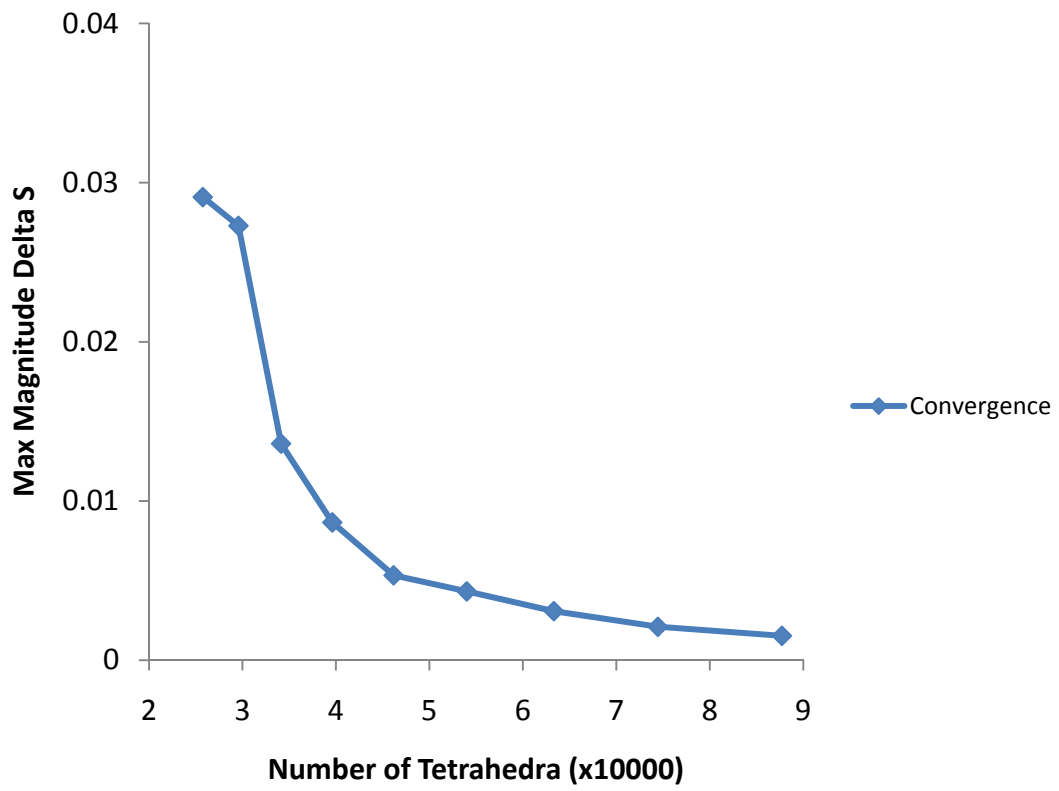
Fig. 4.22 The convergence curve of simulation with the model of MEMS transformer
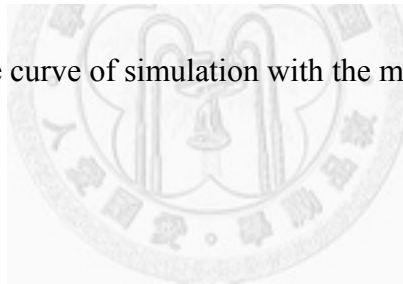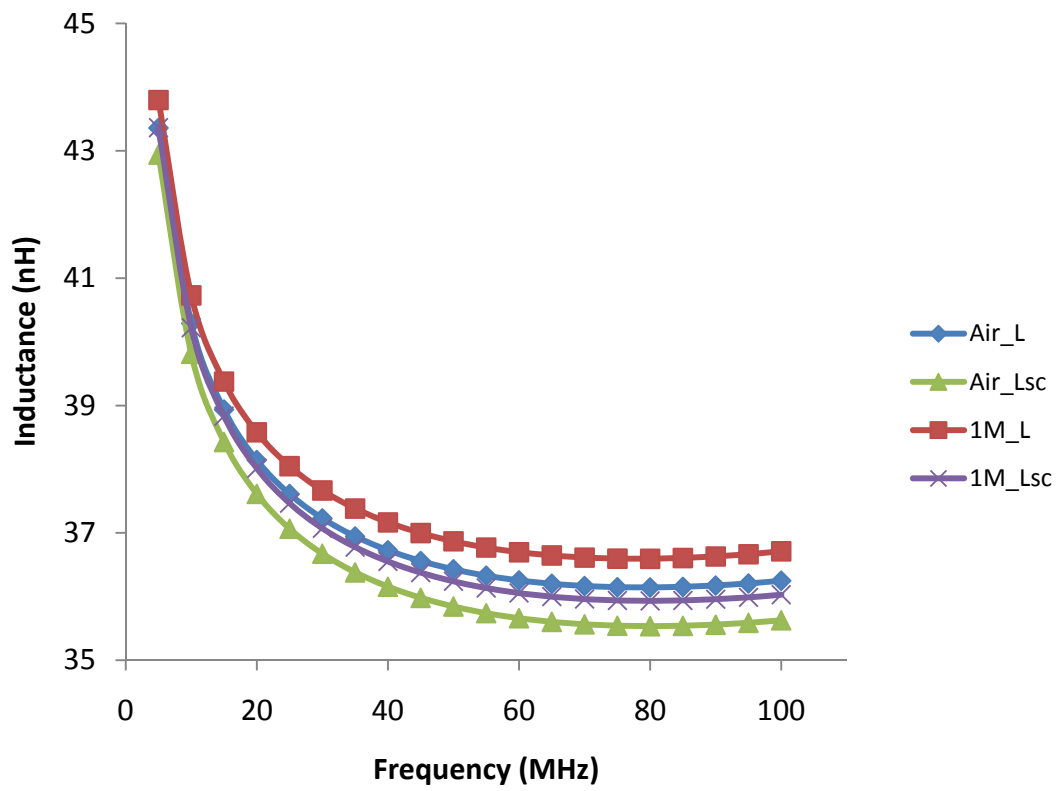
Fig. 4.23 The simulated self-inductance and leakage inductance of coils of MEMS

transformer with the air core and magnetic core of 1 M Fe_3O_4 nanofluid
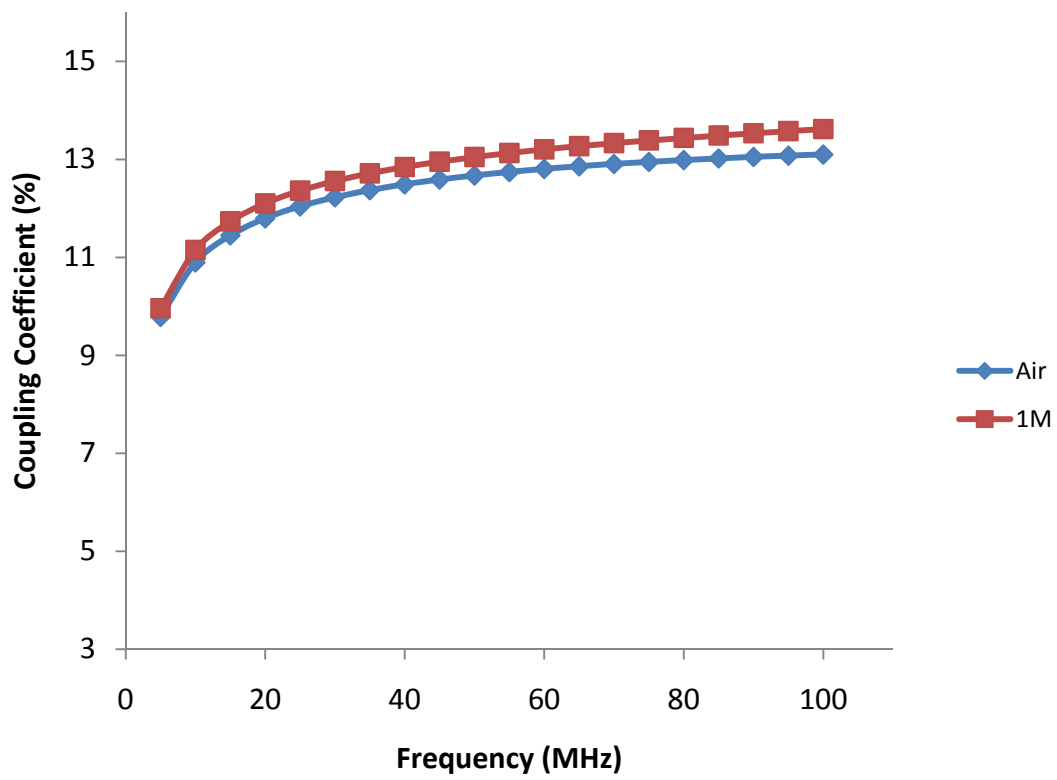
Fig. 4.24 The simulated coupling coefficient of MEMS transformer with the air core and

magnetic core of 1 M Fe_3O_4 nanofluid
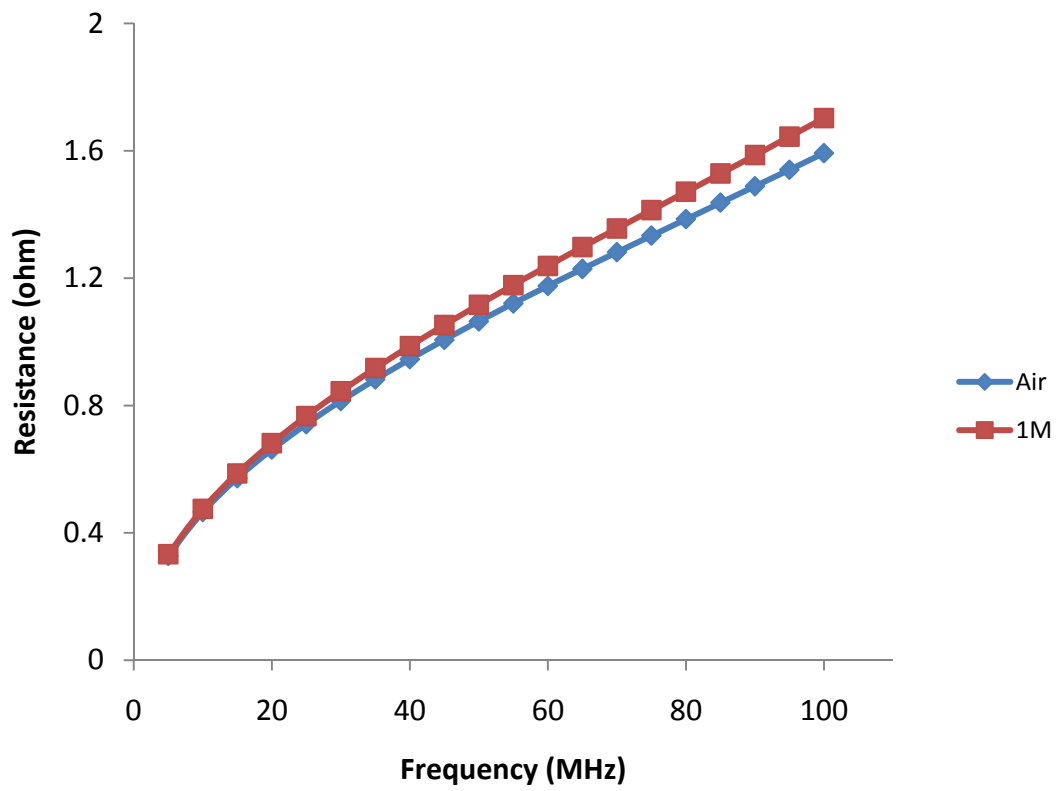
Fig. 4.25 The simulated resistance of coils of MEMS transformer with the air core and

magnetic core of 1 M Fe_3O_4 nanofluid
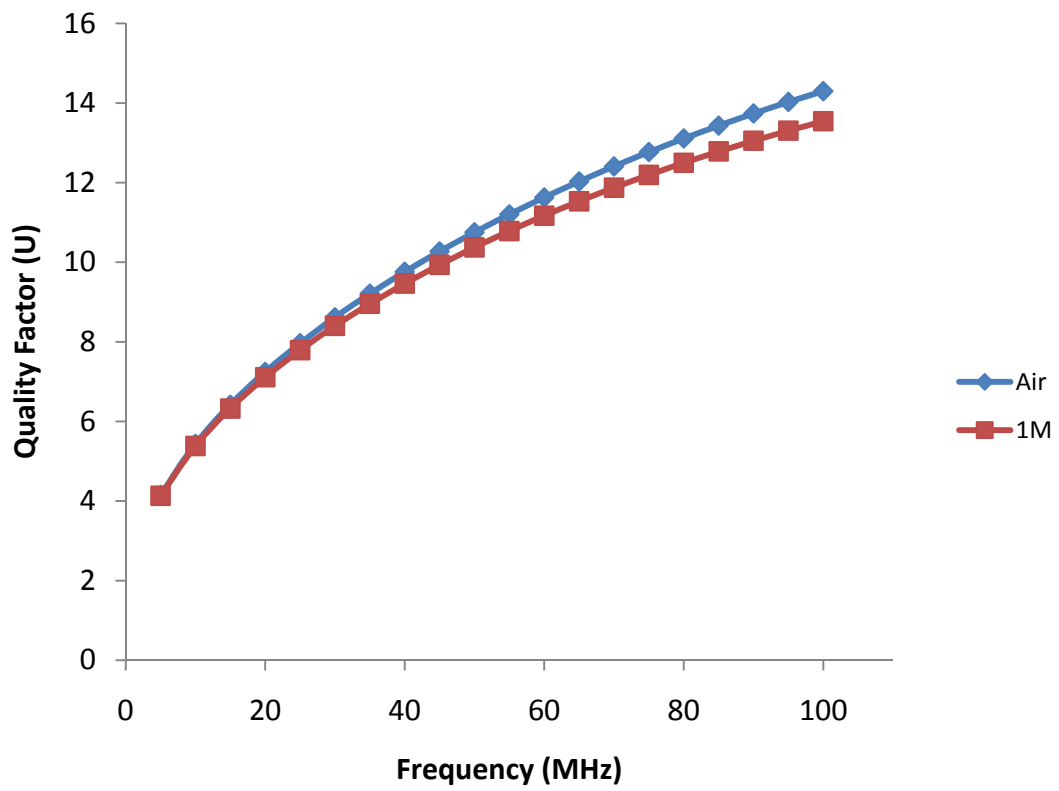
Fig. 4.26 The simulated quality factor of coils of MEMS transformer with the air core

and magnetic core of 1 M Fe_3O_4 nanofluid

Ferro-nanoparticle (Magnetic dipole)

(a)

Magnetic field

(b)
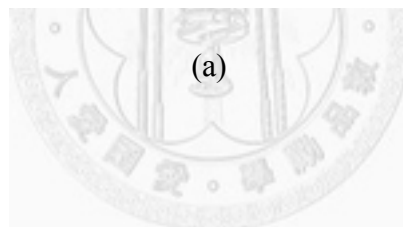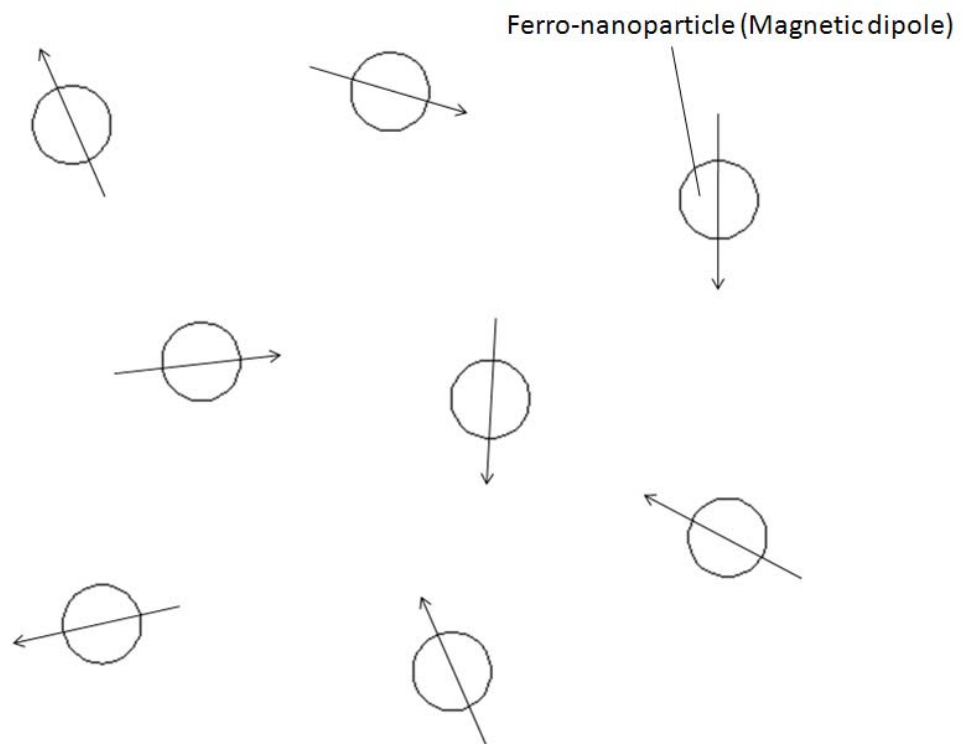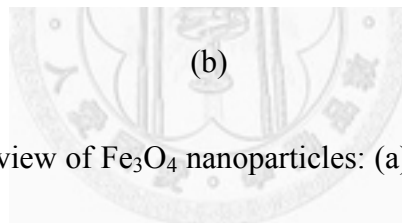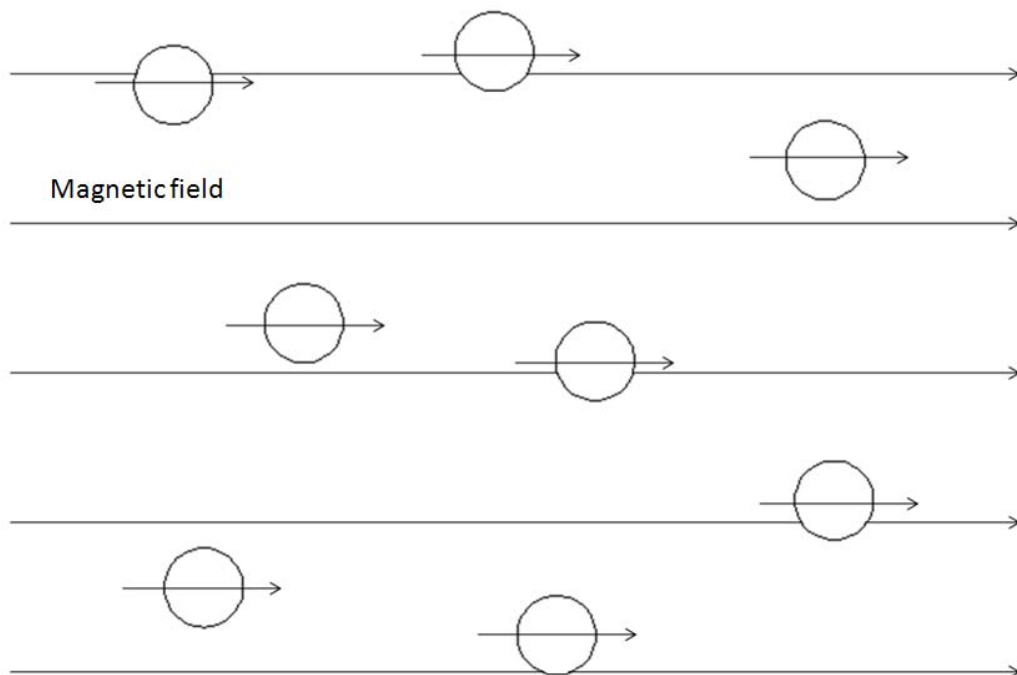
Fig. 4.27 The macroscopic view of Fe$_3$O$_4$ nanoparticles: (a) without a magnetic field; (b)

with a magnetic field.

Magnetic dipole

Ferro-nanoparticle

(a)

Magnetic field

(b)
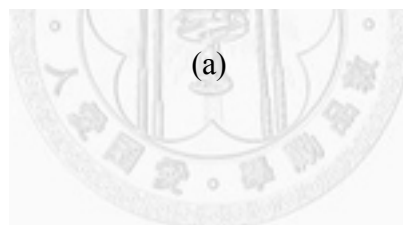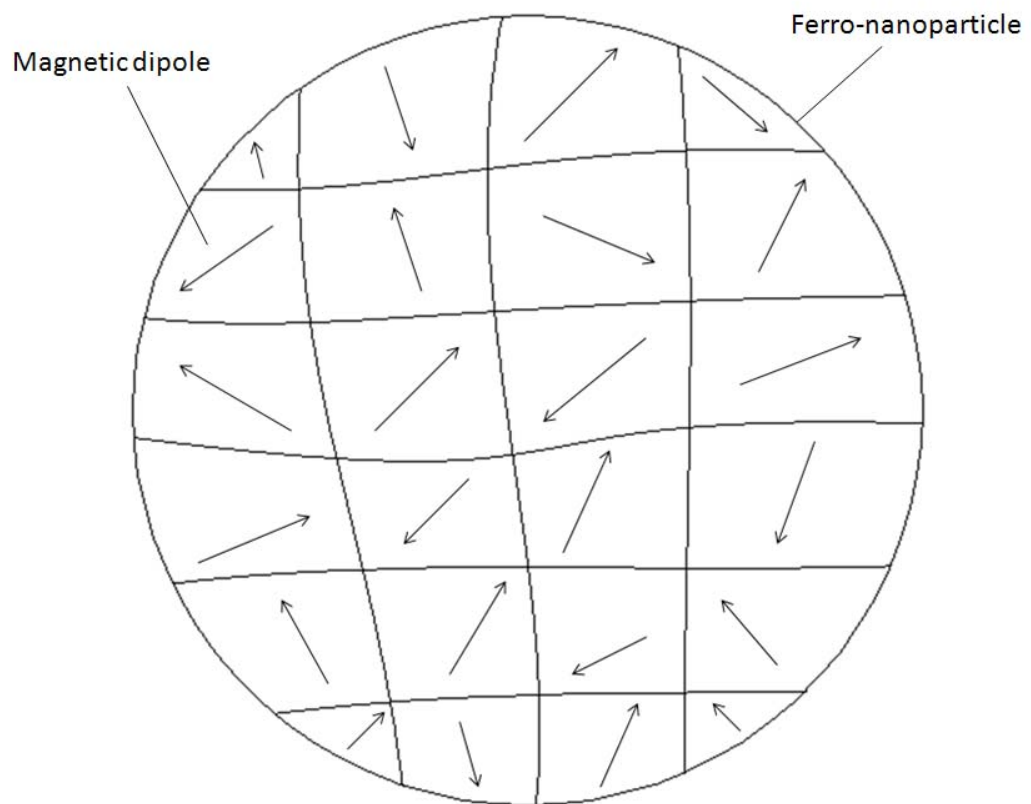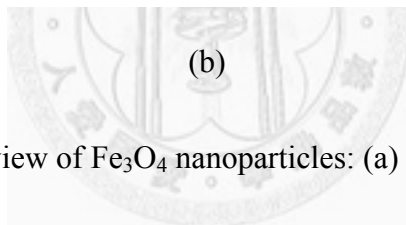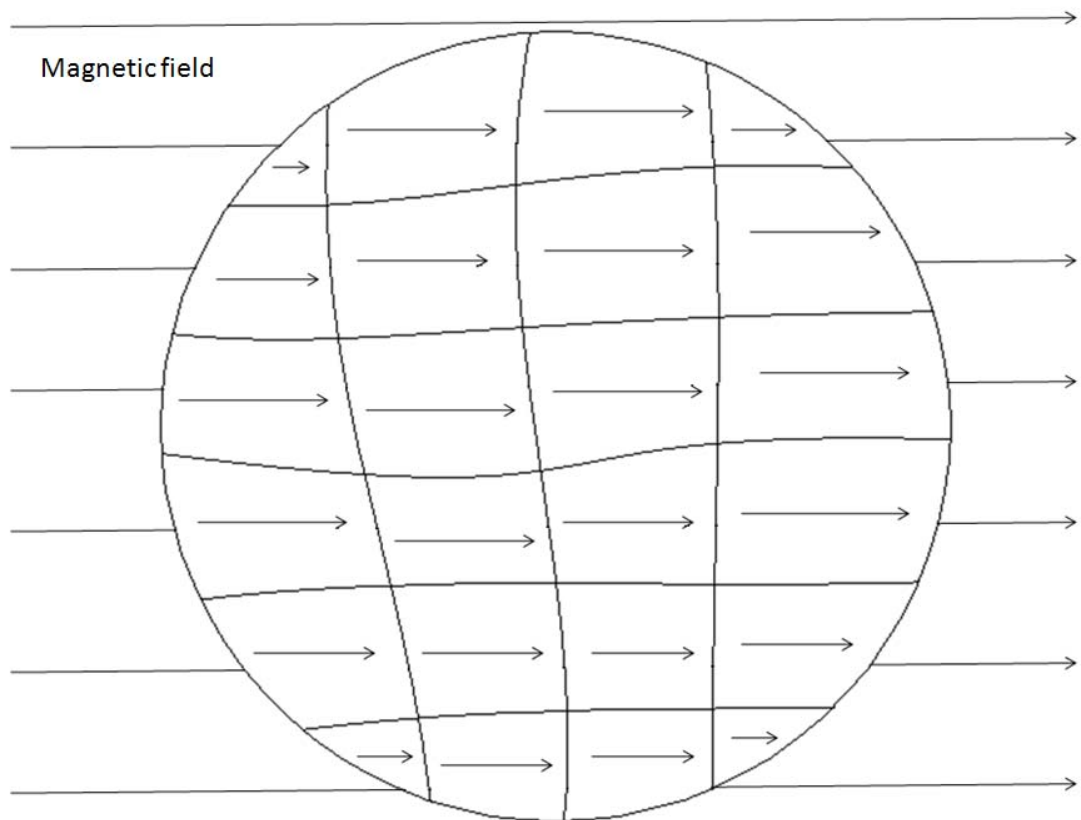
Fig. 4.28 The microscopic view of Fe$_3$O$_4$ nanoparticles: (a) without a magnetic field; (b)

with a magnetic field.

Chapter 5 Conclusions and Prospects

This thesis discusses two topics. The first is the effect of the viscosity of a base fluid on the thermal conductivity of nanofluids. The other one is the application of Fe_3O_4 nanofluids on transformers.

The thermal conductivities of nanofluids with various viscous base fluids were measured. The viscosity of the base fluids, the parameter of interest, was varied by changing the mixing ratio of two base fluids. The experimental results support the following conclusions.

1. The measured thermal conductivity of nanofluids with a low viscous base fluid exceeds that predicted by Maxwell prediction model.

2. As the viscosity of the base fluids increases, the measured thermal conductivity of the nanofluids gradually approaches the value predicted by the Maxwell prediction model. This result indicates that the high viscosity of base fluid constrains the Brownian motion of suspended nanoparticles and reduces their enhancement of thermal conductivity.

3. However, in a highly viscous fluid, the Maxwell prediction model accurately predicts the thermal conductivity of nanofluids, as the Brownian motion of suspended nanoparticles is unimportant, and $k_{static}=k_{Maxwell}$.

4. In summary, experimental results obtained using base fluids of various viscosities

indicate that the Brownian motion of suspended nanoparticles is important to their enhancement of the thermal conductivity of nanofluids, and that a model to predict the thermal conductivity of nanofluids should be based on the Maxwell prediction model.

Although numerous predictive models have been proposed, none offers accurate predictions on thermal conductivity for all nanofluids. Apart from the size and geometry of nanoparticles, the thermal properties of materials, the temperature of the nanofluids and other factors, many unknown factors, such as surface thermal resistance between nanoparticles and the base fluid affect the thermal conductivity of nanofluids. A theoretical understanding of the mechanisms is still lacking. Moreover, experimental results from different research groups regarding the production of nanofluids and the measurement of thermal conductivity do not agree closely. Advances in the heat transfer by nanofluids must address this fact. Therefore, further theoretical and experimental investigations must be performed to understand the heat transfer characteristics of a nanofluid. More measurements of the thermal conductivities of nanofluids with base fluids of various viscosities must be made to establish a predictive model that includes the effect of Brownian motion on oil-based ferrofluids. The effect of the viscosity of base fluids on the thermal conductivity of nanofluids should be confirmed with reference to various nanofluids.

Ferrofluids were used as the magnetic cores of two transformers. The performance of transformers with magnetic cores of air, bulk Fe_3O_4 and ferrofluids is measured. The experimental results support the following conclusions.

1. The presence of Fe_3O_4 improves the inductance of the coils and the coupling coefficient.

2. However, the lag between the magnetization of materials and the external magnetic field increases resistance. Moreover, as the frequency increases, the resistance increases to a great extent, and faster than inductance, yielding a low quality factor.

3. Although ferrofluid is not suitable for use as the magnetic core, it can be applied as a carrier of ferro-nanoparticles into the microchannel. Then, a solid magnetic core can be obtained by repeatedly adding ferrofluid and removing the base fluid. The experimental results of the application of bulk Fe_3O_4 reveal that it slightly improves the performance of a transformer at a frequency of less than 4 MHz.

4. This fabrication process of solid magnetic core has a lower thermal budget than the sputtering and electroplating processes, and it is compatible with the MEMS process.

This thesis proposed a new process for fabricating solid magnetic cores. However, the permeability of the solid magnetic core that was fabricated in this study was not as high as that of a sintered ferrite core. Therefore, further investigations of the method of

synthesis of magnetic nanoparticles, a substituent magnetic material and the fabrication

of bulk Fe_3O_4 are needed to improve the performance of transformers and realize this

new method for fabricating magnetic cores in the future.

References

[1] S. U. S. Choi, 1995, "Enhancing thermal conductivity of fluids with nanoparticles," *Developments and Applications of Non-Newtonian Flows*, FED 231/MD 66, 99-105

[2] J. A. Eastman, S. U. S. Choi, L. J. Thompson and S. Lee, 1997, "Enhanced thermal conductivity through the development of nanofluids," *Materials Research Society Symposium – Proceedings*, 457, 3-11

[3] S. Lee, S. U. S. Choi, S. Li and J. A. Eastman, 1999, "Measuring thermal conductivity of fluids containing oxide nanoparticles," *Journal of Heat Transfer*, 121, 280-289

[4] X. Wang, X. Xu and S. U. S. Choi, 1999, "Thermal conductivity of nanoparticle–fluid mixture," *Journal of Thermophysics and Heat Transfer*, 13, 4, 474-480

[5] Y. Xuan and Q. Li, 2000, "Heat transfer enhancement of nanofluids," *International Journal of Heat and Fluid Transfer*, 21, 58-64

[6] H. Xie, J. Wang, T. Xi, Y. Liu, F. Ai and Q. Wu, 2002, "Thermal conductivity enhancement of suspensions containing nanosized alumina particles," *Journal of Applied Physics*, 91, 7, 4568-4572

[7] J. A. Eastman, S. U. S. Choi, S. Li, W. Yu and L. J. Thompson, 2001, "Anomalously increased effective thermal conductivities of ethylene glycol-based nanofluids containing copper nanoparticles," *Applied Physics Letters*, 78, 6, 718-720

[8] B. M. Berkovsky and V. G. Bashtovoy, 1996, *Magnetic Fluids and Applications Handbook*, Begell House, New York

[9] B. M. Berkovsky, V. F. Medvedev and M. S. Krakov, 1993, *Magnetic Fluids: Engineering Application*s, Oxford University Press, New York

[10] M. Zahn, 2001, "Magnetic fluid and nanoparticle applications to nanotechnology," *Journal of Nanoparticle Research*, 3, 73-78

[11] J. C. Maxwell, 1873, *A Treatise on Electricity and Magnetism*, Clarendon Press, Oxford, UK

[12] P. Keblinski, J. A. Eastman and D. G. Cahill, 2005, "Nanofluids for thermal transport," *Materials Today*, 8, 6, 36-44

[13] T. K. Hong, H. S. Yang and C. J. Choi, 2005, "Study of the enhanced thermal conductivity of Fe nanofluids," *Journal of Applied Physics*, 97, 6, 1-4

[14] K. Hong, T. K. Hong and H. S. Yang, 2006, "Thermal conductivity of Fe nanofluids depending on the cluster size of nanoparticles," *Applied Physics Letters*, 88, 3, 31901

[15] S. M. S. Murshed, K. C. Leong and C. Yang, 2005, "Enhanced thermal

conductivity of TiO$_2$-water based nanofluids," *International Journal of Thermal Sciences*, 44, 4, 367-373

[16] H. Xie, J. Wang, T. Xi and Y. Liu, 2001, "Study on the thermal conductivity of SiC nanofluids," *Journal of the Chinese Ceramic Society*, 29, 4, 361-364

[17] H. Xie, J. Wang, T. Xi and Y. Liu, 2002, "Thermal conductivity of suspensions containing nanosized SiC particles," *International Journal of Thermophysics*, 23, 2, 571-580

[18] R. L. Hamilton and O. K. Crosser, 1962, "Thermal conductivity of heterogeneous two-component systems," *I&EC Fundam*, 1, 182-191

[19] S. K. Das, N. Putta, P. Thiesen and W. Roetzel, 2003, "Temperature dependence of thermal conductivity enhancement for nanofluids," *Journal of Heat Transfer*, 125, 567-574

[20] C. H. Li and G. P. Peterson, 2006, "Experimental investigation of temperature and volume fraction variations on the effective thermal conductivity of nanoparticle suspensions (nanofluids)," *Journal of Applied Physics*, 99, 8, 084314

[21] H. E. Patel, S. K. Das, T. Sundararagan, A. S. Nair, B. Geoge and T. Pradeep, 2003, "Thermal conductivities of naked and monolayer protected metal nanoparticle based nanofluids: Manifestation of anomalous enhancement and chemical effects," *Applied Physics Letters*, 83, 2931-2933

[22] P. Keblinski, S. R. Phillpot, S. U. S. Choi and J. A. Eastman, 2002, "Mechanisms of heat flow in suspensions of nano-sized particles (nanofluids)," *International Journal of Heat and Mass Transfer*, 45, 855-863

[23] J. A. Eastman, S. R. Phillpot, S. U. S. Choi and P. Keblinski, 2004, "Thermal transport in nanofluids," *Annual Review of Materials Research*, 34, 219-246

[24] W. Yu and S. U. S. Choi, 2003, "The role of interfacial layers in the enhanced thermal of nanofluids: a renovated Maxwell model," *Journal of Nanoparticle Research*, 5, 167-171

[25] W. Yu and S. U. S. Choi, 2004, "The role of interfacial layers in the enhanced thermal conductivity of nanofluids: a renovated Hamilton–Crosser model," *Journal of Nanoparticle Research*, 6, 4, 355-361

[26] L. Xue, P. Keblinski, S. R. Phillpot, S. U. S. Choi and J. A. Eastman, 2004, "Effect of liquid layering at the liquid–solid interface on thermal transport," *International Journal of Heat and Mass Transfer*, 47, 4277-4284

[27] J. Koo and C. Kleinstreuer, 2005, "Impact analysis of nanoparticle motion mechanisms on the thermal conductivity of nanofluids," *International Communications in Heat and Mass Transfer*, 32, 9, 1111-1118

[28] W. Evans, J. Fish and P. Keblinski, 2006, "Role of Brownian motion hydrodynamics on nanofluid thermal conductivity," *Applied Physics Letters*, 88, 9,

93116

[29] D. Lee, J. W. Kim and B. G. Kim, 2006, "A new parameter to control heat transport in nanofluids: Surface charge state of the particle in suspension," *Journal of Physical Chemistry B*, 110, 9, 4323-4328

[30] Q. Z. Xue, 2003, "Model for effective thermal conductivity of nanofluids," *Physics Letters A*, 307, 313-317

[31] Q. Xue and W. M. Xu, 2005, "A model of thermal conductivity of nanofluids with interfacial shells," *Materials Chemistry and Physics*, 90, 298-301

[32] H. Xie, M. Fujii and X. Zhang, 2005, "Effect of interfacial nanolayer on the effective thermal conductivity of nanoparticle–fluid mixture," *International Journal of Heat and Mass Transfer*, 48, 14, 2926-2932

[33] Y. Xuan, Q. Li and W. Hu, 2003, "Aggregation structure and thermal conductivity of nanofluids," *AIChE Journal*, 49, 4, 1038-1043

[34] D. H. Kumar, H. E. Patel, V. R. R. Kumar, T. Sundararajan, T. Pradeep and S. K. Das, 2004, "Model for heat conduction in nanofluids," *Physical Review Letters*, 93, 14, 144301

[35] P. Bhattacharya, S. K. Saha, A. Yadav, P. E. Phelan and R. S. Prasher, 2004, "Brownian dynamics simulation to determine the effective thermal conductivity of nanofluids," *Journal of Applied Physics*, 95, 11, 6492-6494

[36] S. P. Jang and S. U. S. Choi, 2004, "Role of Brownian motion in the enhanced thermal conductivity of nanofluids," *Applied Physics Letters*, 84, 4316-4318

[37] S. P. Jang and S. U. S. Choi, 2007, "Effects of various parameters on nanofluid thermal conductivity," *Journal of Heat Transfer*, 129, 617-623

[38] P. L. Kapitza, 1941, "The study of heat transfer in Helium II," *Journal of Physics Moscow*, 4, 181-210

[39] R. Prasher, P. Bhattacharya and P. E. Phelan, 2006, "Thermal conductivity of nanoscale colloidal solutions (nanofluids)," *Physical Review Letters*, 94, 2, 025901

[40] J. Koo and C. Kleinstreuer, 2004, "A new thermal conductivity model for nanofluids," *Journal of Nanoparticle Research*, 6, 6, 577-588

[41] J. Koo, C. Kleinstreuer, 2005, "Laminar nanofluid flow in micro-heat sinks," *International Journal of Heat and Mass Transfer*, 48, 13, 2652-2661

[42] R. E. Rosenweig, 1985, *Ferrohydrodynamics*, Cambridge University Press, New York

[43] W. C. Elmore, 1938, "Ferromagnetic colloid for studying magnetic structure," *Physical review*, 54, 4, 309-310

[44] S. E. Khalafalla and G. W. Reimers, 1980, "Preparation of dilution-stable aqueous magnetic fluids," *IEEE Transactions on Magnetics*, 16, 2, 178-183

[45] S. S. Papell, 1965, "Manufacture of Magnetofluids," *U. S. Patent*, 3215527

[46] K. Raj and R. Moskowitz, 1990, "Commercial applications of ferrofluids," *Journal of Magnetism and Magnetic Materials*, 85, 233-245

[47] M. Sinkai, 2002, "Functional magnetic particles for medical application," *Journal of Bioscience and Bioengineering*, 94, 6, 606-613

[48] Q. A. Pankhurst, J. Connolly, S. K. Jones and J. Dobson, 2003, "Applications of magnetic nanoparticles in biomedicine," *Journal of Physics D: Applied Physics*, 36, R167-R181

[49] I. Hilger, A. Kießling, E. Romanus, R. Hiergeist, R. Hergt, W. Andra, M. Roskos, W. Linss, P. Weber, W. Weitschies and W. A. Kaiser, 2004, "Magnetic nanoparticles for selective heating of magnetically labelled cells in culture: preliminary investigation," *Nanotechnology*, 15, 1027–1032

[50] R. Hiergeist, W. Andra, N. Buske, R. Hergt, I. Hilger, U. Richter and W. Kaiser, 1999, "Application of magnetite ferrofluids for hyperthermia," *Journal of Magnetism and Magnetic Materials*, 201, 420-422

[51] R. E. Rosenweig, 2002, "Heating magnetic fluid with alternating magnetic field," *Journal of Magnetism and Magnetic Materials*, 252, 370-374

[52] Z. G. Forbes, B. B. Yellen, K. A. Barbee and G. Friedman, 2003, "An approach to targeted drug delivery based on uniform magnetic fields," *IEEE Transactions on Magnetics*, 39, 5, 3372-3377

[53] G. S. Park and S. H. Park, 1999, "Design of magnetic fluid linear pump," *IEEE Transactions on Magnetics*, 35, 4058-4060

[54] A. Hatch, A. E. Kaholz, G. Holman, P. Yager and K. F. Böhringer, 2001, "A ferrofluidic magnetic micropump," *Journal of Microelectromechanical Systems*, 10, 2, 215-221

[55] C. Yamahata, M. Chastellain, V. K. Parashar, A. Petri, H. Hofmann and M. A. M. Gijs, 2005, "Plastic micropump with ferrofluidic actuation," *Journal of Microelectromechanical Systems*, 14, 96-102

[56] H. Hartshorne, C. J. Backhouse and W. E. Lee, 2004, "Ferrofluid-based microchip pump and valve," *Sensors and Actuators B: Chemical*, 99, 592-600

[57] C. W. Chang, T. H. Tsai, T. C. Chiang, P. Y. Wang, Y. F. Hsieh, C. H. Chang and P. H. Chen, 2007, "Fast mixing of nanofluids in microchannel," *Proceedings of the International Conference on Integration and Commercialization of Micro and Nanosystems 2007*, 61-64

[58] T. H. Tsai, P. H. Chen, D. S. Liou and C. T. Yang, 2009, "Enhancement of mixing performance of water solutions in a micro-mixer with immiscible ferrofluid," *2009 4th IEEE International Conference on Nano/Micro Engineered and Molecular Systems*, 69-74

[59] T. H. Tsai, D. S. Liou, L. S. Kuo and P. H. Chen, 2009, "Rapid mixing between

ferro-nanofluid and water in a semi-active Y-type micromixer," *Sensors and Actuators A: Physical*, 153, 267-273

[60] H.J. Ryu, S. H. Han and H. J. Kim, 1999, "Characteristics of twin spiral type thin film inductor with Fe-based nanocrystalline core," *IEEE Transaction on Magnetics*, 35, 5, 3568-3570

[61] C. S. Kim, S. Bae, H. J. Kim, S. E. Nam and H. J. Kim, 2001, "Fabrication of high frequency DC-DC converter using Ti/FeTaN film inductor," *IEEE Transactions on Magnetics*, 37, 4, 2894-2896

[62] K. H. Kim, J. Kim, H. J. Kim, S. H. Han and H. J. Kim, 2002, "A megahertz switching DC/DC converter using FeBN thin film inductor," *IEEE Transaction on Magnetics*, 38, 5, 3162-3164

[63] N. Wang, T. O'Donnell, S. Roy, M. Brunet, P. McCloskey and S. C. O'Mathuna, 2005, "High-frequency micro-machined power inductors," *Journal of Magnetism and Magnetic Materials*, 290-291, 1347-1350

[64] J. B. Yoon, B. I. Kim, Y. S. Choi and E. Yoon, 2002, "3-D lithography and metal surface micromachining for RF and microwave MEMS," *IEEE International MEMS Conference*, 673-676

[65] Y. S. Choi, J. B. Yoon, B. I. Kim and E. Yoon, 2002, "A high-performance MEMS transformer for silicon RF ICs," *IEEE International MEMS Conference*, 653-656

[66] E. C. Park, Y. S. Choi, J. B. Yoon and E. Yoon, 2002, "Monolithically integrable RF MEMS passives," *Journal of Semiconductor Technology and Science*, 2, 1, 49-55

[67] J. B. Yoon, B. I. Kim, Y. S. Choi and E. Yoon, 2003, "3-D construction of monolithic passive components for RF and microwave ICs using thick-metal surface micromachining technology," *IEEE Transactions on Microwave Theory and Techniques*, 51, 1, 279-288

[68] K. Chong and Y. H. Xie, 2005, "High-performance on-chip transformers," *IEEE Electron Device Letters*, 26, 8, 557-559

[69] J. H. Zhao, J. Zhu, Z. M. Chen and Z. W. Liu, 2005, "Radio-frequency planar integrated inductor with permalloy-SiO_2 granular films," *IEEE Transactions on Magnetics*, 41, 8, 2334-2338

[70] J. Yunas, A. A. Hamzah, B. Y. Majlis, 2009, "Fabrication and characterization of surface micromachined stacked transformer on glass substrate," *Microelectronic Engineering*, 86, 2020-2025

[71] J. Yunas, A. A. Hamzah and B. Y. Majlis, 2009, "Surface micromachined on-chip transformer fabricated on glass substrate," *Microsystem Technologies*, 15, 547-552

[72] D. C. Laney, L. E. Larson, P. Chan, J. Malinowski, D. Harame, S. Subbanna, R. Volant and M. Case, 1999, "Lateral microwave transformers and inductors

implemented in a Si/SiGe HBT process," *IEEE International Microwave Symposium Digest*, 3, 855-858

[73] J. B. Yoon, C. H. Han, E. Yoon and C. K. Kim, 1998, "Monolithic fabrication of electroplated solenoid inductors using three-dimensional photolithography of a thick photoresist," *Japanese Journal of Applied Physics*, 37, 7081-7085

[74] J. B. Yoon, C. H. Han, E. Yoon and C. K. Kim, 1999, "Monolithic integration of 3-D electroplated microstructures with unlimited number of levels using planarization with a sacrificial metallic mold (PSMM)," *IEEE MEMS Technical Digest*, 624-629

[75] Y. S. Choi, J. B. Yoon, B. I. Kim, E. Yoon and C. H. Han, 2001, "Fabrication of a solenoid-type microwave transformer," *Transducer'01*, 1564-1567

[76] M. Xu, T. M. Liakopoulos and C. H. Ahn, 1998, "A microfabricated transformer for high-frequency power or signal conversion," *IEEE Transactions on Magnetics*, 34, 1369-1371

[77] Y. Zhuang, B. Rejaei, E. Boellaard, M. Vroubel and J. N. Burghartz, 2003, "Integrated solenoid inductors with patterned, sputter-deposited Cr/Fe10Co90/Cr ferromagnetic cores," *IEEE Electron Device Letters*, 24, 4, 224-226

[78] J. W. Park and M. G. Allen, 2003, "Ultralow-profile micromachined power inductors with highly laminated Ni/Fe cores: Application to low-megahertz

DC-DC converters," *IEEE Transactions on Magnetics*, 39, 5, 3184-3186

[79] X. Y. Gao, Y. Cao, Y. Zhou, W. Ding, C. Lei and J. A. Chen, 2006, "Fabrication of solenoid-type inductor with electroplated NiFe magnetic core," *Journal of Magnetism and Magnetic Materials*, 305, 207-211

[80] C. Lei, Y. Zhou, X. Y. Gao, W. Ding, Y. Cao, H. Choi and J. H. Won, 2007, "Fabrication of a solenoid-type inductor with Fe-based soft magnetic core," *Journal of Magnetism and Magnetic Materials*, 308, 284-288

[81] W. A. Wakeman, A. Nagashime and J. V. Sengers, 1991, *Measurement of the Transport Properties of Fluids*, Blackwell, Oxford

[82] Decagon Devices, Inc., 2004, *KD2 thermal properties analyzer user's manual*, version 1.3

[83] Yong-Zhen technomaterial CO. LTD, http://qfnano.diytrade.com/sdp/404613/3/ pl-2170606/0.html

[84] L. Xue, P. Keblinski, S. R. Phillpot, S. U. S. Choi and J. A. Eastman, 2003, "Two regimes of thermal resistance at a liquid-solid interface," *Journal of Chemical Physics*, 118, 337

[85] E. V. Timofeeva, A. N. Gavrilov, J. M. McCloskey, Y. V. Tolmachev, S. Sprunt, L. M. Lopatina and J. V. Selinger, 2007, "Thermal conductivity and particle agglomeration in alumina nanofluids: Experiment and theory," *Physical Review E*,

76, 061203

[86] Ansoft Electronic Design Products, *Ansoft online help*, version 10.0

[87] I. Hrianca and I. Malaescu, 1995, "The rf magnetic permeability of statically magnetized ferrofluids," *Journal of Magnetism and Magnetic Materials*, 150, 131-136

[88] G. M. Sutariya, D. Vincent, B. Bayard, R. V. Upadhyay, G. Noyel and R. V. Mehta, 2003, "Magnetic DC field and temperature dependence on complex microwave magnetic permeability of ferrofluids: effect of constituent elements of substituted Mn ferrite," *Journal of Magnetism and Magnetic Materials*, 260, 42-47